

Gravitational wave sources in our Galactic backyard: Predictions for BHBH, BHNS and NSNS binaries detectable with LISA

2 T. WAGG ,^{1,2,3} F.S. BROEKGAARDEN ,² S.E. DE MINK ,^{3,4,2} N. FRANKEL ,^{5,6,7} L.A.C. VAN SON ,^{2,4,3} AND
3 S. JUSTHAM 

4 ¹*Department of Astronomy, University of Washington, Seattle, WA, 98195*

5 ²*Center for Astrophysics — Harvard & Smithsonian, 60 Garden Street, Cambridge, MA 02138, USA*

6 ³*Max-Planck-Institut für Astrophysik, Karl-Schwarzschild-Straße 1, 85741 Garching, Germany*

7 ⁴*Anton Pannekoek Institute for Astronomy & Grappa, University of Amsterdam, Postbus 94249, 1090 GE Amsterdam, The Netherlands*

8 ⁵*Canadian Institute for Theoretical Astrophysics, University of Toronto, 60 St. George Street, Toronto, ON M5S 3H8, Canada*

9 ⁶*Max Planck Institute for Astronomy, Königstuhl 17, D-69117 Heidelberg, Germany*

10 ⁷*David A. Dunlap Department for Astronomy and Astrophysics, University of Toronto, 50 St. George Street, Toronto, ON M5S 3H4, Canada*

11 ⁸*School of Astronomy & Space Science, University of the Chinese Academy of Sciences, Beijing 100012, China*

13 (Received January 21, 2022)

ABSTRACT

15 Future searches for gravitational waves from space will be sensitive to double compact objects (DCOs)
16 in our Milky Way. We present new simulations of the populations of double black holes (BHBHs), black
17 hole neutron stars (BHNSs) and double neutron stars (NSNSs) that will be detectable by the planned
18 space-based gravitational wave detector LISA. For our estimates, we use an empirically-informed model
19 of the metallicity dependent star formation history of the Milky Way. We populate it using an extensive
20 suite of binary population-synthesis predictions for varying assumptions relating to mass transfer,
21 common-envelope, supernova kicks, remnant masses and wind mass loss physics.

22 For a 4(10)-year LISA mission, we predict between 30-370(50-550) detections over these variations,
23 out of which 6-154(9-238) are BHBHs, 2-198(3-289) are BHNSs and 3-35(4-57) are NSNSs. We discuss
24 how the variations in the physics assumptions alter the distribution of properties of the detectable
25 systems, even when the detection rates are unchanged. In particular we discuss the observable char-
26 acteristics such as the chirp mass, eccentricity and sky localisation and how the BHBH, BHNS and
27 NSNS populations can be distinguished, both from each other and from the more numerous double
28 white dwarf population. We further discuss the possibility of multi-messenger observations of pulsar
29 populations with the Square Kilometre Array (SKA) and assess the benefits of extending the LISA
30 mission.

31 **Keywords:** gravitational waves, gravitational wave detectors, compact objects, stellar mass black holes,
32 neutron stars, binary stars, stellar evolution, pulsars

1. INTRODUCTION

33 Since the first direct observation of gravitational waves
34 ([Abbott et al. 2016](#)), the number of black hole (BH) and
35 neutron star (NS) binaries observed by ground-based
36 gravitational-wave detectors has rapidly grown ([Abbott
37 et al. 2019, 2020b; The LIGO Scientific Collaboration
38 et al. 2021c](#)), offering exciting insights into the forma-

39 [et al. 2021c](#)), offering exciting insights into the forma-
40 tion, lives and deaths of massive (binary) stars (e.g. [Ab-](#)
41 [bott et al. 2021](#)).

42 The Laser Interferometer Space Antenna (LISA,
43 [Amaro-Seoane et al. 2017; Colpi et al. 2019](#)) will pro-
44 vide observations in an entirely new regime of grav-
45 itational waves. LISA will observe at lower frequen-
46 cies ($10^{-5} \lesssim f/\text{Hz} \lesssim 10^{-1}$) than ground-based detec-
47 tors and so will enable the study of sources that are
48 imperceptible by ground-based detectors, such as the
49 mergers of supermassive black holes and extreme mass-

ratio inspirals (e.g. Begelman et al. 1980; Klein et al. 2016). Moreover, this frequency regime is also of interest for the detection of *local* stellar-mass double compact objects (DCOs) millions of years before their merger. This presents an opportunity for both multi-messenger detections to search for electromagnetic counterparts, as well as multiband gravitational-wave detections that can help to constrain binary characteristics (e.g. Sesana 2016; Gerosa et al. 2019). In addition, LISA will be able to measure the eccentricities of DCOs, which may yield further constraints on binary evolution, differentiate between formation channels and distinguish between DCO types (e.g. Nelemans et al. 2001; Breivik et al. 2016; Antonini et al. 2017; Rodriguez et al. 2018). Unlike ground-based detectors, the majority of stellar-mass sources detected in LISA will reside in local galaxies, with most situated in the Milky Way. These sources could be used as a probe for the structure of our galaxy (e.g. Korol et al. 2019).

Traditionally, predictions about the detection of stellar-mass sources with LISA focus on double white dwarf (WDWD) binaries, as they are abundantly present in our galaxy and are expected to be the dominant source of stellar-mass binaries that are detectable by LISA (Nelemans et al. 2001; Ruiter et al. 2010; Yu & Jeffery 2010; Nissanke et al. 2012; Korol et al. 2017; Lamberts et al. 2018). More recently, interest has grown in the detection of NS and BH binaries. Although they are more rare, LISA detections of these sources are potentially valuable for learning more about the evolution and endpoints of massive stars. In this paper we focus on making LISA predictions for double black hole binaries (BHBHs), black hole neutron star binaries (BHNSs) and double neutron star binaries (NSNSs).

The detection of NSNSs in LISA could improve our understanding of many phenomena. Galactic NSNSs have been observed with electromagnetic signals for several decades (e.g. Hulse & Taylor 1975; Antoniadis et al. 2016, see also refs. in Tauris et al. 2017) and more recently the mergers of NSNSs have been detected with ground-based gravitational-wave detectors (e.g. Abbott et al. 2017a). A LISA detectable NSNS with a pulsar component close to merger would be ideal for connecting these populations, as the binary could be observed from inspiral to merger. NSNSs (and possibly BHNSs) are useful sources for understanding the origin of r-process elements (e.g. Eichler et al. 1989) as well as the electromagnetic counterparts to gravitational-wave signals, such as kilonovae (e.g. Li & Paczyński 1998; Metzger 2017), short gamma-ray bursts (e.g. Berger 2014), radio emission (e.g. Hotokezaka et al. 2016) and neutrinos (e.g. Kyutoku et al. 2018).

BHBHs in the Milky Way present a greater observational challenge. To date, no BH has been observed in a BHBH binary in the Milky Way, and so LISA could provide the first detection of a Galactic BHBH. The only confirmed BHs in our galaxy have been discovered as components of X-ray binaries with companion stars (e.g. Bolton 1972; Webster & Murdin 1972). These detections have observed BHs with masses mainly constrained between 5 and $10 M_{\odot}$ (Corral-Santana et al. 2016), a stark contrast to the more massive BHs observed with LIGO/Virgo that tend to contain at least one BH with a mass greater than $10 M_{\odot}$ (Abbott et al. 2020b). These observations of X-ray binaries suggest the presence of a lower mass gap (from 2-5 M_{\odot}) in which there are no strong candidates for either black holes or neutron stars (Özel et al. 2010; Farr et al. 2011) but the gap's existence remains an open question (e.g. Kreidberg et al. 2012; Mandel & Müller 2020). Recently there has also been increased discussion over the maximum BH mass in our galaxy, with the claims of a $70 M_{\odot}$ BH (Liu et al. 2019) which has subsequently been challenged (El-Badry & Quataert 2020; Abdul-Masih et al. 2020; Shenar et al. 2020; Eldridge et al. 2020, see also Liu et al. 2020) and revised measurements of the mass of Cygnus X-1 (Miller-Jones et al. 2021). A sample of BHBHs detected with LISA could possibly help to constrain the BH mass distribution.

One particularly interesting class of potential LISA sources is BHNSs. With the recent detection of two BHNSs by the LIGO scientific collaboration, the existence of these DCOs has been confirmed (The LIGO Scientific Collaboration et al. 2021b). However, with only two detections (not including the low-confidence candidate GW190426, Abbott et al. 2020b, or GW190425, GW190814 and GW190917 which have not been ruled out as BHNSs, Abbott et al. 2020a,c; The LIGO Scientific Collaboration et al. 2021a) and no electromagnetic counterparts, the formation rate and properties of BHNSs are still uncertain. Current predictions for the merger rate of BHNSs range across three orders of magnitude (e.g. Abadie et al. 2010; Mandel & Broekgaarden 2021) so the number of detections in LISA will be important in reducing this uncertainty, thereby refining our understanding of the remnants and evolution of massive stars. A distinctly exciting possibility for BHNSs is the detection of a pulsar–BH system or millisecond pulsar–BH system (Narayan et al. 1991; Pol et al. 2021). These systems could be observed not only by LISA, but also radio telescopes such as MeerKAT and the Square Kilometre Array (SKA, Dewdney et al. 2009), which would help to improve the measurement of individual system parameters and to constrain uncertain binary evolution

processes (e.g. Pfahl et al. 2005; Chattopadhyay et al. 2020). Moreover, the pulsar acts as an ultraprecise clock around a BH and thus a pulsar–BH system provides stringent tests of theories of gravity (Keane et al. 2015). For the purposes of this investigation, we consider the ‘classical’ isolated binary evolution channel (e.g. Tutukov & Yungelson 1973, 1993; Smarr & Blandford 1976; Srinivasan 1989; Kalogera et al. 2007; Belczynski et al. 2016) in which double compact objects are formed following common-envelope ejection or a phase of highly non-conservative mass transfer (van den Heuvel 2011; van den Heuvel et al. 2017). We do not, however, account for several alternative proposed formation channels, which could affect the rate and distribution of detectable NS and BH binaries in LISA. These channels include: dynamical formation in dense star clusters (e.g. Sigurdsson & Hernquist 1993; Portegies Zwart & McMillan 2000; Miller & Lauburg 2009; Rodriguez et al. 2015), young/open star clusters (e.g. Ziosi et al. 2014; Di Carlo et al. 2020; Banerjee 2020; Rastello et al. 2020, 2021) and (active) galactic nuclei discs (e.g. Morris 1993; Antonini & Rasio 2016; McKernan et al. 2020), isolated (hierarchical) triple evolution involving Kozai-Lidov oscillations (e.g. Stephan et al. 2016; Silsbee & Tremaine 2017; Antonini et al. 2017; Toonen et al. 2020), and chemically homogenous evolution through efficient rotational mixing (e.g. de Mink et al. 2009; Mandel & de Mink 2016; Marchant et al. 2016, 2017; du Buisson et al. 2020).

In this paper, we present models for the detection rate and distribution of binary properties (masses, frequency, eccentricity, distance, merger time) of BHBHs, BHNSs and NSNSs formed through isolated binary evolution in the Milky Way. We explore the effect of varying physical assumptions in our population synthesis model on our results as well as discuss the effect of extending the LISA mission length and the prospects for distinguishing DCO detections from the WDWD background.

Earlier work on BHBHs, BHNSs and NSNSs in LISA has used a variety of population synthesis codes, Milky Way models and LISA specifications, resulting in a wide range of predictions (Nelemans et al. 2001; Belczynski et al. 2010; Liu & Zhang 2014; Lamberts et al. 2019; Lau et al. 2020; Breivik et al. 2020; Sesana et al. 2020; Shao & Li 2021). We build upon previous efforts but with several important improvements. We explore the effects of varying binary physics assumptions by repeating our analysis for 20 different models and comparing the effects on the detection rate and distributions of source parameters (Broekgaarden et al. 2021a,b). We use a model for the Milky Way that accounts for the chemical enrichment history and is calibrated on the APOGEE survey (Majewski et al. 2017; Frankel et al. 2018), whereas most

others did not consider the effect of metallicity in detail (see however Lamberts et al. 2019; Sesana et al. 2020). We provide a detailed treatment of the eccentricity of detectable sources, both for the inspiral evolution as well as gravitational wave signal during the LISA mission. Moreover, the grid of binary population synthesis simulations that we use is the most extensive of its kind to date and makes use of the adaptive sampling algorithm STROOPWAFEL (Broekgaarden et al. 2019, 2021a). Overall over 2 billion massive binaries were simulated to produce the DCO populations used in this work. We find that this large number of simulations is important to reduce the sampling noise even when using adaptive importance sampling.

All data related to the predictions made in this study are publicly available on Zenodo at Wagg et al. (2021), as are the populations used in our simulations at Broekgaarden (2021a, BHBH) Broekgaarden (2021b, BHNS) and Broekgaarden (2021c, NSNS). We make all code used to produce our results available in a Github repository [P¹](#). In addition, the repository contains step-by-step Jupyter notebooks that explain how to reproduce and change each figure in the paper. In a companion paper, Wagg et al. (2021), we present LEGWORK², the LISA Evolution and Gravitational Wave Orbit Kit, a python package designed for making predictions for the detection of sources with LISA, which we use in this work.

Our paper is structured as follows. In Section 2, we describe the methods for synthesising a population of binaries, the variations of physical assumptions that we consider, how we simulate the Milky Way distribution of DCOs and our methods for calculating a detection rate for LISA. We present the main results for our fiducial model in Section 3, before exploring the variations in the detectable population when changing our physical assumptions in Section 4. In Section 5 we discuss these results. In Section 6, we compare and contrast our methods and findings to previous work and finish with our conclusions in Section 7.

2. METHOD

To produce predictions for the DCOs that are detectable with LISA, we use a synthesised population of DCOs, simulated using the methods described in Section 2.1. In Section 2.2 we describe our model for the Milky Way and how we place DCOs in randomly sampled Milky Way instances. We evolve the orbit of each DCO in a Milky Way instance up to the LISA mission

¹<https://github.com/TomWagg/detecting-DCOs-in-LISA>

²<https://legwork.readthedocs.io>

and calculate the detection rate for that instance using the methods presented in Section 2.3.

2.1. Binary population synthesis

We use the grid of 20 binary population synthesis simulations recently presented in Broekgaarden et al. (2021a,b). This grid of simulations is synthesised using the rapid population synthesis code COMPAS (Stevenson et al. 2017; Vigna-Gómez et al. 2018; Stevenson et al. 2019; Broekgaarden et al. 2019). COMPAS follows the approach of the population synthesis code BSE (Hurley et al. 2000, 2002) and uses fitting formula and rapid algorithms to efficiently predict the final fate of binary systems. The code is open source and documented in the papers listed above, the online documentation³ and in the methods paper (Team COMPAS: J. Riley et al. 2021). We summarise the main assumptions and settings relevant for this work in Appendix A.

The result of the simulations is a sample of binaries, which, for each metallicity Z , have N_{binaries} binaries with parameters

$$\mathbf{b}_{Z,i} = \{m_1, m_2, a_{\text{DCO}}, e_{\text{DCO}}, t_{\text{evolve}}, t_{\text{inspiral}}, w\}, \quad (1)$$

for $i = 1, 2, \dots, N_{\text{binaries}}$, where m_1 and m_2 are the primary and secondary masses, a_{DCO} and e_{DCO} are the semi-major axis and eccentricity at the moment of double compact object (DCO) formation, t_{evolve} is the time between the binary's zero-age main sequence and DCO formation, t_{inspiral} is the time between DCO formation (that is, immediately after the second supernova in the system) and gravitational-wave merger and w is the adaptive importance sampling weight assigned by STROOPWAFEL (Broekgaarden et al. 2019, Eq. 7). We sample from these sets of parameters when creating synthetic galaxies.

2.2. Galaxy synthesis

In order to estimate a detection rate of DCOs with statistical uncertainties, we create a series of random instances of the Milky Way, each populated with a subsample drawn (with replacement) from the synthesised binaries described in Section 2.1.

Most previous studies that predict a detection rate for LISA place binaries in the Milky Way independently of their age or evolution. We improve upon this as the first study to use an empirically-informed analytical model of the Milky Way that takes into account the galaxy's enrichment history by applying the metallicity-radius-time relation from Frankel et al. (2018). Those authors

developed this relation in order to measure the global efficiency of radial migration in the Milky Way and calibrated it using a sample of red clump stars measured with APOGEE (Majewski et al. 2017).

In Section 2.2.1, we outline our model for the Milky Way and in Section 2.2.2 we explain how we combine our population of synthesised DCOs with this Milky Way model.

2.2.1. Milky Way model

Fig. 1 shows the distributions and relations outlined in this section and also displays an example random galaxy drawn using this model.

Our model for the Milky Way accounts for the low-[α/Fe]⁴ disc, high-[α/Fe] disc and a central component approximating a bar/bulge. The low- and high-[α/Fe] discs are often also referred to as the thin and thick discs because the stellar vertical distribution is better fit by a double exponential rather than a single one. However, this doesn't allow one to assign a star to either the thin or thick disk purely based on its height above the Galactic plane. Therefore, we instead use the chemical definition of the two disks (applying the [α/Fe] nomenclature) as there is a clear bimodal distribution in the chemical plane, allowing stars to be assigned to each of the disc components based on their chemical abundances. For each of the three components, we use a separate star formation history and spatial distribution, which we combine into a single model, weighting each component by its present-day stellar mass. Licquia & Newman (2015) gives that the stellar mass of the bulge is $0.9 \times 10^{10} M_\odot$ and the stellar mass of the disc is $5.2 \times 10^{10} M_\odot$, which we split equally between the low- and high-[α/Fe] discs (e.g., Snaith et al. 2014).

Star formation history: We use an exponentially declining star formation history (Frankel et al. 2018) (inspired by the average cosmic star formation history) for the combined low- and high-[α/Fe] discs,

$$p(\tau) \propto \exp\left(-\frac{(\tau_m - \tau)}{\tau_{\text{SFR}}}\right), \quad (2)$$

where τ is the lookback time (the amount of time elapsed between the binary's zero-age main sequence and today), $\tau_m = 12$ Gyr is the assumed age of the Milky Way and $\tau_{\text{SFR}} = 6.8$ Gyr is the star formation timescale (Frankel et al. 2018). The two discs form stars in mutually exclusive time periods, such that the high-[α/Fe] disc forms stars in the early history of the galaxy (8–12 Gyr ago) and the low-[α/Fe] disc forms stars more

³<https://compas.science>

⁴Nomenclature used to describe the enhancement of α elements compared to iron in stellar atmospheres

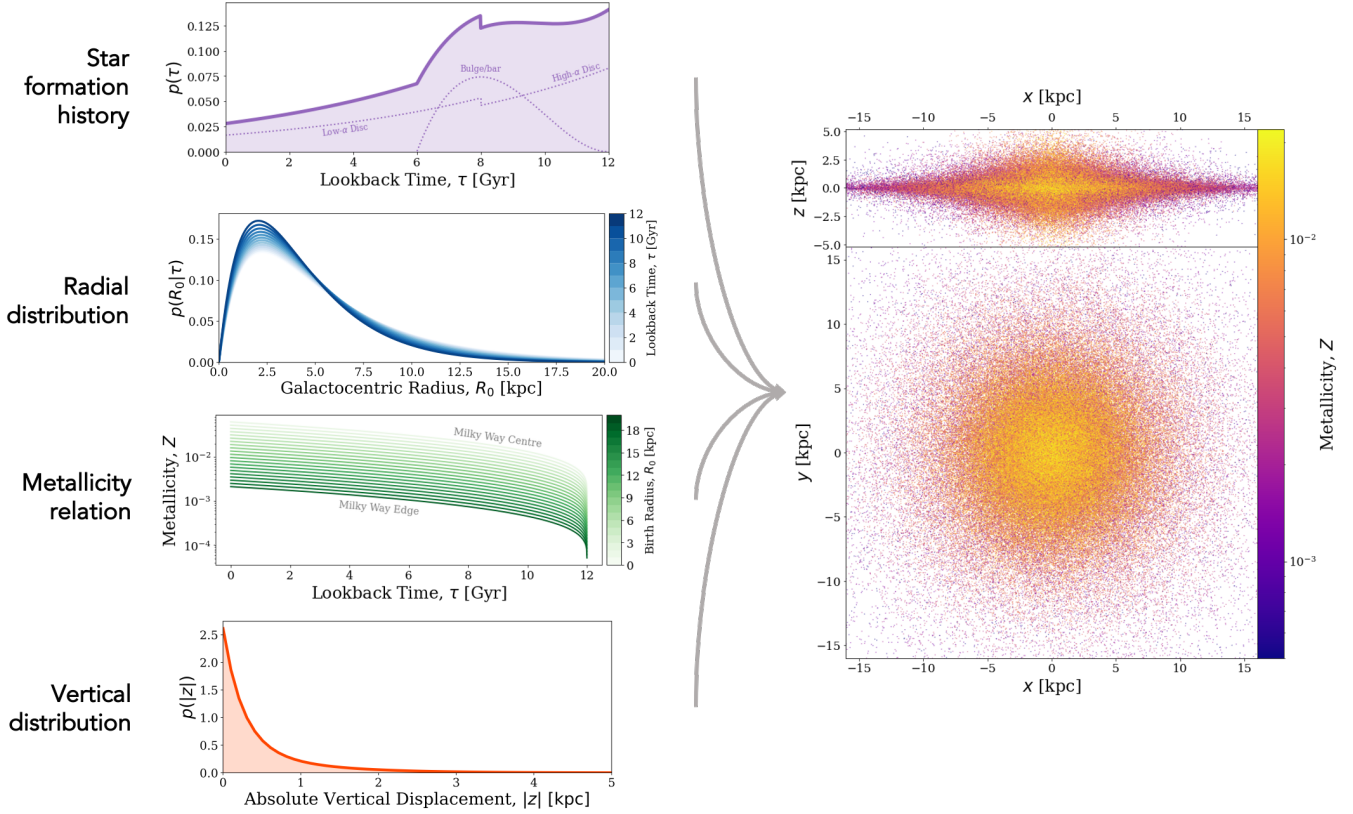


Figure 1. A schematic illustrating how we model the Milky Way. The left panel illustrates the different model aspects: star formation history of three galactic components (individually shown in the dotted lines), radial distribution, metallicity-radius-time relation, and height distribution. The right panel shows an example instance of the Milky Way with 250000 binaries shown as points coloured by metallicity. The top panel shows a side-on view and the bottom panel a face-on view.

recently (0–8 Gyr ago). Both distributions are normalised so that an equal amount of mass is formed in each of the two components over their respective star forming periods.

The star formation history of the Milky Way bulge (which we assume here to be dominated by the central bar) has many uncertainties due to the (1) sizeable age measurement uncertainties at large ages in observational studies, (2) complex selection processes affecting the observed age distributions, and (3) formation mechanisms that are still under debate. However, the central bar was shown to contain stars with an extended age range, with most observed stars between 6 and 12 Gyr with a younger tail of ages that could come from the subsequent secular growth of the Galactic bar (e.g., Bovy et al. 2019). To model the bar’s age distribution more realistically than in previous studies (which assume an old bulge coming from a single starburst), we choose to adopt a more extended star formation history using a $\beta(2, 3)$ distribution, shifted and scaled such that stars are only formed in the range [6, 12] Gyr. We show these distributions in the top left panel of Fig. 1.

Radial distribution: For each of the three components we employ the same single exponential distribution (but with different scale lengths)

$$p(R) = \exp\left(-\frac{R}{R_d}\right) \frac{R}{R_d^2}, \quad (3)$$

where R is the Galactocentric radius and R_d is the scale length of the component. For the low-[α /Fe] disc, we set $R_d = R_{\text{exp}}(\tau)$, where $R_{\text{exp}}(\tau)$ is the scale length presented in Frankel et al. (2018, Eq. 6)

$$R_{\text{exp}}(\tau) = 4 \text{ kpc} \left(1 - \alpha_{R_{\text{exp}}} \left(\frac{\tau}{8 \text{ Gyr}}\right)\right), \quad (4)$$

where $\alpha_{R_{\text{exp}}} = 0.3$ is the inside-out growth parameter⁵. This scale length accounts for the inside-out growth of the low-[α /Fe] disc and hence is age dependent. We assume $R_d = (1/0.43)$ kpc for the high-[α /Fe] disc (Bovy et al. 2016, Table 1) and $R_d = 1.5$ kpc for the bar component (Bovy et al. 2019). We show the combination

⁵We find that $R_{\text{exp}}(\tau) = 4$ kpc fits the data well and adopt this value rather than the 3 kpc quoted in Frankel et al. (2018), which was a fixed parameter (not a fit).

364 of these distributions in the second panel on the left in
 365 Fig. 1.

Vertical distribution: Similar to the radial distribution, we use the same single exponential distribution (but with different scale heights) for each component, given by

$$p(|z|) = \frac{1}{z_d} \exp\left(-\frac{|z|}{z_d}\right), \quad (5)$$

366 where z is the vertical displacement above the Galactic
 367 plane and z_d is the scale height. We set $z_d = 0.3$ kpc for
 368 the low-[α /Fe] disc (McMillan 2011) and $z_d = 0.95$ kpc
 369 for the high-[α /Fe] disc (Bovy et al. 2016). For the bar,
 370 we set $z_d = 0.2$ kpc (Wegg et al. 2015). We show the
 371 combination of these distributions in the bottom left
 372 panel of Fig. 1.

Metallicity-radius-time relation: To account for the chemical enrichment of star forming gas as the Milky Way evolves, we adopt the relation given by (Frankel et al. 2018, Eq. 7)

$$\begin{aligned} [\text{Fe}/\text{H}](R, \tau) &= F_m + \nabla[\text{Fe}/\text{H}]R \\ &- \left(F_m + \nabla[\text{Fe}/\text{H}]R_{[\text{Fe}/\text{H}]=0}^{\text{now}} \right) f(\tau), \end{aligned} \quad (6)$$

where

$$f(\tau) = \left(1 - \frac{\tau}{\tau_m}\right)^{\gamma_{[\text{Fe}/\text{H}]}} , \quad (7)$$

$F_m = -1$ dex is the metallicity of the gas at the center of the disc at $\tau = \tau_m$, $\nabla[\text{Fe}/\text{H}] = -0.075$ kpc $^{-1}$ is the metallicity gradient, $R_{[\text{Fe}/\text{H}]=0}^{\text{now}} = 8.7$ kpc is the radius at which the present day metallicity is solar and $\gamma_{[\text{Fe}/\text{H}]} = 0.3$ sets the time dependence of the chemical enrichment. We convert this to the representation of metallicity that we use in this paper by applying (e.g. Bertelli et al. 1994)

$$\log_{10}(Z) = 0.977[\text{Fe}/\text{H}] + \log_{10}(Z_\odot). \quad (8)$$

373 Although Frankel et al. (2018) only fit this model for
 374 the low-[α /Fe] disc, we also use this metallicity-radius-
 375 time relation for the high- α disc and the bar, but focus-
 376 ing on the chemical tracks more representative to the
 377 inner disc and large ages. Sharma et al. (2020) showed
 378 that using a simple continuous model for both the low-
 379 and high-[α /Fe] discs, the Milky Way abundance dis-
 380 tributions could be well reproduced. Empirically, the
 381 abundance tracks in the [α /Fe]-[Fe/H] plane (and other
 382 elements) of the stars in the bulge/bar follow the same
 383 track as those of the old stars in the Solar neighbour-
 384 hood (Griffith et al. 2021; Bovy et al. 2019, Fig. 7.),
 385 which motivates our modelling choice to use the same
 386 metallicity-radius-time relation.

2.2.2. Combining population and galaxy synthesis

For each Milky Way instance, we randomly sample the following set of parameters

$$\mathbf{g}_j = \{\tau, R, Z, z, \theta\} \quad (9)$$

388 for $j = 1, 2, \dots, N_{\text{MW}}$, where we set $N_{\text{MW}} = 2 \times 10^5$,
 389 τ, R, Z and z are defined and sampled using the dis-
 390 tribution functions specified in Section 2.2.1, θ is the
 391 azimuthal angle sampled uniformly on $[0, 2\pi)$ and Z is
 392 the metallicity. Fig. 1 shows an example of a random
 393 Milky Way instance created with these distributions.
 394 This shows how these distributions translate to positions
 395 and illustrates the gradient in metallicity over radius.

396 We match each set of galaxy parameters \mathbf{g}_j , to a ran-
 397 dom set of binary parameters $\mathbf{b}_{Z,i}$, by drawing a binary
 398 from the closest metallicity bin to the metallicity in \mathbf{g}_j .
 399 If the metallicity in \mathbf{g}_j is below the minimum COMPAS
 400 metallicity bin ($Z = 10^{-4}$), we use this minimum bin.
 401 If the metallicity in \mathbf{g}_j is above the maximum COMPAS
 402 metallicity bin ($Z = 0.03$), we use a randomly selected
 403 bin from the five highest metallicity bins⁶.

404 Each binary is likely to move from its birth orbit.
 405 Although all stars in the Galactic disc experience ra-
 406 dial migration (Sellwood & Binney 2002; Frankel et al.
 407 2018), DCOs generally experience stronger dynamical
 408 evolution as a result of the effects of both Blaauw kicks
 409 (Blaauw 1961) and natal kicks (e.g. Hobbs et al. 2005).

410 The magnitude of the systemic kicks are typically
 411 small compared to the initial circular velocity of a bi-
 412 nary at each Galactocentric radius. Therefore, we ex-
 413 pect that kicks will not significantly alter the overall
 414 distribution of their positions (see however, e.g., Brandt
 415 & Podsiadlowski 1995; Abbott et al. 2017b). Given this,
 416 and for the sake of computational efficiency, we do not
 417 account for the displacement due to systemic kicks in
 418 our analysis.

2.3. Gravitational wave detection

419 We use the Python package **LEGWORK** (Wagg et al.
 420 2021) to evolve binaries and calculate their LISA de-
 421 teability. For a full derivation of the equations given
 422 below see (Wagg et al. 2021, Section 3), or the LEG-
 423 WORK documentation [\[2\]](#).

2.3.1. Inspiral evolution

6

We spread the binaries over the five highest bins, rather than just the highest bin, as we found that using a single bin led to unphysical artifacts in our results. These artifacts arose because the small population of binaries in the highest bin were oversampled.

426 Each binary loses orbital energy to gravitational waves
 427 throughout its lifetime. This causes the binary to shrink
 428 and circularise over time. In order to assess the de-
 429 tectability of a binary, we need to know its eccentricity
 430 and frequency at the time of the LISA mission. For each
 431 binary in our simulated Milky Way, we know that the
 432 time from DCO formation to today is $\tau - t_{\text{evolve}}$ and that
 433 the initial eccentricity and semi-major axis are e_{DCO} and
 434 a_{DCO} . We find the eccentricity of the binary at the start
 435 of the LISA mission, e_{LISA} , by numerically integrating
 436 its time derivative (Peters 1964, Eq. 5.13) given the ini-
 437 tial conditions. This can be converted to the semi-major
 438 axis at the start of LISA, a_{LISA} (Peters 1964, Eq. 5.11),
 439 which in turn gives the orbital frequency, $f_{\text{orb}, \text{LISA}}$, by
 440 Kepler's third law since we know the component masses.

441 2.3.2. Binary detectability

We define a binary as detectable if its gravitational wave signal has a signal-to-noise ratio (SNR) of greater than 7 by the end of the LISA mission (e.g. Breivik et al. 2020; Korol et al. 2020). The sky-, polarisation- and orientation-averaged signal-to-noise ratio, ρ , of an inspiraling binary can be calculated with the following (e.g. Finn & Thorne 2000)

$$\rho^2 = \sum_{n=1}^{\infty} \int_{f_{n,i}}^{f_{n,f}} \frac{h_{c,n}^2}{f_n^2 S_n(f_n)} df_n, \quad (10)$$

where n is a harmonic of the gravitational wave signal, $f_n = n \cdot f_{\text{orb}}$ is the frequency of the n^{th} harmonic of the gravitational wave signal, f_{orb} is the orbital frequency, $S_n(f_n)$ is the LISA sensitivity curve at frequency f_n (e.g. Robson et al. 2019) and $h_{c,n}$ is the characteristic strain of the n^{th} harmonic, given by (e.g. Barack & Cutler 2004)

$$h_{c,n}^2 = \frac{2^{5/3}}{3\pi^{4/3}} \frac{(G\mathcal{M}_c)^{5/3}}{c^3 D_L^2} \frac{1}{f_{\text{orb}}^{1/3}} \frac{g(n,e)}{nF(e)}, \quad (11)$$

where D_L is the luminosity distance to the source, f_{orb} is the orbital frequency, $g(n,e)$ and $F(e)$ are given in Peters & Mathews (1963) and \mathcal{M}_c is the chirp mass, defined as

$$\mathcal{M}_c = \frac{(m_1 m_2)^{3/5}}{(m_1 + m_2)^{1/5}}. \quad (12)$$

442 Note that increasing the length of the LISA mission
 443 allows more time for a DCO to evolve over the mis-
 444 sion. Therefore the frequency limits in Eq. 10 are dic-
 445 tated by the LISA mission length. The SNR generally
 446 scales as $\sqrt{T_{\text{obs}}}$ (with exceptions for sources very close
 447 to merging) and thus the SNR of a typical source in a
 448 10-year LISA mission is approximately 1.58 ($=\sqrt{10/4}$)
 449 times stronger than in a 4-year mission.

450 We use LEGWORK (Wagg et al. 2021) to calculate
 451 the signal-to-noise ratio for each binary and the package
 452 ensures that enough harmonics are computed for each
 453 binary such that the error on the gravitational-wave lu-
 454 minosity remains below 1%.

455 2.3.3. Detection rate calculation

456 For each physics variation model and DCO type, we
 457 first convert the COMPAS simulation results into a total
 458 number of DCOs in the Milky Way, N_{DCO} . We do this
 459 by integrating the full mass and period distributions and
 460 stars and normalising to the total Milky Way mass. For
 461 more details see Appendix B.

We then determine the fraction of binaries that are detectable in each Milky Way instance by summing the adaptive importance sampling weights of the binaries that have an SNR greater than 7, and dividing by the total weights in the simulation. We multiply this fraction by N_{DCO} to find a detection rate (which we write as a total number of detections per LISA mission)

$$N_{\text{detect}} = \frac{\sum_{i=0}^{N_{\text{MW}}} w_i \phi(i)}{\sum_{i=0}^{N_{\text{MW}}} w_i} N_{\text{DCO}}, \quad (13)$$

462 where $\phi(i) = 1$ if a binary is detectable and 0 other-
 463 wise. We calculate the detection rate by Monte Carlo
 464 sampling 2500 Milky Way instances (each containing
 465 200,000 DCOs) for each DCO type and every physics
 466 variation in order to obtain values for the uncertainty
 467 on the expected detection rate.

468 3. RESULTS I - PREDICTIONS FOR LISA 469 SOURCES

470 In this section we present our predictions for the popu-
 471 lation of detectable LISA sources for our fiducial model.
 472 In total we expect, on average, 124 detections in a 4-
 473 year LISA mission, of which 74, 42 and 8 are BHBs,
 474 BHNSs and NSNSs respectively, based on our fiducial
 475 simulations. In the remainder of this section, we discuss
 476 where the sources are expected relative to LISA's sensi-
 477 tivity curve (Sec. 3.1), their properties (Sec. 3.2), their
 478 locations in the Milky Way (Sec. 3.3), their formation
 479 channels (Sec. 3.4) and finally we discuss the expected
 480 SNR and how accurately we expect that the parameters
 481 can be measured (Sec. 3.5). Note that all results shown
 482 in this section are based on our fiducial simulations. A
 483 discussion of the impact of variations in the physics as-
 484 sumptions is provided in Sec. 4.

485 3.1. The LISA sensitivity curve and the population of 486 detectable sources

487 We show the expected LISA sensitivity curve (Rob-
 488 son et al. 2019) in Fig. 2, which includes the confu-

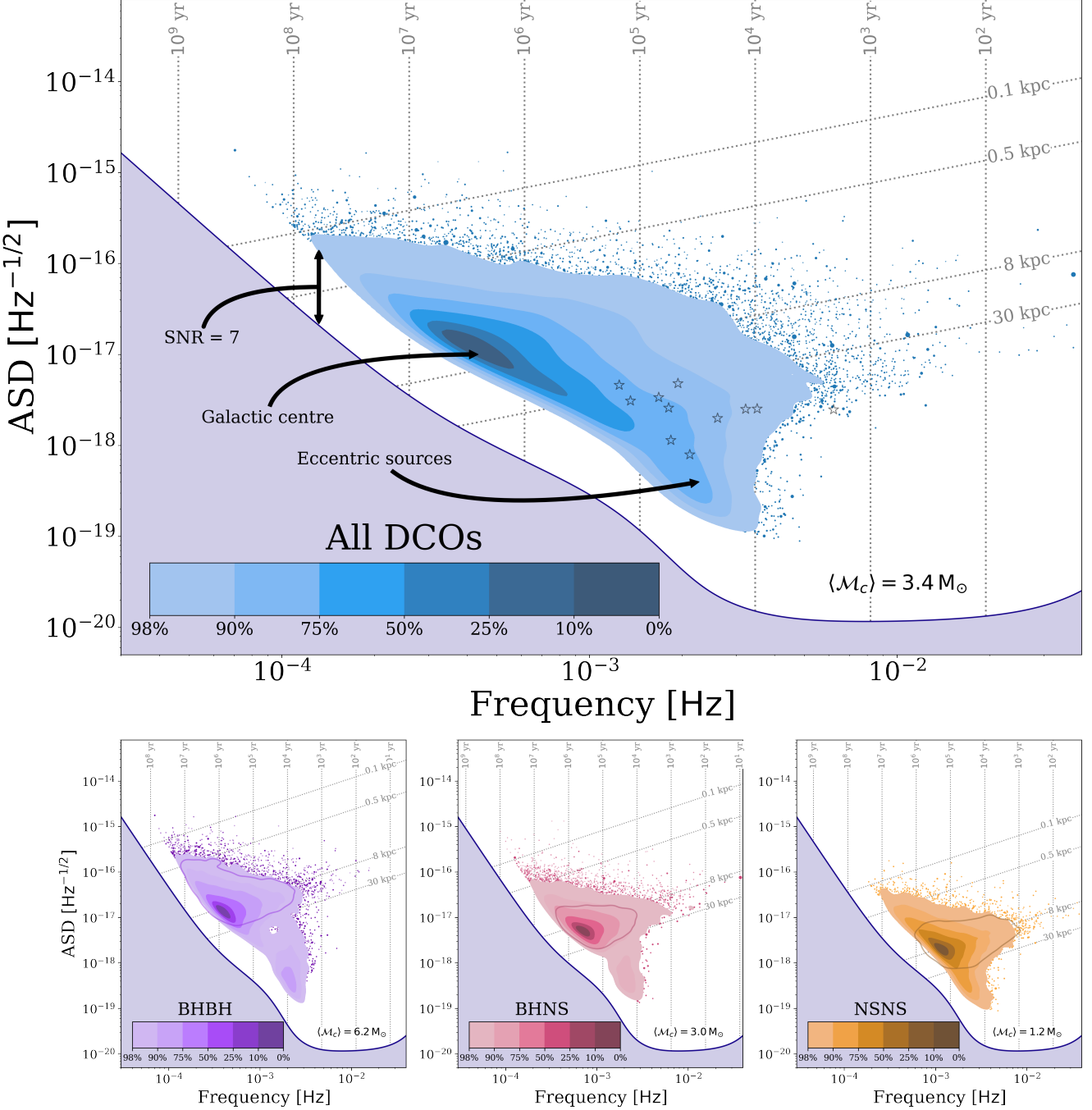


Figure 2. The LISA sensitivity curve is shown together with the density distribution of the characteristic strain and the dominant frequency for all detectable sources in our simulations (top) and separated by type (bottom). Contours show the percentage of the population enclosed. The remaining 2% of the population is shown as dots with a size that scales with the sampling weight. To guide the interpretation, we show reference lines marking where a circular binary would reside for a given distance (diagonal line) and remaining inspiral time (vertical lines), assuming an average chirp mass (\mathcal{M}_c) , orientation and sky location. The coloured lines in the bottom panels show a contour that encloses 90% of the population that is circular. LISA verification binaries are overplotted in the top panel (star symbols). See also Fig. F2 and Sec. 3.1 for a discussion.

sion noise arising from the Galactic WDWD population, and overplot our predictions for the distribution of detectable sources. Eccentric systems emit gravitational waves in multiple harmonic frequencies (nf_{orb} , with $n = 2, 3, \dots$). We choose to plot them at the x -coordinate that corresponds to the frequency of the harmonic that individually accumulates the largest SNR. For circular systems, the x -coordinate simply corresponds to $2f_{\text{orb}}$. The y -coordinate indicates the strength of the signal (or to be more precise, the amplitude spectral density, ASD), including the contribution from *all* harmonics.

For reference, we show dotted lines to indicate where a hypothetical binary system would reside assuming a given distance from earth (diagonal lines) and a fixed remaining inspiral time (vertical lines). For each line we assume the binary is circular and has a chirp mass equal to the average of the sample ($\langle M_c \rangle$, annotated in each panel). We also overplot the LISA verification binaries (star symbols, Kupfer et al. 2018).

We observe several features in Fig. 2 that are worth discussing and explaining. We note that some of these have also been described in earlier studies (see Sec. 6). Firstly, we note the empty band that separates the LISA sensitivity curve and the detectable population. This is the result of the criteria for detection where we require $\text{SNR} > 7$.

We further note that the detectable population is concentrated on the left side of LISA’s sensitivity window. The peak is located at a frequency of about 0.4 mHz, which is much lower than the frequency where LISA will be most sensitive (about 10 mHz). This can be understood from the acceleration of inspiraling DCOs as they evolve towards higher frequencies. DCOs typically form with wide orbits (low frequencies) that would not be detectable yet. Their orbits shrink as they lose angular momentum in the form of gravitational waves leading to an increase of their orbital frequency until they become detectable. These systems are increasingly rare because they evolve faster and faster towards higher frequency as the inspiral accelerates, even though the signal emitted by a more compact binary is stronger (Peters 1964). The vertical grid lines show these rapidly decreasing inspiral times at increasing frequencies. Most of the population is thus expected to reside at low frequencies.

In the lower three panels, we show the contributions of the different types of sources. Comparing them, one can observe the shift in the frequency at which the peak is located, at 0.3 mHz, 0.7 mHz and 1 mHz for BHBH, BHNS and NSNS systems respectively. This is a result of the difference in chirp mass. A higher mass system

can emit at lower frequency and still produce the minimum SNR needed for detection. We note that this effect can be used to distinguish the heavier DCOs that we discuss in this work from WDWD systems, at least probabilistically (see Sec. 5.1.1). In the same way, this also explains the offset in frequency between the population of sources we predict and the LISA verification binaries.

Inspecting the dotted reference lines, we note that the peak of the density distribution of observable sources coincides with the location expected for circular systems at 8 kpc, which is the distance to the centre of the Milky Way. As can be seen best in the lower panels, the reference lines for 0.1 and 30 kpc enclose the majority of systems, as expected given the dimensions of the Milky Way.

There is a distinct subpopulation of binaries, most clearly visible in the lower panels as an offshoot that extends downwards to ASDs of $10^{-19} \text{ Hz}^{-1/2}$, especially around 2 mHz. This offshoot is almost uniquely composed of eccentric binaries, as can be seen in Fig. F2, which shows a similar figure but colouring individual systems by their eccentricity. This can also be seen, albeit indirectly, from the contour lines shown in the bottom panels of Fig. 2, which encompass 90% of the *circular* sources in each population. This contour does not include the offshoot. We conclude that eccentric sources occupy a very different region in this diagram.

3.2. Properties of the detectable systems

In Fig. 3, we show the 1D distribution of several individual parameters of the population of detectable binaries together with the 1- and 2- σ uncertainties obtained via bootstrapping. These uncertainties represent the fluctuations in our results over different random instances of the Milky Way. The distributions shown here are approximated by kernel density estimators, corrected for edge effects by mirroring the sample (Schuster 1985).

Orbital Frequency—The orbital frequency distributions for BHBHs, BHNSs and NSNSs (Fig. 3a) peak at progressively increasing frequencies. As mentioned in Sec. 3.1, this is because a higher mass DCO at the same distance and eccentricity requires a lower frequency to produce the same signal-to-noise ratio and thus be detected. The distributions appear nearly symmetric, but closer inspections shows that the left hand side is more populated, which can be seen most clearly in the curve for the BHBHs. This is due to the contribution of highly eccentric binaries, which are most abundant in the BHBH population. These systems are still detectable by LISA, despite their low orbital frequency,

as the high eccentricity means that the majority of the GW signal is emitted at higher harmonics, where LISA is more sensitive.

Black Hole Mass—In Fig. 3b, we show the distribution masses of individual black holes that are part of BHNS and BHBH systems. The distribution for BHBH shows a bimodality. This results from the two contributions of the more and less massive BHs in BHBH systems, which peak at around $8 M_{\odot}$ and $3.5 M_{\odot}$ respectively as shown by the dotted lines (see also our discussion of the mass ratios below).

For both the BHBHs and BHNSs, we see that the black hole mass distribution favours low masses. About 90% of BHs have masses below $11 M_{\odot}$, in our fiducial simulations shown here. This is in stark contrast with observations from ground-based GW detectors, where heavy BHs with masses of about $30 M_{\odot}$ and higher have been common. There are two main reasons for this discrepancy. First, the population of BHs in the Milky Way (and, in particular, those detectable by LISA due to their recent formation times, see Fig. 3e) primarily come from progenitors that formed from high metallicity gas according to our simulations. Stellar winds are stronger at high metallicity leading to increased mass loss. This affects the mass of the most massive black holes that can be formed (Belczynski et al. 2010). Secondly, ground-based detectors are strongly biased towards high mass systems, since they can be detected out to larger distances and thus a greater volume is probed. In contrast, LISA has no such bias and is, in principle, sensitive to inspiraling BHBHs throughout the entire Milky Way regardless of their mass, as long as we catch them when they are emitting in the LISA band. For this reason, LISA is more likely to detect the more common lower mass BHBHs.

We also note that our BH mass distribution extends down below $5 M_{\odot}$ to $2.5 M_{\odot}$ which is our fiducial maximum neutron star mass. The BHs in this simulation fill the so-called “lower mass gap” marked as a grey band (Özel et al. 2010; Farr et al. 2011), see also Shao & Li (2021) who recently also pointed this out. This prediction is sensitive to adopted model for fallback during the SN explosion as we discuss this further in Section 4.2.1.

Mass Ratio—The mass ratio distributions for each DCO type are very distinct from one another, as can be seen in Fig. 3c. The majority of NSNSs have a mass ratio close to unity, with 90% of systems having $q > 0.8$, where $q \equiv m_2/m_1$. The reason for the concentration around equal masses is that most NSs are formed either through electron-capture supernovae (ECSN) or from low mass stars in our simulations. We assume a remnant

mass for any NS formed through ECSN of $1.26 M_{\odot}$ (see Sec. A.2). The remnant mass prescription that we use assumes a fixed fallback mass for any star with a CO core mass less than $2.5 M_{\odot}$, such that many NSs end up with an identical mass of $1.278 M_{\odot}$ (see Fryer et al. 2012, Eq. 19). This means that many NSs are formed with equal masses and hence we see a mass ratio distribution peaked around unity.

In contrast, only 8% of detectable BHBHs are formed with $q > 0.8$ and the distribution peaks around $q = 0.4$. We find that the strong stellar winds in our (typically high-metallicity) progenitors are the reason behind this.

BHBHs with unequal masses typically come from progenitors that also had more extreme mass ratios at birth (90 and $30 M_{\odot}$ are typical for the progenitors of detectable BHBH systems in our simulations). The primary in such systems experiences strong mass loss by winds before filling its Roche lobe. This mostly happens during its early hydrogen-shell burning phase. The wind mainly reduces the mass of the envelope, but does not have a very strong effect on the core. By the time the primary fills its Roche lobe, it has become less massive and the mass ratio is closer to one. This favours stable mass transfer. The massive core of the primary star typically becomes the more massive BH. Accretion on the secondary star is limited and the secondary eventually provides the less massive black hole.

At the same time, stellar wind mass loss disfavours the formation of black holes with comparable masses. Such systems would have originated from progenitors that also started with comparable masses. The rather massive secondaries in these systems (especially after they accreted from the primary) experience very strong stellar wind mass loss due to LBV-like eruptions. This limits the amount by which they can expand (e.g. van Son et al. 2021). At the same time, wind mass loss (and also stable and more conservative mass transfer in these systems) lead to widening of the orbit. Both effects, the reduced expansion and increased widening of the orbit, tend to prevent the secondaries from being able to fill their Roche lobe. This thus limits the number of systems that experience the reverse mass transfer or common-envelope phase needed to shrink the orbits and make them tight enough to be detected as gravitational-wave sources.

We find that detectable BHNSs have even more unequal mass ratios. Moreover, the mass ratio distribution is bimodal, where the two peaks arise from two distinct formation scenarios. Around two thirds of detectable BHNSs experience at least one common-envelope event, whilst the last third are formed through only stable mass transfer. The first peak at $q = 0.18$ is from systems that

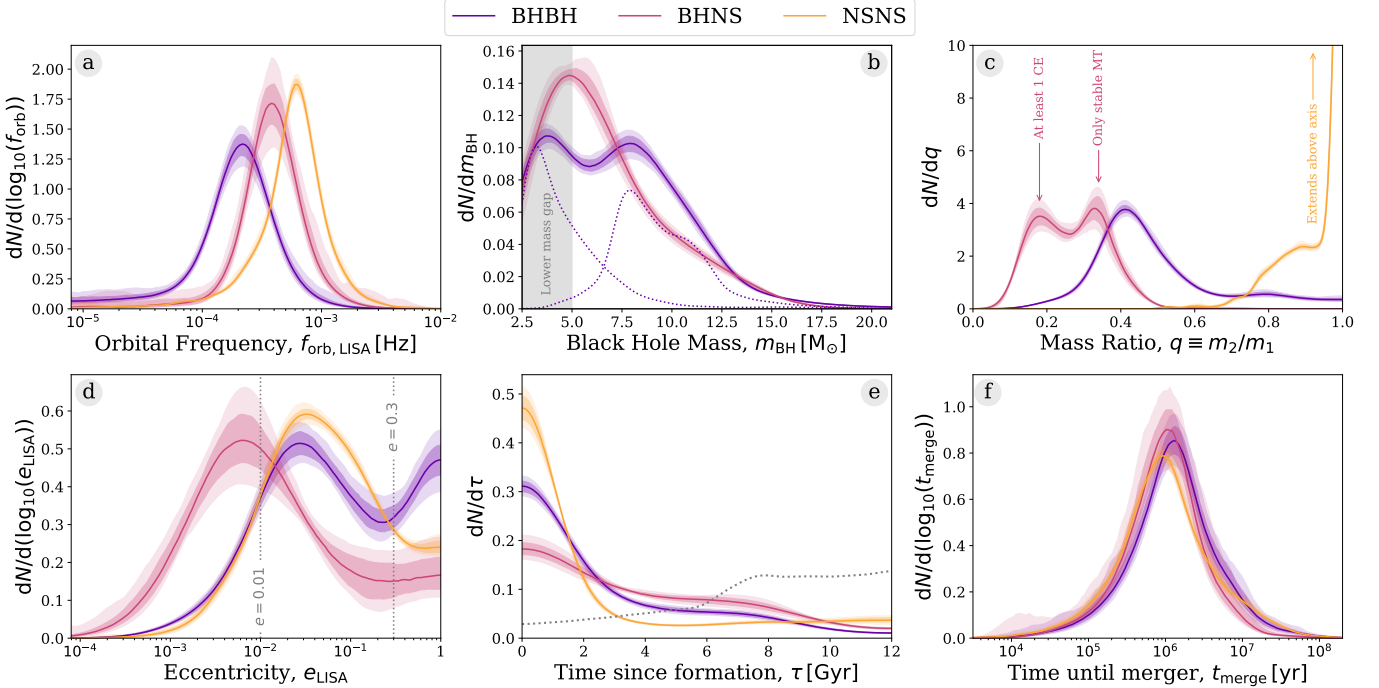


Figure 3. Properties of detectable systems for a 4-year LISA mission in our fiducial model. Each panel shows a kernel density estimator for a single property, coloured by DCO type. Each curve has been individually normalised. The shaded areas show the 1- and 2- σ sampling uncertainties (obtained via bootstrapping). The dotted lines in panel b show the individual primary and secondary mass distributions. The dotted line in panel e shows the star formation history we have assumed in our Milky Way model. See Sec. 3.2 for a discussion.

experience at least one common-envelope phase and occurs at the expected mass ratio, which approximately follows the mean BH mass ($\sim 6.5 M_{\odot}$) and NS mass ($\sim 1.2 M_{\odot}$). Yet we also see a second peak at higher mass ratios around $q = 0.34$, which arises from the fraction of the population that underwent only stable mass transfer phases. The stability of mass transfer depends on the mass ratio, preferentially forming systems with more equal masses, i.e. at higher q .

Eccentricity—In Fig. 3d we show the eccentricity distributions. We find that most systems (73%) will have eccentricities larger than 0.01 during the LISA mission, which should in principle be detectable according to Nishizawa et al. (2016). This means that we will potentially be able to use eccentricity to distinguish these sources from WDWDs, which are expected to have little to no eccentricity (see Sec. 5.1.1). We note that several previous studies assumed all systems to be circular when calculating the detection rates (e.g. Liu & Zhang 2014; Lamberts et al. 2018; Sesana et al. 2020). We discuss the impact of this assumption in Section 6.

For systems with eccentricities higher than $e \gtrsim 0.3$, most gravitational wave energy is emitted in higher harmonics. Such systems are more rare, but we find them to be significant among the BHBH population, where

they account for 21% of systems. Detectable BHBHs in our simulation (and, in particular, those that are eccentric) are primarily systems formed through the stable mass transfer channel (see Fig. F1). These systems are still relatively wide (compared to those formed through the CE channel) immediately prior to formation of the second BH, which makes them more easily affected by kicks. If the kick is oriented roughly in opposite direction to the orbital motion and has a velocity that is of similar magnitude as the orbital velocity, it will lead to the formation of a highly eccentric system.

It is rare to get such a “lucky kick”, but there are a few effects that favour this for BHBHs. The kicks of BHs are reduced by fallback and they are thus less likely to disrupt the system. Moreover, because of their higher masses, BHBHs can be observed already at lower orbital frequencies. This means that they have not had as much time to circularise and so still have significant eccentricity by the time of the LISA mission. Finally, LISA favours the detection of eccentric systems, if all other properties are held fixed. This is because the gravitational-wave emission is stronger (Eq. C2) and the energy is emitted at higher frequencies (Peters & Mathews 1963, Eq. 20) where LISA is more sensitive.

The lower abundance of highly eccentric systems among the NSNS and BHNS systems may seem counter-

intuitive since neutron stars are lower mass and would be more strongly affected by natal kicks, which one may expect to lead to more eccentric systems. However, the majority of NSs in our simulations are formed through ECSV and USSN and for these types of supernovae we draw from a Maxwellian with $\sigma_{\text{rms}}^{1D} = 30 \text{ km s}^{-1}$. Thus the kicks received by NSs in our simulations are often much smaller than for BHs.

Time since formation—In Fig. 3e we show how long ago the LISA detectable DCOs formed. Star formation was highest at early times 6–12 Gyr ago, after which it declined. In contrast, the LISA detectable DCOs primarily formed in the relatively *recent* history of our Milky Way, about 2 Gyr ago. This reflects the fact that binaries in our simulation typically take about a Gyr to merge.

When comparing the distribution of formation times for the three different DCO types we see that NSNSs are most strongly concentrated at recent times, followed by BHBHs and then BHNSs. To understand this it is helpful to consider how the inspiral time scales with various parameters (Peters 1964)

$$t_{\text{inspiral}} \propto \frac{a^4}{(m_1 + m_2)^3} \cdot \frac{q}{(1+q)^2} \cdot (1 - e^2)^{-7/2}. \quad (14)$$

The inspiral time depends most strongly on the separation at DCO formation, a , and this is where the three types also differ most strongly (see Fig. F3). The detectable NSNS systems have the tightest orbits at DCO formation. The median of the distribution of separations at DCO formation, $\langle a_{\text{DCO}} \rangle_{\text{med}}$, relate as 8:3:1 for detectable BHBH:BHNS:NSNS in our simulations. This results in increase of the inspiral time by a factor of about 4000:80:1. The total masses affect the inspiral time to the third power and this where the heavier BHBH systems are favoured. The median total masses differ by ratios of 6:4:1 for detectable BHBH:BHNS:NSNS in our simulations, impacting the inspiral times such that they are a factor of 200:60:1 shorter, partially counteracting the effect of the separations. The term depending on the mass ratio q only varies by about 30% for the mass ratio ranges considered here and so is not of interest. The eccentricity term is not of importance for mildly eccentric systems, $f(e_{\text{DCO}} \leq 0.3) \leq 1.4$ but of large importance for the very eccentric $f(e_{\text{DCO}} \geq 0.9) \geq 300$. The fraction of highly eccentric systems with $e_{\text{DCO}} > 0.9$ is 33%, 16%, and 8% of for BHBH, BHNS and NSNS respectively, see also Fig. F3.

We conclude that the shorter median separations at DCO formation are the main reason why NSNS are most strongly peaked at short delay times. They are followed

Component	Formation	Detectable			
	All	All	BHBH	BHNS	NSNS
Low- α disc	42.5%	86%	89%	82%	85%
High- α disc	42.5%	6%	5%	8%	12%
Bulge/bar	15.0%	8%	6%	10%	3%

Table 1. Percentage of systems in each Galactic component.

by BHBHs rather than BHNSs due to the high masses and substantial eccentricities of BHBHs.

Time until merger—Fig. 3f shows the remaining time until merger for each of the DCO types at the start of LISA mission. The distributions are strikingly similar and peak with merger times of around a Myr.

The merger time is a function of the mass, frequency and eccentricity of the sources, such that more massive, higher frequency and more eccentric sources merge faster (Peters 1964, Eq. 5.14). So, despite the fact that each DCO type often has higher values in any one of these properties, the convolution of all three tends to negate the differences. For example, NSNSs have the highest orbital frequencies and are mildly eccentric whilst BHNSs have moderate orbital frequencies and are more circular. However, BHNSs are more massive in general and so the overall merger times are distributed very similarly for both DCO types.

3.3. Distribution in the Milky Way

For our Milky way model we consider three different components, a low-[α/Fe] (“thin”) disc, an older high-[α/Fe] (“thick”) disc and a bulge/bar (see Sec. 2.2). In Table 1 we summarise the number of detections originating from each of these components. Despite the fact that only 42.5% of systems are formed in the low-[α/Fe] disc, we find that 86% of the detections originate from this component. This is because most detectable systems were formed relatively recently (see Fig. 3e) and so the high-[α/Fe] disc and bulge are effectively too old to contribute many detectable systems. Nevertheless, we do find a significant fraction of detectable systems originate in the high-[α/Fe] disc and bulge, indicating that it is still important to include these components, as was ignored in some earlier works (see Sec. 6).

In the top panel of Fig. 4, we show the density distribution for detectable DCOs in the galaxy. We see that most detectable sources are concentrated towards the Galactic centre, with a strong bias towards sources that are on our side of the Milky Way in the vicinity of the solar system (indicated with the \odot symbol). In principle, systems are detectable out to large distances of about 20 kpc and more, although they become increasingly rare, as can be seen from the 95% contour.



Figure 4. **Top:** A face-on view of the Galactic density distribution for detectable DCOs. We show the density distribution for the top 95% of the sources, the rest are indicated by scatter points whose sizes correspond to their sampling weights. The coloured lines show the 75% contour for each of the individual DCO types. The large cross passes through $(0, 0)$ and helps to highlight the bias towards the position of the sun, which is indicated by the \odot . **Bottom:** As Fig. 3, but for the luminosity distance. 

The differences between different DCO types can be seen more clearly in the bottom panel of Fig. 4 where we show the distribution of the distances, D , from earth to the detectable systems. Each distribution peaks around 8 kpc, which is the distance to the centre of the Milky Way. The distribution for BHBH and BHNS systems follow a very similar shape, favouring the detection of systems with distance < 8 kpc, but with a tail extending out to about 20 kpc.

The distribution for NSNS stands out by being flatter, making them more common nearby and, surprisingly, also at larger distances compared to the stellar density. This may seem counter intuitive as one might naively

expect the less massive NSNS systems would not be observable out to larger distances than the more massive BHNS and NSNS systems. To understand the differences we need to consider not only the mass distribution of binaries, but also their eccentricity and frequency distributions. Since, each parameter contributes to the calculation of the SNR (and thus affects the maximum distance at which systems can be detected).

The reason that the NSNSs are favoured at higher distances is that the NSNS population has the highest fraction of “mildly” eccentric systems ($0.01 < e < 0.03$). In contrast, the BHNS population has a much higher fraction of effectively circular systems ($e < 0.01$), which emit weaker gravitational waves compared to equivalent eccentric systems. Therefore, despite their typically higher masses, the distance at which a BHNS source is detectable is generally lower than for the mildly eccentric NSNS.

Conversely, the BHBH population has the highest fraction of highly eccentric systems ($e > 0.3$). Although one may naively expect that this would result in stronger signals (and so further distances), for a system to have these high eccentricities in LISA, it must still be early in its evolution (otherwise it would have circularised) and thus have a low orbital frequency. The result of this is that highest eccentricity systems tend to have lower SNRs and so cannot be detected at large distances.

Overall we see that the eccentricity distribution of NSNSs occupies a “sweet spot” where the gravitational wave power is increased compared to circular systems, but it isn’t too high that the frequency is significantly impacted. This means that NSNSs can be seen out to the largest distances of the three DCO types.

3.4. Formation channels

In our fiducial model, approximately two thirds of detectable BHBHs are formed through the ‘only stable mass transfer’ channel, whilst the remaining third are primarily formed through the ‘classic’ CE channel. Detectable BHNSs follow an inverse pattern, such that around two thirds are formed through the classic channel and the rest are mainly formed through only stable mass transfer.

In contrast, detectable NSNSs are very rarely formed through only stable mass transfer. Approximately half of systems are formed through the ‘classic’ channel and the rest are formed through a double-core common-envelope event (Brown 1995) where both progenitors evolve on a similar timescale and initiate a double-core common-envelope event whilst they are on the giant branch. All detectable DCOs show a small fraction of systems are formed through a channel that does not fit

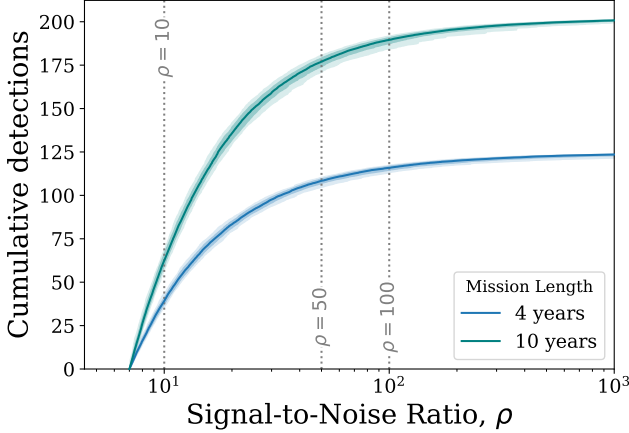


Figure 5. Cumulative number of LISA detections with a given signal-to-noise ratio. Colours indicate LISA mission length and shading shows 1- and 2- σ uncertainties (obtained via bootstrapping). .

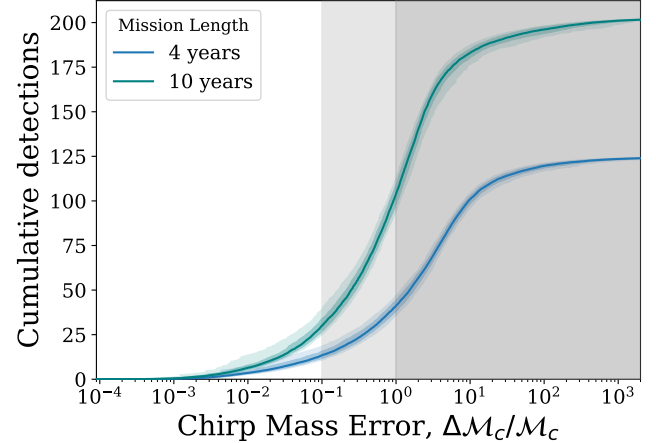


Figure 6. As Fig. 5, but for the chirp mass uncertainty. The shaded areas indicate regions with more than 10% and 100% uncertainty. .

into the other categories and hence are labelled ‘other’. These systems tend to be formed through ‘lucky’ supernova kicks that happen to shrink the binary significantly by chance.

The fraction of detectable DCOs that are formed through different formation channels in the other model variations are shown Fig. F1, where the first column in the plot corresponds to the fiducial model that we described above.

3.5. How accurately will we be able to infer the parameters of detected systems?

So far we have discussed the properties of the all detectable sources. However, only for a subset of systems we expect to get high enough SNR to obtain accurate and useful measurements of these parameters. Below we discuss the expected SNR distribution and the typical uncertainties expected for the most relevant parameters, namely, the chirp mass and sky localisation.

Signal-to-noise ratio—In Fig. 5 we show the cumulative number of detections with a given SNR. Although many a large fraction of sources have SNRs around our assumed detection threshold of 7, many systems are detected with very high SNRs. We find that on average for a 4(10)-year LISA mission, of the 124(202) detections, 85(138), 16(27) and 9(14) systems have SNRs greater than 10, 50 and 100, respectively. These high SNR systems are typically, but not only, the more massive BHBH systems.

Chirp mass—The chirp mass is important for identifying the type of the source of a detected GW signal. The uncertainty of the chirp mass depends on the uncertainty in the measured orbital frequency, the time derivative of

the orbital frequency and the eccentricity as detailed in Appendix C.

We find that for a 4(10)-year LISA mission, approximately 41(105) detections have measurable chirp masses ($\Delta M_c/M_c < 1$, indicated by the dark shaded region in Fig. 6) whilst 13(31) have chirp mass uncertainties below 10% ($\Delta M_c/M_c < 0.1$, indicated by the light shaded region in Fig. 6). This uncertainty is generally dominated by the uncertainty on the time derivative of the frequency, since most of the binaries are too early in their inspiral for LISA to measure a strong chirp. Note from Fig. 6 that increasing the mission length significantly increases the number of detections for which the chirp mass uncertainty is below 100%. The total number of detections only scales as $\sqrt{T_{\text{obs}}}$, yet we find that the the total number of detections with a chirp mass uncertainty is below 100% and 10% both scale approximately as T_{obs} .

Sky localisation—An accurate sky localisation will be essential to possibly identify electromagnetic counterparts or distinguish sources that come from different components of our Milky Way.

We quantify the sky localisation of a source by estimating the angular resolution for the detectable sources. Since all potential sources are effectively stationary on the timescale of the LISA mission, we can follow Mandel et al. (2018) and use the timing accuracy of LISA and the effective detector baseline to calculate the angular resolution, σ_θ , as

$$\sigma_\theta = 16.6^\circ \left(\frac{7}{\rho} \right) \left(\frac{5 \times 10^{-4} \text{ Hz}}{f_{\text{dom}}} \right) \left(\frac{2 \text{ AU}}{L} \right), \quad (15)$$

where L is the effective detector baseline, which for LISA is 2 AU in the frame of the solar system, since it will orbit the Sun.

We plot the distribution of expected angular resolutions in Fig. 7. We see that, for a 4(10)-year LISA mission, approximately 82(123) sources can be resolved to an angular resolution better than 10 degrees and only 16(23) better than 1 degree.

For comparison, the size of a pencil beam for a 15 m diameter SKA dish observing at 1.4 GHz is roughly 0.67 square degrees (Smits et al. 2009), corresponding to an angular resolution of $\sigma_\theta = \sqrt{(0.67/\pi)} = 0.46^\circ$ (similar to the angular size of the moon). We will further discuss the prospects of matching LISA detections to radio pulsars with SKA in Sec. 5.2.

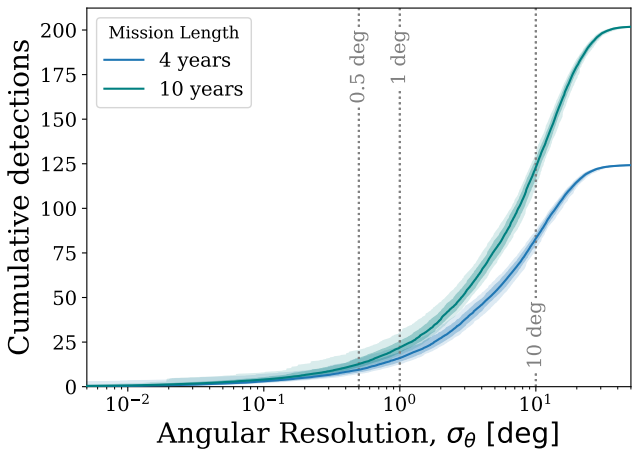


Figure 7. As Fig. 5, but for the angular resolution.

4. RESULTS II - IMPACT OF PHYSICS ASSUMPTIONS

In this section we explore the effect of varying the uncertain assumptions governing the evolution of binary system and the formation of compact objects. For this we use the population synthesis simulations and model variations presented in Broekgaarden et al. (2021a,b).

We first discuss the robustness of our predictions for the number of detectable systems (Section 4.1). We then discuss examples of how the observable properties of the detectable systems, such as the distribution of masses and eccentricities, are affected and can potentially be used to probe the physics of double compact object formation (Section 4.2).

4.1. Detection rates

We predict approximately 30-370 detections in a 4-year LISA mission, across all our simulations for varying physics assumptions. This increases to about 50-550

for a 10-year LISA mission. Although the number of detections per type can vary by about 2 orders of magnitude, we find that the total detection rate is fairly robust, among the variations we have considered (see Table F1).

In Fig. 8, we show the expected number of LISA detections based on our simulations considering variations in the physical assumptions. We show the expected number of detections for BHBH, BHNS and NSNS systems in the top, middle and bottom panel respectively. All the rates and their uncertainties plotted in this figure are also provided in Table F1. In the sections that follow, we briefly explain the variations considered and discuss the most prominent trends.

4.1.1. Efficiency of mass transfer

The efficiency of mass transfer, i.e. the fraction of mass lost by the donor through Roche-lobe overflow that is accreted by the companion, is poorly constrained and is considered as one of the main uncertainties in binary evolution (e.g. de Mink et al. 2007). In our fiducial model A, we use a prescription in which the accretion rate onto stellar companions is regulated by their thermal timescale, i.e. the timescale on which a star can react to changes and restore thermal equilibrium (see e.g. Schneider et al. 2015).

In models B-D, we instead adopt a fixed value for the mass transfer efficiency, β , from $\beta = 0.25$ up to 0.75 , in cases of stable mass transfer onto a stellar companion. For accretion onto NS and BH we still assume that their accretion is limited to the Eddington rate.

Nearly all systems that can be detected form through channels where the very first interaction is stable mass transfer. Generally, higher mass transfer efficiencies lead to higher masses for the accreting stars, but also leads to wider orbits (Soberman et al. 1997; van Son et al. 2020). Changing β thus already affects the masses and orbital separation after the first interaction phase, which in turn changes the starting conditions and outcome of all subsequent interactions phases. This makes it complicated to fully understand the impact of varying β in simple terms, but we can distinguish two main patterns for higher and lower mass systems respectively.

For the most massive progenitors, increasing β leads to secondary stars that are so massive and luminous that they experience strong wind mass loss. This leads to further widening of the orbit. In addition the more massive secondaries may not be able to fully expand as mass loss may prematurely remove their hydrogen envelope. Both of these effects tend to prevent the most massive secondaries from filling their Roche lobe. This means that they cannot initiate the reverse interaction needed

to shrink the binary system and eventually produce a detectable double compact object. We indeed see that increasing β leads to a decrease of the expected number of detections for BHBHs and BHNSs, which originate from the most massive progenitors.

For lower mass progenitors, which primarily produce NSNS systems, we find the opposite: increasing β leads to an *increase* in the number of detectable NSNS systems. This is in part because the changes in secondary mass and the orbital widening, affect the number of systems for which the reverse interaction successfully ejects the envelope and shrinks the orbit. Furthermore, the increased mass of the secondary stars allows stars that would have otherwise ended their life as a WD to instead become massive enough to form a NS (e.g. Zampertas et al. 2017). The same effect also allows some NS progenitors to become massive enough to become BH progenitors, which partially cancels the extra progenitors that would have originally been destined to become WDs.

4.1.2. Common-envelope evolution

The common-envelope phase constitutes a highly uncertain phase in the evolution of interacting binary systems (e.g. Ivanova et al. 2013). The uncertainties concern the conditions required for the onset of a common-envelope phase and, if a common-envelope phase occurs, what the outcome is. Rapid population synthesis simulations such as ours approximate both questions in a crude way. We therefore consider several model variations.

The efficiency parameter α_{CE} —To estimate the outcome of a CE phase, we use a simple consideration of the binding energy and orbital energy (Webbink 1984; de Kool 1990). Our fiducial model assumes a common-envelope efficiency parameter $\alpha_{\text{CE}} = 1$ which can be interpreted as the case where all the energy liberated by shrinking the orbit is used in an optimal way to unbind the envelope. There have been many attempts to constrain this parameter using observations and more recently also using 3D simulations (e.g. De Marco et al. 2011; Law-Smith et al. 2020; Lau et al. 2021), but no consistent picture has emerged. Therefore we consider large variations in this parameter.

In models G-J we alter the common-envelope efficiency parameter α_{CE} to 0.1, 0.5, 2.0 and 10.0 respectively. Values smaller than 1 may represent cases where not all energy is used efficiently to unbind the envelope, for example when part of the energy escapes in the form of radiation or if part is used to impart additional kinetic energy in the ejecta (e.g. Ivanova et al. 2013; Nandez & Ivanova 2016). Values larger than 1 may represent cases

where additional energy sources can be tapped into, such as for example jets powered by accretion (e.g. Schreier et al. 2021). The variations can also be seen as a way to cover uncertainties in estimates for the binding energy itself.

Increasing α_{CE} makes common-envelope ejection more efficient or, in other words, less orbital shrinkage is needed to successfully eject the envelope. This has two consequences. (1) A larger fraction of systems avoids merging during the CE phase. This increases the overall number of DCOs. (2) The systems that survive the CE phase are wider, possibly too wide to become detectable as gravitational wave sources (e.g. Klencki et al. 2021). So, while the first consequence favours the formation of DCOs, the second consequence disfavours the formation of DCOs that are tight enough to be detected.

These two opposing effects result in a fine tuning situation. Only a very small subset of progenitor systems have the right orbital parameters prior to the CE phase to successfully produce detectable systems. Changing α_{CE} moves and changes this window in the parameter space that successfully leads to the formation of detectable systems. How the number of the detectable systems changes depends on whether the relevant parameter space grows or shrinks and on how well the relevant part of the parameters space is populated. Fully unravelling these effects and how they interplay with the assumed star formation history is beyond our scope (and possibly not even of large relevance given the severe simplifications). We will limit the further discussions to simply stating the trends we observe.

We find that the BHBH rate peaks for $\alpha_{\text{CE}} = 1$ (model A) and reduces whether we increase *or* decrease α_{CE} . The BHNS rate follows the same pattern as BHBHs although the value of α_{CE} which maximises BHNSs seems to be between 1 and 2. In contrast, for NSNSs we find that increasing α_{CE} (models I and J) results in significantly higher rates.

The “optimistic” CE treatment—We further explore a model variation introduced by Belczynski et al. (2007) often referred to as the “optimistic” CE scenario. This variation (model K) relaxes our restriction that donor stars that are on the Hertzsprung cannot survive common-envelope events.

In agreement with other studies, we find that this treatment leads to a significant increase in the formation rate of BHBHs, by a factor of two. This is because the progenitors expand significantly during the Hertzsprung gap phase in our simulations. In our fiducial simulation, all progenitors that initiate unstable interaction during this phase would end as stellar mergers, while in this variation they will survive. The progenitors of BHNSs

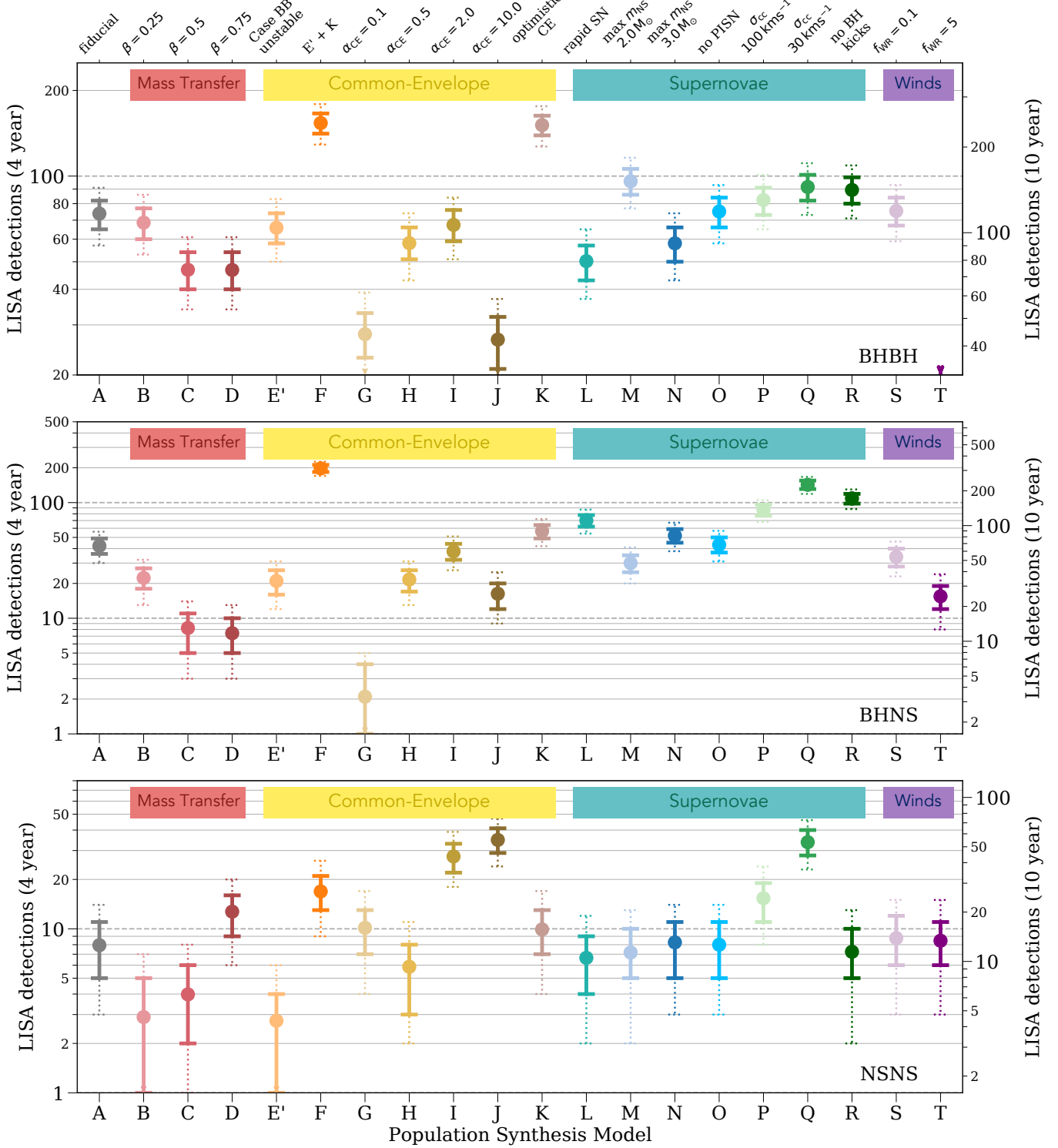


Figure 8. The number of expected detections in the LISA mission for different DCO types and model variations. Error bars show the 1- (solid) and 2- σ (dotted) Poisson uncertainties. An arrow indicates that the error bar extends to zero. The left axis and grid lines show the number of detections in a 4-year LISA mission and the right axis shows an approximation of the number of detections in a 10-year mission (we scale the axis by $\sqrt{T_{\text{obs}}}$, see Table F1 for exact rates). Each model is described in further detail in Table A1 and details of the fiducial assumptions are in Section A.2. See Sec. 4.1 for a discussion.

1135 and NSNSs are less strongly affected with an increase
 1136 about 30% increase.

1137 *Case BB mass transfer*—In models E' and F we consider
 1138 uncertainties in case BB mass transfer. This is a phase
 1139 of mass transfer where the donor star has already lost
 1140 its hydrogen envelope in a prior interaction, but fills
 1141 its Roche lobe again as it expands during helium shell
 1142 burning phase (e.g. Dewi et al. 2002; Tauris et al. 2015,
 1143 2017). This is of particular interest for the formation
 1144 of NSs, as their lower mass progenitors are swelling the
 1145 most during this phase (e.g. Laplace et al. 2020, and
 1146 references therein). Population synthesis studies find
 1147 that nearly all NSNS systems form through a phase of
 1148 case BB mass transfer (Vigna-Gómez et al. 2018).

1149 In model E' we enforce that case BB mass transfer is
 1150 always unstable, such that it always leads to a CE. Note
 1151 that this is slightly different from model E described in
 1152 Broekgaarden et al. (2021a,b). In their work the pes-
 1153 simistic approach to CE evolution is implemented such
 1154 that all HG stars are excluded including helium stars in
 1155 the helium shell burning phase. This, in combination
 1156 with the assumption that case BB mass transfer is al-
 1157 ways unstable, effectively leads to the exclusion of all
 1158 systems that originate through this channel. We are in-
 1159 terested in NSNS systems, which are frequently formed
 1160 through this channel in our simulations. Therefore, we
 1161 adapted this model to only exclude H-rich HG donors,
 1162 but allow systems with donors that are helium stars in
 1163 the helium shell burning phase to survive a CE phase.

1164 As expected, in model E', we find that case BB sys-
 1165 tems form through a common-envelope phase rather
 1166 than only stable mass transfer (see Fig. F1). This model
 1167 gives the lowest NSNS rate of all of our variations, which
 1168 is a factor of 3 lower than our fiducial rate. We also
 1169 find a reduction of the BHNS systems by a factor 2.
 1170 The BHBH systems are not significantly affected, as ex-
 1171 pected, since case BB mass transfer does not play a role
 1172 for high mass progenitors.

1173 Finally, in model F, we again enforce that case BB
 1174 mass transfer is always unstable, but in combination
 1175 with the optimistic treatment for CE (essentially com-
 1176 bining models E' and K). This allows the systems that
 1177 have HG donors for common-envelopes (as well as those
 1178 formed through case BB mass transfer) to survive the
 1179 CE phase. We find that this model leads to the highest
 1180 predictions for the detections among all variations that
 1181 we have considered.

1182 4.1.3. Supernovae and compact remnants

1183 The formation of compact remnants and their associ-
 1184 ated natal kicks also constitute important uncertainties.

1185 In model L we consider the so-called “rapid” remnant
 1186 mass function by Fryer et al. (2015) as an alternative
 1187 to the “delayed” description used in our fiducial simula-
 1188 tions. This affects the mass distribution (see Sec. 4.2.1),
 1189 but the effects on the number of detectable systems is
 1190 modest for BHBH and BHNS, and negligible for NSNS.
 1191 The same is true for the impact of changing the as-
 1192 sumed maximum neutron star mass, $m_{\text{NS},\text{max}}$ (M and
 1193 N). Lowering $m_{\text{NS},\text{max}}$ increases the number of detec-
 1194 tions involving BHs (since more stars form BHs instead
 1195 of NSs) and vice versa, but has no significant effect on
 1196 the number of NSNS detections since the vast majority
 1197 are formed from low mass NSs.

1198 We find that not implementing pair-instability super-
 1199 novae (PISN) or pulsational pair-instability supernovae
 1200 (PPISN) in model O has no effect on the number of de-
 1201 tections with LISA. This is because the average metal-
 1202 licity of the Milky Way is high enough such that no
 1203 progenitor retains enough mass to initiate a PISN or
 1204 PPISN.

1205 Decreasing the natal kicks for all core-collapse super-
 1206 novae (models P-Q) increases the detection rates for
 1207 each DCO type, since lower kicks result in fewer dis-
 1208 rupted binaries and hence a more numerous detectable
 1209 population. The BHNS and NSNS systems are strongly
 1210 affected whilst the impact on BHBH systems is insignif-
 1211 icant. The reason that BHBHs are relatively unaffected
 1212 is that, in our models, the natal kicks for BHs are scaled
 1213 down with the amount of mass that falls back. In the
 1214 case of BHBHs, the black holes have very massive cores
 1215 and thus low kicks.

1216 In model R we assume BHs form without any kick,
 1217 while using our fiducial assumption for the natal kicks of
 1218 neutron stars. This increases the predictions for BHNS
 1219 by a factor 3 but the impact on BHBH systems is much
 1220 smaller for the same reason as for models P-Q. As ex-
 1221 pected, the NSNS population is not affected.

1222 4.1.4. Stellar winds

1223 Mass loss in the form of stellar winds or eruptions is
 1224 also a main uncertainty. It affects by how much stars
 1225 can grow in size and it affects the final core masses. We
 1226 consider variations in the mass loss by naked helium
 1227 (Wolf-Rayet like) stars and choose to vary the efficiency
 1228 of these winds between 0.1 and 5, to account for un-
 1229 certainties in the derived rates (e.g. Vink 2017; Shenar
 1230 et al. 2019; Hamann et al. 2019; Sander & Vink 2020).

1231 We find that a reduction of the wind mass loss has very
 1232 little effect on our predictions. This is the consequence
 1233 of several effects that cancel each other. Firstly, the
 1234 decreased Wolf-Rayet like winds mean that the DCOs
 1235 (particularly those containing BHs) are generally more

massive and so more detectable in LISA. Secondly, one may expect that LISA sources in model S would be higher frequency than in our fiducial model as decreased winds generally result in tighter binaries. However, though this is the case at DCO formation, we find that by the time the sources have evolved until they are observable by the LISA mission, they have lower orbital frequencies than in our fiducial model. This is because the reduced winds allow DCOs to be formed at higher metallicity and, therefore, at more recent times. This means that most DCOs do not evolve for as long before the LISA mission and so remain at lower frequencies (wider separations) thus making them less detectable.

In addition, we find that NSNSs are more eccentric and BHBHs are less eccentric than our fiducial model (with BHNSs relatively unchanged). The increase in eccentricity for NSNSs comes from the same reason as the lower frequency, more recent birth times mean that binaries have less time to circularise. The same is not true for BHBHs as the more massive systems are less affected by supernova kicks and so fewer high eccentricity systems are formed. Overall, despite the large differences in the system properties, these three effects in combination leave the detection rates relatively unchanged.

In model T we instead *increase* the efficiency of Wolf-Rayet winds by a factor of 5. In this model the detection rate of BHBHs decreases by over a factor of 10 and BHNSs by over a factor of 2 whilst the NSNS rate is relatively unchanged. Increasing the efficiency of WR winds widens the orbit and decreases the final masses of DCOs. This means that some progenitors that would have formed LISA sources under our fiducial assumptions would not have enough mass to produce a DCO, or produce a NS instead of a BH. The effect is strongest for the progenitors of black holes, since these are most strongly affected by Wolf-Rayet winds. This effect is less pronounced in NSs since the rate of mass loss for the progenitors of these systems is low enough that changing by a factor of 5 still does not impact the final fate. Moreover, DCOs that are formed tend to be less massive and therefore less detectable.

4.2. Properties of detectable systems

In this section, we consider how varying underlying physics assumptions changes the properties of detectable systems. We focus on several key differences across physics variations rather than showing the differences in every model and thus this section is by no means exhaustive.

4.2.1. Using LISA to investigate the lower mass gap

In Fig. 9, we show the component mass distribution for all LISA detectable DCOs (BHBHs, BHNSs

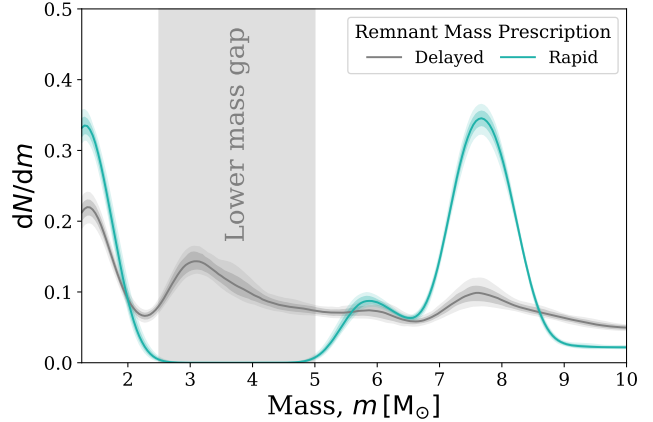


Figure 9. Comparison of the component mass distribution of LISA detectable DCOs when using the Fryer delayed (model A) and rapid (model L) remnant mass prescriptions. Distributions are plotted in the same way as Fig. 3, except all DCO types are shown in one curve and each type is weighted by its detection rate in the respective model.

and NSNSs) for two different remnant mass prescriptions. The grey distribution uses the Fryer *delayed* remnant mass prescription (Fryer et al. 2012), which is our fiducial assumption (model A). This prescription produces compact objects in the lower mass gap ($2.5 M_{\odot} \leq m \leq 5 M_{\odot}$) and indeed we find that, of the LISA detectable DCOs, approximately 69% of BHBHs, 39% of BHNSs and 0% of NSNSs have at least one component in the lower mass gap. Overall, weighting by the relative detection rates, this gives that, in our fiducial model, 55% of our predicted LISA DCO detections would have at least one component in the lower mass gap when using this remnant mass prescription. This equates to approximately 69 systems being detected in the lower mass gap. Alternatively, the blue curve in Fig. 9 shows the same distribution but for the *rapid* remnant mass prescription (Fryer et al. 2012), which we use in model L. In this case, no compact objects are formed (and therefore, detected) in the lower mass gap.

From the stark difference between these models, it is clear that it is difficult at this point to say with any certainty what fraction of systems LISA will detect in the lower mass gap given the highly uncertain formation rate of systems in this mass range. Indeed, we find that the percentage of detectable systems with at least one component in the lower mass gap varies between approximately 30-70% (or, in terms of detections, from 15 to 156) for the different model variations. However, it is important to highlight that *if* DCOs are formed with components in the lower mass gap, LISA *will* be able to detect them. And thus, LISA could be a useful instrument for providing constraints on the existence or

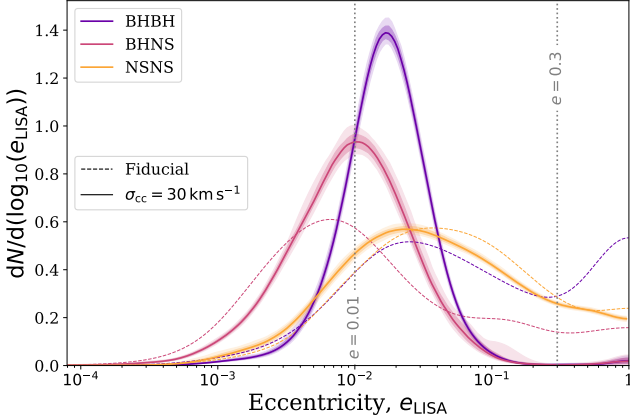


Figure 10. As Fig. 3d, but for model Q. For comparison, we show the mean distribution for the fiducial model (model A) as dashed lines.

non-existence of a lower mass gap based on the mass distribution of detected DCOs.

4.2.2. Effect of natal kicks on eccentricity distribution

In Fig. 10, we investigate how decreasing the magnitude of natal kicks from core-collapse supernovae affects the eccentricity distribution of LISA detectable DCOs. For reference, we show the mean fiducial distributions (model A) as dashed lines (see Fig. 3d for full comparison). In the main curves, we reduce the velocity dispersion for core-collapse supernovae from 265 km s^{-1} to 30 km s^{-1} (model Q).

We find that the LISA detectable BHBHs are significantly less eccentric with weaker kicks, such that the population above $e = 0.2$ is nearly completely eliminated. This is because BHBHs are often massive enough to withstand strong natal kicks without disrupting and these kicks tend to impart significant eccentricity. In model Q, very few systems are ever given such strong kicks and thus very few BHBHs are detected with significant eccentricity.

Since BHNSs are less massive than BHBHs and have more unequal mass ratios, they are more vulnerable to disruption during supernova kicks. BHNSs can only withstand strong kicks when they are aimed in the correct direction and so only a small ‘lucky’ fraction of the fiducial population is highly eccentric. Therefore in model Q, although we see that the population of highly eccentric BHNS systems is eliminated (similar to BHBHs), the peak of the distribution actually shifts to higher eccentricity. This is because a larger fraction of systems are given weaker kicks that BHNSs can withstand and these impart much more moderate eccentricities.

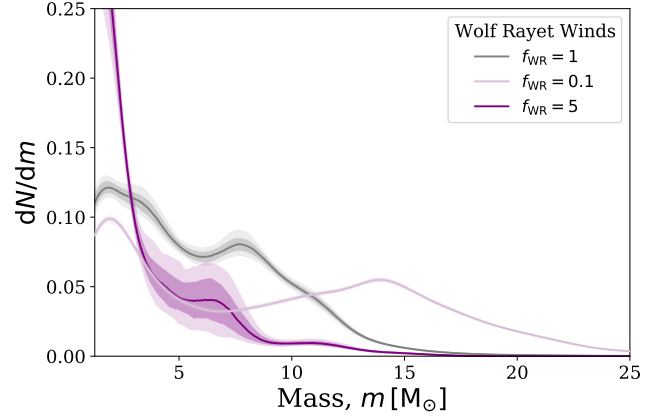


Figure 11. As Fig. 9, but instead varying Wolf-Rayet wind efficiency (models S and T). The curve for $f_{\text{WR}} = 5$ has much higher uncertainties as there are many fewer DCO systems formed in this model (the inverse reasoning also explains the lower uncertainties for $f_{\text{WR}} = 0.1$).

Finally, we find that the NSNS distribution is relatively unchanged between model A and Q. This is not surprising however since the majority of NSNSs are formed through electron-capture supernovae and ultra-stripped supernovae and for these types of supernovae we use $\sigma_{\text{rms}}^{1D} = 30 \text{ km s}^{-1}$ already (see App. A.2) and thus there is little difference between the models.

Overall, compared to our fiducial model, we find that decreasing supernova natal kicks, though it strongly increases the number of detections (see Fig. 8), strongly decreases the fraction of highly eccentric systems that are detected.

4.2.3. Effect of Wolf-Rayet winds on mass distribution

In Fig. 11 we show the effect that changing the efficiency of Wolf-Rayet winds has on the individual component mass distribution. Decreasing the Wolf-Rayet wind efficiency allows the formation of more massive DCOs in the Milky Way and, indeed, we see that the distribution extends to $25 M_{\odot}$ and relatively fewer detectable systems are formed at low masses. By contrast, increasing the Wolf-Rayet efficiency by a factor of 5 strongly disfavours the formation of systems at high masses and approximately 85% of detectable systems have masses below $5 M_{\odot}$. These three distributions are very distinct and so it is possible that the mass distribution of LISA could help to constrain the efficiency of Wolf-Rayet winds.

5. DISCUSSION

In this section we discuss the prospects of (and methods for) identifying LISA sources (Sec. 5.1), the possibility of matching LISA signals to SKA detections (Sec. 5.2), the main caveats for this study (Sec. 5.3) and

the possible contribution from other formation channels (Sec. 5.4). All predictions quoted in each subsection are derived for the fiducial model (model A).

5.1. Identification of GW sources

It is important to note that, though we present predictions for the detection rates of specific DCO types, the nature of the source may not be immediately (*or ever*) apparent from the gravitational wave signal. LISA can detect a variety of sources, from exoplanets (e.g. Tamanini & Danielski 2019) to common-envelopes (e.g. Ginat et al. 2020; Renzo et al. 2021) that may cause confusion. However, by far the most prominent will be the population of Galactic WDWDs detectable with LISA, which will be several orders of magnitude larger than the population of the more massive DCOs that we focus on in this paper (e.g. Korol et al. 2017). It is therefore imperative that we consider how to distinguish NS and BH binaries from this much more numerous population of sources. In addition to distinguishing them from WDWDs, we must consider how to discriminate between BHBHs, BHNSs and NSNSs themselves.

5.1.1. Distinguishing from WDWD population

The simplest way to check whether a source is a WDWD is to evaluate its chirp mass. The mass of a non-rotating white dwarf cannot be larger than the Chandrasekhar limit of $1.4 M_{\odot}$ (Chandrasekhar 1931; Hamada & Salpeter 1961), so we can take the maximum chirp mass of a WDWD to be $\sim 1.2 M_{\odot}$. Therefore, any DCO with a chirp mass that satisfies $M_c > 1.2 M_{\odot} + \Delta M_c$ must not be a WDWD (where ΔM_c is the error on the chirp mass, estimated using Eq. C3). We find that for the detectable population of a 4(10)-year LISA mission, 24(38)% of BHBHs, 28(41)% of BHNSs and 4(5)% of NSNSs satisfy this condition. This method is not particularly effective for NSNSs since their average chirp mass, $1.17 M_{\odot}$, is below the Chandrasekhar limit.

Another discriminator between WDWDs and other DCOs is eccentricity. WDWDs formed in the disc are thought to be formed mainly through isolated binary formation and have little to no eccentricity (e.g. Nelemans et al. 2001, see however Dosopoulou & Kalogera 2016a,b; Gosnell et al. 2019). This is because WDWDs formed through isolated binary evolution all experience a phase of mass transfer or a common envelope, which typically circularises the binary (e.g. Marsh et al. 2004). However, in contrast to the more massive DCOs that we study, WDWDs do not experience strong natal kicks which we find to be the main source of eccentricity. Therefore, if any system is detected with anything other than one detectable harmonic, this suggests

that the system is unlikely to be a WDWD. We find that for a 4(10)-year LISA mission, 55(61)% of BHBHs, 27(29)% of BHNSs and 66(68)% of NSNSs are detected with multiple harmonics (see also Sec. 3.2). Both the absolute percentage and the relative improvement with an extended LISA mission is lower for the BHNSs with respect to other DCOs as we find that these BHNSs are less eccentric on average (see Fig. 3d and discussion in Sec. 3.2).

However, we should also consider that eccentric WD-WDs could be formed through dynamical formation in Milky Way globular clusters (e.g. Willems et al. 2007; Kremer et al. 2018), or with third companions (e.g. Antonini et al. 2017). This means that we cannot assume that eccentric binaries are not WDWDs unless they are detected in the Galactic plane (though even then there is a chance they were formed dynamically). We can use the sky localisation, scale height of the disc and distance to the source to estimate what fraction of eccentric sources can be localised to the Galactic plane. This condition can be written as $\sigma_{\theta} < \arcsin(z_{\text{plane}}/D_L)$ or $D_L < z_{\text{plane}}$, where we set the height of the Galactic plane, $z_{\text{plane}} = 0.95$ kpc, to the scale height of the high- α disc. We apply this condition to find that the fraction of sources that are eccentric and localised within the disc for a 4(10)-year LISA mission are 40(40)% for BHBHs, 23(23)% for BHNSs and 59(59)% for NSNSs. Note that although the fractions are the same for the 10-year mission, the absolute number of detections is still greater.

Overall, combining these methods (chirp mass, eccentricity and sky localisation) we find that for a 4(10)-year mission, LISA will detect at least 37(70) BHBHs, 18(38) BHNSs and 5(8) NSNSs that are distinguishable from the WDWD population. Thus we will be able to confidently distinguish approximately half of all detected sources from WDWDs. This increases to roughly 60% for a 10-year mission. We highlight that, though the overall number of LISA detections in an extended mission only increases by a factor of $\sqrt{T_{\text{obs}}}$, the number of distinguishable detections increases by a greater factor since each of the more numerous sources are better measured. This further underlines the benefits of extending the LISA mission to 10 years.

5.1.2. Discriminating between BHBHs, BHNSs and NSNSs

The problem of discriminating between the BHBH, BHNS and NSNS populations can be more difficult than distinguishing them from WDWDs. For NSNSs, we can follow a similar method to the WDWDs (see Sec. 5.1.1) by applying our knowledge of the maximum mass of a neutron star. Following our fiducial assumption, we can take the maximum mass of a neutron star as $2.5 M_{\odot}$

and thus the maximum chirp mass that a system can attain without one of the components being a black hole is $\mathcal{M}_c = 2.2 M_{\odot}$. For a 4(10)-year LISA mission, the fraction of systems that are above or below this limit (and thus *must* respectively contain or not contain a BH component) by more than $\Delta \mathcal{M}_c$ is 21(33)% for BHBHs, 18(24)% for BHNSs and 47(62)% of NSNSs, which in terms of absolute detections is 16(39) for BHBHs, 7(17) for BHNSs and 4(8) for NSNSs.

For separating the BHBH and BHNS population one could do so probabilistically given the properties that are measured, particularly the orbital frequency and eccentricity, since these distributions are fairly different for the two DCO types (see Fig. 3). This method would pose a challenge, however, as it would likely only indicate which type was more likely rather than discriminate between them with strong evidence.

Another possible solution would be the existence of electromagnetic counterparts to the gravitational wave signal. In Section 5.2 we consider the possibility of detecting a pulsar within a BHNS or NSNS system. This could be used to identify the type of the source.

5.2. Matching LISA detections to pulsars with the SKA

Since the vast majority of the LISA detectable population of DCOs will not merge for many years, the main type of electromagnetic counterpart for this population is pulsars. Therefore, for this section we focus only on BHNSs and NSNSs since no BHBH system will contain a pulsar. The joint detection of a binary pulsar with LISA and the Square Kilometre Array (SKA, Dewdney et al. 2009) would not only help to constrain the parameters of the binary, but also enable investigation of other compact object physics. A pulsar(PSR)+BH can provide stringent tests of theories of gravity, in particular the “No-hair theorem” (Keane et al. 2015). Alternatively, an ultrarelativistic PSR+NS system could be used to measure the neutron star equation of state up to an order of magnitude more accurately than other proposed observational constraints (Kyutoku et al. 2019; Thrane et al. 2020).

We estimate that on average, given the number of detectable pulsars and the SKA sky area, each pulsar in the SKA occupies a region with an angular resolution of $\sigma_\theta < 1.3^\circ$ or 0.7° for SKA-1 and SKA-2 respectively (see Appendix E). Therefore, any DCOs containing NSs localised by LISA with an angular resolution lower than these values can be unambiguously matched to the radio signal in the SKA. By considering Fig. 7, approximately 11 and 6 (for SKA-1 and SKA-2) DCOs will satisfy this constraint.

If there is more than one pulsar in the region given by the LISA sky localisation, one can compare the measured parameters of the system in LISA and the SKA. Both the SKA and LISA will measure the orbital frequency to high precision, as well as the time derivative of the frequency and chirp mass to a lesser precision, of each of these systems. Therefore, one could perform a targeted search with the SKA that checks the sky location given by LISA, only looking for binary pulsars with orbital frequencies within the uncertainties. If there was still more than one possible pulsar one could also check against the chirp mass. In this way, we expect it will be possible to get a joint detection between the SKA and LISA even when the sky area implied by the LISA detection contains more than one pulsar.

In order to assess the efficacy of this method, we would need to know the probability that two random binary pulsars would have orbital frequencies and chirp masses close enough that one could not tell which pulsar matches the LISA detection. This would require simulating the SKA population of pulsars with a code such as PSRPOPPY (Bates et al. 2014) to find the frequency and chirp mass distribution, which is beyond the scope of this paper. However, the uncertainty in the orbital frequency of a binary on the detection threshold ($\text{SNR} = 7$) for a 4-year LISA mission is $2.5 \times 10^{-9} \text{ Hz}$ and $1.0 \times 10^{-9} \text{ Hz}$ for a 10-year mission (calculated using Eq. C4). Therefore, we expect that the SKA could likely isolate the correct binary pulsar to match to a LISA detection even when several are present in the sky localisation region.

5.3. Caveats

Our predictions are subject to various uncertainties which can be broadly divided into two different categories: those arising from the progenitor models for the population of DCOs and those arising from the choices we have made when placing these DCOs in our model for the Milky-Way. Although we are unable, at present, to evaluate the impact of all these uncertainties, the reader should nevertheless keep in mind that they are likely very substantial. Most of these concerns are not unique to these study, but apply to most of the predictions available in present literature. We highlight a few main concerns.

Progenitor models—Our binary-star progenitors models have been computed with a rapid population synthesis code (see Sec. 2.1). This code relies on approximate parametric prescriptions for the stellar evolutionary tracks of single stars and simple algorithms to mimic the effects of evolutionary and binary interaction processes. Even though we explicitly consider the

1587 impact of some of the main physics uncertainties (see
 1588 Sect. A.3) the list of variations that we considered is far
 1589 from exhaustive. Moreover, it is by no means guaranteed
 1590 that the parametric prescriptions used in this code lead
 1591 to realistic results, even when varying the values of the
 1592 parameters to their extremes. We stress in particular
 1593 the uncertainties affecting our most massive progenitor
 1594 models. Observational constraints are scarce for high
 1595 mass stars and practically non-existent for the rapid evo-
 1596 lutionary phases (e.g. Langer 2012; Mapelli 2021). This
 1597 is even more true for the evolution of massive stars at
 1598 low metallicity. In addition to our limited understand-
 1599 ing of massive stars, we note that the rapid population
 1600 synthesis code, such as the one employed to compute
 1601 the models used in this study, rely on extrapolations of
 1602 the original fitting formulae to approximate the evolu-
 1603 tionary tracks for these higher mass progenitors (Hurley
 1604 et al. 2000, 2002).

1605 *Populating the Milky Way*—Our Milky Way model is
 1606 semi-empirical and has been calibrated based on ob-
 1607 servations. Unfortunately, the early evolution of the
 1608 (metallicity dependence of the) star formation history is
 1609 poorly constrained. We do not expect this to be a major
 1610 concern, as most of the double compact objects have rel-
 1611 atively short delay times of less than 2 Gyr (see Fig. 3e),
 1612 but this is a caveat that should be kept in mind. Fur-
 1613 thermore, to estimate the rate of detectable systems, we
 1614 rely on normalisation choices (e.g. how many detectable
 1615 double compacts are formed per unit of star formation).
 1616 This depends heavily on the initial mass function, as
 1617 low mass stars account for most of the mass while high
 1618 mass stars are the progenitors of double compact ob-
 1619 jects. Further choices, such as the binary fraction and
 1620 the initial distributions of binary parameters also play
 1621 a lesser but probably still significant role de Mink &
 1622 Belczynski (e.g. 2015); Chruslinska et al. (e.g. 2017);
 1623 Klencki et al. (e.g. 2018).

1624 We also note that, for reasons of computational effi-
 1625 ciency, we have not accounted for the spatial velocities
 1626 resulting from the Blaauw-Boersma kick (Blaauw 1961;
 1627 Boersma 1961). In test simulations we find that account-
 1628 ing for this spreads out the population (increasing the
 1629 typical height above the Galactic plane and Galactocen-
 1630 tric radius), but we find that the impact on the rate is
 1631 limited. In light of the other much larger uncertainties,
 1632 we felt that this was justified (see however, e.g., Brandt
 1633 & Podsiadlowski 1995; Abbott et al. 2017b). **We have**
 1634 **further ignored a possible contribution coming from the**
 1635 **Galactic halo, as Sesana et al. (2020) estimates this is**
 1636 **not significant compared to the contributions from the**
 1637 **Galactic bulge and discs.** However, this may not be true

1638 for other formation channels other than those we have
 1639 considered here.

1640 5.4. Other formation channels

1641 In this paper we considered the formation of NS
 1642 and BH binaries formed via isolated binary evolution,
 1643 through the classical CE channel, the stable mass trans-
 1644 fer channel and variations on these (see Fig. F1). We did
 1645 not consider further possible contributions from other
 1646 formation channels, which may play a role.

1647 We highlight the possible role of dynamical formation
 1648 in globular clusters. Kremer et al. (2018) predict, for a
 1649 nominal 4-year LISA mission, that 21 sources will have
 1650 $\text{SNR} > 7$, of which 7 are BHBHs, 0 are BHNSs and 1
 1651 is a NSNS (see Table 1 Kremer et al. 2018). This is
 1652 significantly lower than the rates we predict for nearly
 1653 every model variation. If true, this would mean that for-
 1654 mation through isolated binary formation will dominate
 1655 the LISA detections.

1656 Banerjee (2020) investigates formation of LISA de-
 1657 tectable BHBHs in young massive and open stellar clus-
 1658 ters and estimates approximately 128 BHBHs with SNR
 1659 > 5 in a 5-year LISA mission (see Table 1, Column 9
 1660 Banerjee 2020). Although this is similar to the number
 1661 we predict for our fiducial model, we note these authors
 1662 adopt a threshold SNR required for a detection that is
 1663 lower and a mission length is slightly longer than what
 1664 is typically assumed (i.e. $\text{SNR} > 7$ and 4 years, as we
 1665 have also adopted in our work). We expect that, after
 1666 correcting for this and making a fair comparison, our
 1667 fiducial model predicts about twice as many detections.

1668 The contribution of triples systems (e.g. Antonini
 1669 et al. 2017), or even higher order multiple systems (e.g.
 1670 Vynatheya & Hamers 2021) will likely also be of inter-
 1671 est, in particular for the formation of eccentric sources.
 1672 We are, however, not aware of specific predictions for
 1673 the detection rates that we can compare to directly.

1674 6. COMPARISON WITH PREVIOUS STUDIES

1675 In Fig. 12, we compare our results to similar previous
 1676 studies that investigate the population of stellar-mass
 1677 BHBHs, BHNSs and NSNSs that are detectable with
 1678 LISA. Fig. 12 details the expected detection rates pre-
 1679 dicted by each paper as well as their assumptions regard-
 1680 ing their Milky Way galaxy model, binary popula-
 1681 tion synthesis simulation and LISA mission specifications.
 1682 We only include papers that are similar to our work,
 1683 such that they use population synthesis and simulate
 1684 sources in the Galactic plane. Moreover, Fig. 12 does
 1685 not include the numerous papers on the LISA WDWD
 1686 population as we do not make predictions for WDWDs.

		Predicted DCO Detection Rates						Population Synthesis						
First Author	Year	BHBH			BHNS		NSNS		Code	Open Source Code	Metallicity	Binary Physics Variations		
<i>Wagg</i>	2021	6-154			9-238		2-198		COMPAS	✓	53 bins between [1e-4, 3e-2]		20	
<i>Shao</i>	2021	12			2		X		BSE	✓	0.02		Fryer rapid, Mandel & Mueller remnant mass	
<i>Breivik</i>	2020	93			33		8		COSMIC	✓	0.02, 0.003		None	
<i>Lau</i>	2020	X			X		35		COMPAS	✓	0.0142		Case BB always unstable, Single SN, alpha=0.1	
<i>Sesana</i>	2020	4.2		6.5		X		X		BSE	✓	13 bins between [1e-4, 3e-2]		None
<i>Lamberts</i>	2018	25			X		X		BSE	✓	13 bins between [1e-4, 3e-2]		None	
<i>Liu</i>	2014	6			3		16		BSE	✓	0.02		None	
<i>Belczynski</i>	2010	2.3	0	0.2	0	4	1.7	Startrack	X	0.02 (disc, bulge), 0.001 (halo)		Optimistic CE, Pessimistic CE		
<i>Nelemans</i>	2001	0			3		39		SeBa	✓	0.02		None	

		Galaxy and Positioning							Detection			
First Author	Year	Star formation history			Spatial distribution			Galactic Components	Metallicity Dependent Distributions	SNR Limit	LISA Mission Time (yr)	Eccentricity Treatment
<i>Wagg</i>	2021	Exponential 8-0 Gyr ago (thin disc), Exponential 12-8 Gyr ago (thick disc), Skewed gaussian 0-6 Gyr (bulge)			Exponential radial and vertical, different scale length/height for each component, thin disc has inside-out growth			Thin disc, thick disc, bulge	✓	7	4, 10	Full
<i>Shao</i>	2021	Constant over 10 Gyr			Uniform flat disc of 15 kpc			Single disc	X	5	4	Full
<i>Breivik</i>	2020	Constant over 10 Gyr (thin disc), 1 Gyr burst 10 Gyr ago (bulge), 1 Gyr burst 11 Gyr (thick disc)			McMillan 2011			Thin disc, thick disc, bulge	X	7	4	Full
<i>Lau</i>	2020	Constant			Miyamoto & Nagai potential (disc), Wilkinson & Evans potential (halo)			Single disc or halo	X	8	4	Full
<i>Sesana</i>	2020	FIRE simulation			FIRE simulation			Everything within 300kpc	✓	7	4, 10	Ignored during detection
<i>Lamberts</i>	2018	FIRE simulation			FIRE simulation			Everything within 300kpc	✓	5	4	Ignored during detection
<i>Liu</i>	2014	Constant over 13.7 Gyr			Exponential radial, sech^2 vertical (Benacquista+2007)			Single disc	X	7	2	Assumed circular
<i>Belczynski</i>	2010	Constant over 10 Gyr (disc), 1 Gyr burst 10 Gyr ago (bulge), burst at 13 Gyr (halo)			Exponential sphere (bulge), exponential radial and vertical (disc), spherical shell (halo)			Disc, bulge, halo	X	10	1	Full
<i>Nelemans</i>	2001	Exponential over 10 Gyr			Exponential radial, sech^2 vertical			Single disc	X	1, 5	1	Full

Figure 12. A table comparing previous studies of a similar nature to this work. In the detection rate section darker shades of blue indicate higher detection rates. In other sections, darker shades of green indicate more detailed models or more accurate choices. Entries in detection rates with two values listed correspond to the different mission lengths (penultimate column). The works listed in the table are Nelemans et al. (2001), Belczynski et al. (2010), Liu & Zhang (2014), Lamberts et al. (2018), Sesana et al. (2020), Lau et al. (2020), Breivik et al. (2020) and Shao & Li (2021).   

1687 *Nelemans et al. (2001)*—were the first to investigate the
 1688 population of LISA detectable stellar-mass double com-
 1689 pact objects. We find a significantly higher detection
 1690 rate for BHBHs and BHNSs, as well as a slightly lower
 1691 rate for NSNSs. We can understand this difference from
 1692 changes both to the specifications of LISA (such as the
 1693 mission length and SNR threshold for detection) and our
 1694 understanding of massive star evolution since the pub-
 1695 lication of their paper, which both strongly affect the
 1696 expected detections rates.

1697 *Belczynski et al. (2010)*—built upon the work of *Nele-*
 1698 *mans et al. (2001)*, by using a different population syn-
 1699 thesis code with two model variations and a multi-
 1700 component model for the Milky Way. They find a much
 1701 lower detection rate for BHNSs and NSNSs (and agreed
 1702 on zero BHBHs) when compared to *Nelemans et al.*
 1703 *(2001)*. They state that this discrepancy from *Nelemans*
 1704 *et al. (2001)* comes from differences in their population
 1705 synthesis and an overall lower formation rate rather than
 1706 any changes to LISA detectability. The low total de-
 1707 tection rate for all DCOs in this paper compared to
 1708 our work is unsurprising given the relatively high SNR
 1709 threshold of 10 and short mission length of 1 year. The
 1710 reduced mission length means that the source signal has
 1711 much less time to accumulate, whilst also fewer WD-
 1712 WDs can be resolved in this time, leading to a weaker
 1713 signal and an increased Galactic confusion noise relative
 1714 to our work.

1715 *Liu & Zhang (2014)*—performed a similar investigation
 1716 using a different population synthesis code and find
 1717 higher rates than earlier works. Their lower detection
 1718 threshold and longer mission length compared to *Bel-*
1719 czynski et al. (2010) likely explains the relatively in-
 1720 creased rates. Yet their rates are still significantly below
 1721 what we find. This could be for several reasons; they as-
 1722 sume all binaries are circular both in their evolution and
 1723 for detection. This means that systems may not have
 1724 inspiralled as far before the LISA mission or may appear
 1725 to have weaker gravitational waves when eccentricity is
 1726 not accounted for. They also use a simplified model
 1727 for the Milky Way with a single disc of one metallicity
 1728 and constant star formation, whilst also using a mission
 1729 length half what we assume. Each of these factors likely
 1730 contributes to the lower overall detection rates.

1731 *Lamberts et al. (2018)*—presented a new approach to the
 1732 problem by using the FIRE simulation (*Hopkins et al.*
 1733 *2014*) to distribute their sources rather than an analyt-
 1734 ical model of the Milky Way and were the first paper
 1735 in this area to incorporate metallicity dependence into
 1736 their Milky Way model. *Sesana et al. (2020)* followed
 1737 up on this paper using the same simulated BHBH pop-

1738 ulation and presented updated results for the number
 1739 of expected BHBH detections. They find significantly
 1740 fewer BHBHs than our fiducial model despite using the
 1741 same SNR threshold and LISA mission length. The dis-
 1742 crepancy between the results of *Sesana et al. (2020)* and
 1743 those presented in this work could be caused by different
 1744 treatments of eccentricity. Unlike our work, *Sesana et al.*
 1745 *(2020)* assume that all binaries are circular for the pur-
 1746 pose of detection in LISA, which could result in a lower
 1747 number of detections by missing eccentric binaries that
 1748 appear as weaker signals when assumed to be circular.
 1749 This is especially relevant as we find that around 87%
 1750 of LISA detectable BHBHs are not circular and around
 1751 21% have significant eccentricity (see Fig. 3d). We also
 1752 improve upon this work by using a larger number of
 1753 metallicity bins compared to *Sesana et al. (2020)*, since
 1754 a low number of metallicity bins can produce artificial
 1755 features in the mass distribution of DCOs and possibly
 1756 affect the detection rate (see *Dominik et al. 2015; Neijs-*
1757 sel et al. 2019; Kummer 2020, and also appendix D for
 1758 further discussion). Finally, it could be that different
 1759 implicit assumptions in their population synthesis code
 1760 lead to differences in our results (*Toonen et al. 2014*).

1761 *Lau et al. (2020)*—focussed on the number of Galactic
 1762 NSNS binaries that could be detected by LISA. Their
 1763 study uses the same population synthesis code, COM-
 1764 PAS, as this work, though an earlier version. Despite
 1765 this, their study finds a much larger number of detec-
 1766 tions. They make several different physical assump-
 1767 tions in their population synthesis, using the *Fryer et al.*
 1768 *(2012)* rapid remnant mass prescription, assuming the
 1769 optimistic CE scenario, limiting the maximum neutron
 1770 star mass to $2 M_{\odot}$ and not implementing PISN. How-
 1771 ever, we note that none of these assumptions strongly
 1772 affect the NSNS LISA detection rate (see bottom panel
 1773 of Fig. 8, models K, L, M and O) and so this is unlikely to
 1774 entirely account for the differences. It is also important
 1775 to highlight that COMPAS has received several improve-
 1776 ments and bug fixes since *Vigna-Gómez et al. (2018)*
 1777 (which contains the simulations used by *Lau et al. 2020*)
 1778 and these could possibly have affected the formation rate
 1779 of NSNSs. Yet it is most likely that the remaining dif-
 1780 ference between our results is due to way in which we
 1781 simulate the Milky Way. *Lau et al. (2020)* use a model
 1782 for the Milky Way similar to that of *Breivik et al. (2020)*,
 1783 which we use to estimate the impact of the choice of MW
 1784 model in Appendix D. The Milky Way model by *Breivik*
 1785 *et al. (2020)* applies only two metallicity bins, while we
 1786 consider a range of metallicities between 10^{-4} and 0.03.
 1787 When applying the simpler model for the Milky Way,
 1788 we find that the NSNS detection rate is increased by at
 1789 least a factor of two. *Lau et al. (2020)* only uses a sin-

gle metallicity, and so assuming that all star formation happens at a single high metallicity (which has a high efficiency of producing NSNS), could lead to an even greater overestimate of the detection rate. Hence, we expect the low number of metallicity bins in their Milky Way model to be the main driver behind the discrepancy between our results.

Breivik et al. (2020)—introduced the population synthesis code COSMIC and presented detections for many different DCO types in LISA using this code. They find that LISA will detect 93 BHBHs, 33 BHNSs and 8 NSNSs in the Milky Way over a 4 year mission. *Breivik et al. (2020)* make many physical assumptions that differ from our fiducial model, the most notable being that they assume the optimistic CE scenario and that case BB mass transfer is always unstable, whilst also using a simpler model for the Milky Way (see Appendix D). Thus for better comparison we ran our simulation using model F and the Milky Way model from *Breivik et al. (2020)*. This results in 97, 101 and 43 detections for BHBHs, BHNSs and NSNSs respectively. Therefore, though we are in very good agreement for BHBHs, we predict much higher rates for BHNSs and NSNSs. These differences are likely due to using a different population synthesis code (COSMIC), which has different underlying physics assumptions from COMPAS. Given our strong agreement for BHBHs, it is possible that COSMIC and COMPAS handle NSs differently and so lead to different detection rates for DCOs containing NSs. However checking this would require a more in-depth study of the intrinsic formation rate of DCOs containing NSs in the two codes.

Shao & Li (2021)—most recently investigated the detectability binaries containing BHs in LISA using BSE and a relatively simple model for the Milky Way (assuming a uniform flat disc, constant star formation and a single metallicity). They assume that kicks for NSs formed through ECSN are slightly higher than our work (50 km s^{-1} instead of 30 km s^{-1}). This may account for their particularly low BHNS rate (as the binaries would be more likely to disrupt), which is a factor of 20 lower than ours, but we expect their assumption of the optimistic CE scenario, reduced Wolf-Rayet winds and lower SNR detection threshold could partially offset this. As we show in Appendix D, their use of a simpler Milky Way model, especially with only a single metallicity, would lead to an underestimate of the BHBH and BHNS rates, which may explain the discrepancy in our results.

Overall, since the work of *Nelemans et al. (2001)*, in addition to the LISA mission specifications, the methods that we use to simulate binaries and the Milky Way have all changed significantly. We now predict that LISA detections of these massive DCOs are dominated by BHBHs, rather than NSNSs, whilst the absolute detection rates for BHBHs and BHNSs are much higher. Further studies in this area could improve on this work by including the effects of systemic kicks on the position of systems in the Milky Way and accounting for contributions from other formation channels.

7. CONCLUSION & SUMMARY

We provide predictions for the detection rate and population properties of LISA detectable BHBH, BHNS and NSNS. We use a novel empirically-informed analytical model for the metallicity dependent star formation history of the Milky Way, calibrated against the APOGEE stellar spectroscopic survey. We use this to model Monte-Carlo realisations of the present-day BHBH, BHNS and NSNS populations in our Milky Way. For the binary population, we use the results of a large grid of simulations performed with the rapid population synthesis code COMPAS (*Broekgaarden et al. 2021a,b*). These simulations have been optimised with the adaptive sampling algorithm STROOPWAFEL to preferentially sample NS and BH binaries. In total these comprise over two billion massive binaries that span 20 physics variations, which represent the most common uncertainties in binary physics. To determine the detectability of sources with LISA we use the LEGWORK package (*Wagg et al. 2021*), that was specifically developed for this purpose and is publicly available. We investigate the results expected for a 4- and 10-year LISA mission. Our main conclusions can be summarised as:

1. Total detections: We predict 30-370 detections in a 4-year LISA mission, across all our simulations for varying physics assumptions. This increases to about 50-550 for a 10-year LISA mission. Although the number of detections per type can vary by about 2 orders of magnitude, we find that the total detection rate is fairly robust, among the variations we have considered (see Table F1).

2. Detections by type: For our fiducial model, we predict a total of 124 ± 11 detections and out of these we find about 74 ± 9 BHBHs, 42 ± 6 BHNSs and 8 ± 3 NSNSs. The errors quoted here are the $1-\sigma$ Poisson uncertainties resulting from the random initialisation of the Milky Way (see Table F1).

3. Physics variations: Among the model variations we consider, we find that our predictions for the

rates for the different DCO types are robust within a factor of 2 of the fiducial rate, with the following exceptions. For BHBHs, the rate is most sensitive to the treatment of common envelope phases or an increase of the WR wind mass loss. For BHNSs and NSNSs, the assumptions regarding the assumed common envelope ejection efficiency, treatment of case BB mass transfer and the kicks are most important. In addition, the assumed mass transfer efficiency impacts the BHNS (see Fig. 8).

4. Probing the black hole mass distribution and the lower mass gap: We expect LISA to predominantly detect lower mass BHs (with 90% of BHBH and BHNSs having BH masses lower than $11 M_{\odot}$ in our fiducial simulations) in stark contrast to current ground-based detectors which are heavily biased towards high mass systems. For our fiducial simulation, we predict that approximately 69 systems with a component with a mass between $2.5\text{--}5 M_{\odot}$ would be detected by a 4-year LISA. This implies that LISA can potentially make important contributions to the debate about the existence of a lower mass gap (see Fig. 9).

5. Eccentricity distribution: We find that for all DCO types a large fraction of detectable systems still have nonzero eccentricities ($e > 0.01$) when entering the LISA band, which can be used to distinguish them from the more numerous WDWD binaries, which are largely expected to be circular. In particular, for our fiducial model, we find that this is the case for around three quarters of detectable binaries. Furthermore, around 16% of detectable binaries have eccentricities that are so high ($e > 0.3$) that the emission at frequencies corresponding to higher order harmonics start to dominate (see Fig. 3).

6. Distinguishing from WDWD sources: For about half of all detections we expect that we will be able to confidently determine the type of compact objects involved and this increases to 60% for a 10-year LISA mission (see Sec. 5.1.1).

7. Chirp mass determinations: For about 10% of systems we expect to be able to determine the chirp mass better than 10% and this increases to 15% for a 10-year LISA mission (see Fig. 6).

8. Prospects for finding EM counterparts: We expect about 13% of detections with a sky localisation better than 1 degree for our fiducial model (though the fraction remains roughly constant

among model variations). This fraction remains the same for a 10-year LISA mission, meaning that the number increases proportionally. This will be of interest for electromagnetic searches for counterparts, in particular for radio pulsar searches with SKA (see Fig. 5.2).

9. Benefits of extending the LISA mission:

The number of detections scale approximately as $\sqrt{T_{\text{obs}}}$, where T_{obs} is the mission length. Therefore, extending the LISA mission from 4- to 10-years increases the number of detections by about 60% for each model variation. A further important benefit is the improvement of the characterisation of the sources, since the relative error on the frequency derivative (which dominates the relative error in the chirp mass) scales as $T_{\text{obs}}^{-2.5}$ for stationary sources (Eq. C5). We find that the number of systems with chirp masses that can be measured better than 10% increases by a factor of 2.4 for each model variation. In addition, the number of systems with a sky localisation better than one degree increases by a factor of 1.5. Overall, the number of sources that can be unambiguously distinguished from WDWDs increases by almost a factor of 2 (see Section 5.1.1).

ACKNOWLEDGMENTS

We thank Katie Brevik, Will Farr, Rob Farmer, Valeriya Korol, Floris Kummer, Eva Laplace, Mike Lau, Tyson Littenberg, Ilya Mandel, Mathieu Renzo, Alberto Sesana, Katie Sharpe, Simon Stevenson, the CCA GW group and COMPAS collaboration for insightful discussions. TW also thanks Terence Lovatt for his advice and help on improving an earlier draft of this project. Portions of this study were inspired by the LISA Sprint at the Center for Computational Astrophysics of the Flatiron Institute, supported by the Simons Foundation. This project was funded in part by the National Science Foundation under Grant No. (NSF grant number 2009131), the European Union’s Horizon 2020 research and innovation program from the European Research Council (ERC, Grant agreement No. 715063), and by the Netherlands Organization for Scientific Research (NWO) as part of the Vidi research program Bin-Waves with project number 639.042.728. We further acknowledge the Black Hole Initiative funded by a generous contribution of the John Templeton Foundation and the Gordon and Betty Moore Foundation.

Software: We used LEGWORK to evolve sources over time and calculate signal-to-noise ratios (Wagg et al. 2021). It is freely available at <https://legwork.readthedocs.io/en/latest/>. Simulations in this paper made use of the COMPAS rapid binary population synthesis code (Team COMPAS: J. Riley et al. 2021). The simulations performed in this work were simulated with a COMPAS version that predates the publicly available code. Our version is most similar to v02.13.01 of the publicly available COMPAS code. Requests for the original code can be made to Floor Broekgaarden. The authors used STROOPWAFEL from (Broekgaarden et al. 2019), publicly available at <https://github.com/FloorBroekgaarden/STROOPWAFEL>⁷.

The authors also made use of Python (v3.8), available at <http://www.python.org>. In addition the following Python packages were used: `matplotlib` (Hunter 2007), `NumPy` (Harris et al. 2020), `Astropy` (Astropy Collaboration et al. 2013, 2018), `Seaborn` (Waskom 2021), `SciPy` (Virtanen et al. 2020), `h5py` (Collette et al. 2021) and `Jupyter Lab` (Kluyver et al. 2016). This research has made use of NASA’s Astrophysics Data System Bibliographic Services. We also made use of the computational facilities from the Harvard FAS Research Computing cluster.

REFERENCES

- Abadie, J., Abbott, B. P., Abbott, R., et al. 2010, Classical and Quantum Gravity, 27, 173001, doi: [10.1088/0264-9381/27/17/173001](https://doi.org/10.1088/0264-9381/27/17/173001)
- Abbott, B. P., Abbott, R., Abbott, T. D., et al. 2016, Physical Review X, 6, 041015, doi: [10.1103/PhysRevX.6.041015](https://doi.org/10.1103/PhysRevX.6.041015)
- . 2019, Physical Review X, 9, 031040, doi: [10.1103/PhysRevX.9.031040](https://doi.org/10.1103/PhysRevX.9.031040)
- . 2020a, ApJL, 892, L3, doi: [10.3847/2041-8213/ab75f5](https://doi.org/10.3847/2041-8213/ab75f5)
- . 2017a, PhRvL, 119, 161101, doi: [10.1103/PhysRevLett.119.161101](https://doi.org/10.1103/PhysRevLett.119.161101)
- . 2017b, ApJL, 850, L40, doi: [10.3847/2041-8213/aa93fc](https://doi.org/10.3847/2041-8213/aa93fc)
- Abbott, R., Abbott, T. D., Abraham, S., et al. 2020b, arXiv e-prints, arXiv:2010.14527, <https://arxiv.org/abs/2010.14527>
- . 2020c, ApJL, 896, L44, doi: [10.3847/2041-8213/ab960f](https://doi.org/10.3847/2041-8213/ab960f)
- . 2021, ApJL, 913, L7, doi: [10.3847/2041-8213/abe949](https://doi.org/10.3847/2041-8213/abe949)
- Abdul-Masih, M., Banyard, G., Bodensteiner, J., et al. 2020, Nature, 580, E11, doi: [10.1038/s41586-020-2216-x](https://doi.org/10.1038/s41586-020-2216-x)
- Abt, H. A. 1983, ARA&A, 21, 343, doi: [10.1146/annurev.aa.21.090183.002015](https://doi.org/10.1146/annurev.aa.21.090183.002015)
- Amaro-Seoane, P., Audley, H., Babak, S., et al. 2017, arXiv e-prints, arXiv:1702.00786, <https://arxiv.org/abs/1702.00786>
- Antoniadis, J., Tauris, T. M., Ozel, F., et al. 2016, arXiv e-prints, arXiv:1605.01665, <https://arxiv.org/abs/1605.01665>
- Antonini, F., & Rasio, F. A. 2016, ApJ, 831, 187, doi: [10.3847/0004-637X/831/2/187](https://doi.org/10.3847/0004-637X/831/2/187)
- Antonini, F., Toonen, S., & Hamers, A. S. 2017, ApJ, 841, 77, doi: [10.3847/1538-4357/aa6f5e](https://doi.org/10.3847/1538-4357/aa6f5e)
- den et al. 2019), publicly available at <https://github.com/FloorBroekgaarden/STROOPWAFEL>⁷. The authors also made use of Python (v3.8), available at <http://www.python.org>. In addition the following Python packages were used: `matplotlib` (Hunter 2007), `NumPy` (Harris et al. 2020), `Astropy` (Astropy Collaboration et al. 2013, 2018), `Seaborn` (Waskom 2021), `SciPy` (Virtanen et al. 2020), `h5py` (Collette et al. 2021) and `Jupyter Lab` (Kluyver et al. 2016). This research has made use of NASA’s Astrophysics Data System Bibliographic Services. We also made use of the computational facilities from the Harvard FAS Research Computing cluster.
- Astropy Collaboration, Price-Whelan, A. M., Sipőcz, B. M., et al. 2018, AJ, 156, 123, doi: [10.3847/1538-3881/aabc4f](https://doi.org/10.3847/1538-3881/aabc4f)
- Astropy Collaboration, Robitaille, T. P., Tollerud, E. J., et al. 2013, A&A, 558, A33, doi: [10.1051/0004-6361/201322068](https://doi.org/10.1051/0004-6361/201322068)
- Banerjee, S. 2020, PhRvD, 102, 103002, doi: [10.1103/PhysRevD.102.103002](https://doi.org/10.1103/PhysRevD.102.103002)
- Barack, L., & Cutler, C. 2004, PhRvD, 69, 082005, doi: [10.1103/PhysRevD.69.082005](https://doi.org/10.1103/PhysRevD.69.082005)
- Bates, S. D., Lorimer, D. R., Rane, A., & Swiggum, J. 2014, MNRAS, 439, 2893, doi: [10.1093/mnras/stu157](https://doi.org/10.1093/mnras/stu157)
- Begelman, M. C., Blandford, R. D., & Rees, M. J. 1980, Nature, 287, 307, doi: [10.1038/287307a0](https://doi.org/10.1038/287307a0)
- Belczynski, K., Benacquista, M., & Bulik, T. 2010, ApJ, 725, 816, doi: [10.1088/0004-637X/725/1/816](https://doi.org/10.1088/0004-637X/725/1/816)
- Belczynski, K., Holz, D. E., Bulik, T., & O’Shaughnessy, R. 2016, Nature, 534, 512, doi: [10.1038/nature18322](https://doi.org/10.1038/nature18322)
- Belczynski, K., Kalogera, V., Rasio, F. A., et al. 2008, ApJS, 174, 223, doi: [10.1086/521026](https://doi.org/10.1086/521026)
- Belczynski, K., Taam, R. E., Kalogera, V., Rasio, F. A., & Bulik, T. 2007, ApJ, 662, 504, doi: [10.1086/513562](https://doi.org/10.1086/513562)
- Berger, E. 2014, ARA&A, 52, 43, doi: [10.1146/annurev-astro-081913-035926](https://doi.org/10.1146/annurev-astro-081913-035926)
- Bertelli, G., Bressan, A., Chiosi, C., Fagotto, F., & Nasi, E. 1994, A&AS, 106, 275
- Blaauw, A. 1961, BAN, 15, 265
- Boersma, J. 1961, BAN, 15, 291
- Bolton, C. T. 1972, Nature, 235, 271, doi: [10.1038/235271b0](https://doi.org/10.1038/235271b0)
- Bovy, J., Leung, H. W., Hunt, J. A. S., et al. 2019, MNRAS, 490, 4740, doi: [10.1093/mnras/stz2891](https://doi.org/10.1093/mnras/stz2891)
- Bovy, J., Rix, H.-W., Schlafly, E. F., et al. 2016, ApJ, 823, 30, doi: [10.3847/0004-637X/823/1/30](https://doi.org/10.3847/0004-637X/823/1/30)
- Brandt, N., & Podsiadlowski, P. 1995, MNRAS, 274, 461, doi: [10.1093/mnras/274.2.461](https://doi.org/10.1093/mnras/274.2.461)
- Breivik, K., Coughlin, S., Zevin, M., et al. 2020, ApJ, 898, 71, doi: [10.3847/1538-4357/ab9d85](https://doi.org/10.3847/1538-4357/ab9d85)

⁷For the latest pip installable version of STROOPWAFEL please contact Floor Broekgaarden.

- 2055 Breivik, K., Rodriguez, C. L., Larson, S. L., Kalogera, V.,
 2056 & Rasio, F. A. 2016, ApJL, 830, L18,
 2057 doi: [10.3847/2041-8205/830/1/L18](https://doi.org/10.3847/2041-8205/830/1/L18)
- 2058 Broekgaarden, F. S. 2021a, BHBB simulations from:
 2059 Impact of Massive Binary Star and Cosmic Evolution on
 2060 Gravitational Wave Observations II: Double Compact
 2061 Object Mergers, 1, Zenodo, doi: [10.5281/zenodo.5651073](https://doi.org/10.5281/zenodo.5651073)
 2062 —. 2021b, BHNS simulations from: Impact of Massive
 2063 Binary Star and Cosmic Evolution on Gravitational
 2064 Wave Observations II: Double Compact Object Mergers,
 2065 1, Zenodo, doi: [10.5281/zenodo.5178777](https://doi.org/10.5281/zenodo.5178777)
 2066 —. 2021c, NSNS simulations from: Impact of Massive
 2067 Binary Star and Cosmic Evolution on Gravitational
 2068 Wave Observations II: Double Compact Object Mergers,
 2069 1, Zenodo, doi: [10.5281/zenodo.5189849](https://doi.org/10.5281/zenodo.5189849)
- 2070 Broekgaarden, F. S., Berger, E., Neijssel, C. J., et al.
 2071 2021a, arXiv e-prints, arXiv:2103.02608.
<https://arxiv.org/abs/2103.02608>
- 2072 Broekgaarden, F. S., Justham, S., de Mink, S. E., et al.
 2073 2019, MNRAS, 490, 5228, doi: [10.1093/mnras/stz2558](https://doi.org/10.1093/mnras/stz2558)
- 2074 Broekgaarden, F. S., Berger, E., Stevenson, S., et al. 2021b,
 2075 arXiv e-prints, arXiv:2112.05763.
<https://arxiv.org/abs/2112.05763>
- 2076 Brown, G. E. 1995, ApJ, 440, 270, doi: [10.1086/175268](https://doi.org/10.1086/175268)
- 2077 Chandrasekhar, S. 1931, ApJ, 74, 81, doi: [10.1086/143324](https://doi.org/10.1086/143324)
- 2078 Chattopadhyay, D., Stevenson, S., Hurley, J. R., Bailes,
 2079 M., & Broekgaarden, F. 2020, arXiv e-prints,
 2080 arXiv:2011.13503. <https://arxiv.org/abs/2011.13503>
- 2081 Chruslinska, M., Belczynski, K., Bulik, T., & Gladysz, W.
 2082 2017, AcA, 67, 37
- 2083 Collette, A., Kluyver, T., Caswell, T. A., et al. 2021,
 2084 h5py/h5py: 3.3.0, 3.3.0, Zenodo,
 2085 doi: [10.5281/zenodo.594310](https://doi.org/10.5281/zenodo.594310)
- 2086 Colpi, M., Holley-Bockelmann, K., Bogdanovic, T., et al.
 2087 2019, arXiv e-prints, arXiv:1903.06867.
<https://arxiv.org/abs/1903.06867>
- 2088 Corral-Santana, J. M., Casares, J., Muñoz-Darias, T., et al.
 2089 2016, A&A, 587, A61, doi: [10.1051/0004-6361/201527130](https://doi.org/10.1051/0004-6361/201527130)
- 2090 de Kool, M. 1990, ApJ, 358, 189, doi: [10.1086/168974](https://doi.org/10.1086/168974)
- 2091 De Marco, O., Passy, J.-C., Moe, M., et al. 2011, MNRAS,
 2092 411, 2277, doi: [10.1111/j.1365-2966.2010.17891.x](https://doi.org/10.1111/j.1365-2966.2010.17891.x)
- 2093 de Mink, S. E., & Belczynski, K. 2015, ApJ, 814, 58,
 2094 doi: [10.1088/0004-637X/814/1/58](https://doi.org/10.1088/0004-637X/814/1/58)
- 2095 de Mink, S. E., Cantiello, M., Langer, N., et al. 2009, A&A,
 2096 497, 243, doi: [10.1051/0004-6361/200811439](https://doi.org/10.1051/0004-6361/200811439)
- 2097 de Mink, S. E., Pols, O. R., & Hilditch, R. W. 2007, A&A,
 2098 467, 1181
- 2099 Dewdney, P. E., Hall, P. J., Schilizzi, R. T., & Lazio,
 2100 T. J. L. W. 2009, IEEE Proceedings, 97, 1482,
 2101 doi: [10.1109/JPROC.2009.2021005](https://doi.org/10.1109/JPROC.2009.2021005)
- 2102 Dewi, J. D. M., Pols, O. R., Savonije, G. J., & van den
 2103 Heuvel, E. P. J. 2002, MNRAS, 331, 1027,
 2104 doi: [10.1046/j.1365-8711.2002.05257.x](https://doi.org/10.1046/j.1365-8711.2002.05257.x)
- 2105 Di Carlo, U. N., Mapelli, M., Giacobbo, N., et al. 2020,
 2106 MNRAS, 498, 495, doi: [10.1093/mnras/staa2286](https://doi.org/10.1093/mnras/staa2286)
- 2107 Dominik, M., Berti, E., O'Shaughnessy, R., et al. 2015,
 2108 ApJ, 806, 263, doi: [10.1088/0004-637X/806/2/263](https://doi.org/10.1088/0004-637X/806/2/263)
- 2109 Dosopoulou, F., & Kalogera, V. 2016a, ApJ, 825, 70,
 2110 doi: [10.3847/0004-637X/825/1/70](https://doi.org/10.3847/0004-637X/825/1/70)
- 2111 —. 2016b, ApJ, 825, 71, doi: [10.3847/0004-637X/825/1/71](https://doi.org/10.3847/0004-637X/825/1/71)
- 2112 du Buisson, L., Marchant, P., Podsiadlowski, P., et al. 2020,
 2113 MNRAS, 499, 5941, doi: [10.1093/mnras/staa3225](https://doi.org/10.1093/mnras/staa3225)
- 2114 Eichler, D., Livio, M., Piran, T., & Schramm, D. N. 1989,
 2115 Nature, 340, 126, doi: [10.1038/340126a0](https://doi.org/10.1038/340126a0)
- 2116 El-Badry, K., & Quataert, E. 2020, MNRAS, 493, L22,
 2117 doi: [10.1093/mnrasl/slaa004](https://doi.org/10.1093/mnrasl/slaa004)
- 2118 Eldridge, J. J., Stanway, E. R., Breivik, K., et al. 2020,
 2119 MNRAS, 495, 2786, doi: [10.1093/mnras/staa1324](https://doi.org/10.1093/mnras/staa1324)
- 2120 Farmer, R., Renzo, M., de Mink, S. E., Marchant, P., &
 2121 Justham, S. 2019, ApJ, 887, 53,
 2122 doi: [10.3847/1538-4357/ab518b](https://doi.org/10.3847/1538-4357/ab518b)
- 2123 Farr, W. M., Sravan, N., Cantrell, A., et al. 2011, ApJ, 741,
 2124 103, doi: [10.1088/0004-637X/741/2/103](https://doi.org/10.1088/0004-637X/741/2/103)
- 2125 Finn, L. S., & Thorne, K. S. 2000, PhRvD, 62, 124021,
 2126 doi: [10.1103/PhysRevD.62.124021](https://doi.org/10.1103/PhysRevD.62.124021)
- 2127 Frankel, N., Rix, H.-W., Ting, Y.-S., Ness, M., & Hogg,
 2128 D. W. 2018, ApJ, 865, 96,
 2129 doi: [10.3847/1538-4357/aadba5](https://doi.org/10.3847/1538-4357/aadba5)
- 2130 Fryer, C. L., Belczynski, K., Ramirez-Ruiz, E., et al. 2015,
 2131 ApJ, 812, 24, doi: [10.1088/0004-637X/812/1/24](https://doi.org/10.1088/0004-637X/812/1/24)
- 2132 Fryer, C. L., Belczynski, K., Wiktorowicz, G., et al. 2012,
 2133 ApJ, 749, 91, doi: [10.1088/0004-637X/749/1/91](https://doi.org/10.1088/0004-637X/749/1/91)
- 2134 Gerosa, D., Ma, S., Wong, K. W. K., et al. 2019, PhRvD,
 2135 99, 103004, doi: [10.1103/PhysRevD.99.103004](https://doi.org/10.1103/PhysRevD.99.103004)
- 2136 Ginat, Y. B., Glanz, H., Perets, H. B., Grishin, E., &
 2137 Desjacques, V. 2020, MNRAS, 493, 4861,
 2138 doi: [10.1093/mnras/staa465](https://doi.org/10.1093/mnras/staa465)
- 2139 Gosnell, N. M., Leiner, E. M., Mathieu, R. D., et al. 2019,
 2140 ApJ, 885, 45, doi: [10.3847/1538-4357/ab4273](https://doi.org/10.3847/1538-4357/ab4273)
- 2141 Griffith, E., Weinberg, D. H., Johnson, J. A., et al. 2021,
 2142 ApJ, 909, 77, doi: [10.3847/1538-4357/abbd6be](https://doi.org/10.3847/1538-4357/abbd6be)
- 2143 Hamada, T., & Salpeter, E. E. 1961, ApJ, 134, 683,
 2144 doi: [10.1086/147195](https://doi.org/10.1086/147195)
- 2145 Hamann, W. R., Gräfener, G., Liermann, A., et al. 2019,
 2146 A&A, 625, A57, doi: [10.1051/0004-6361/201834850](https://doi.org/10.1051/0004-6361/201834850)
- 2147 Hamann, W. R., & Koesterke, L. 1998, A&A, 335, 1003
- 2148 Harris, C. R., Millman, K. J., van der Walt, S. J., et al.
 2149 2020, Nature, 585, 357–362,
 2150 doi: [10.1038/s41586-020-2649-2](https://doi.org/10.1038/s41586-020-2649-2)

- 2154 Hjellming, M. S., & Webbink, R. F. 1987, ApJ, 318, 794,
2155 doi: [10.1086/165412](https://doi.org/10.1086/165412)
- 2156 Hobbs, G., Lorimer, D. R., Lyne, A. G., & Kramer, M.
2157 2005, MNRAS, 360, 974,
2158 doi: [10.1111/j.1365-2966.2005.09087.x](https://doi.org/10.1111/j.1365-2966.2005.09087.x)
- 2159 Hopkins, P. F., Kereš, D., Oñorbe, J., et al. 2014, MNRAS,
2160 445, 581, doi: [10.1093/mnras/stu1738](https://doi.org/10.1093/mnras/stu1738)
- 2161 Hotokezaka, K., Nissanke, S., Hallinan, G., et al. 2016,
2162 ApJ, 831, 190, doi: [10.3847/0004-637X/831/2/190](https://doi.org/10.3847/0004-637X/831/2/190)
- 2163 Hulse, R. A., & Taylor, J. H. 1975, ApJL, 195, L51,
2164 doi: [10.1086/181708](https://doi.org/10.1086/181708)
- 2165 Hunter, J. D. 2007, Computing in Science and Engineering,
2166 9, 90, doi: [10.1109/MCSE.2007.55](https://doi.org/10.1109/MCSE.2007.55)
- 2167 Hurley, J. R., Pols, O. R., & Tout, C. A. 2000, MNRAS,
2168 315, 543, doi: [10.1046/j.1365-8711.2000.03426.x](https://doi.org/10.1046/j.1365-8711.2000.03426.x)
- 2169 Hurley, J. R., Tout, C. A., & Pols, O. R. 2002, MNRAS,
2170 329, 897, doi: [10.1046/j.1365-8711.2002.05038.x](https://doi.org/10.1046/j.1365-8711.2002.05038.x)
- 2171 Ivanova, N., Heinke, C. O., Rasio, F. A., Belczynski, K., &
2172 Fregeau, J. M. 2008, MNRAS, 386, 553,
2173 doi: [10.1111/j.1365-2966.2008.13064.x](https://doi.org/10.1111/j.1365-2966.2008.13064.x)
- 2174 Ivanova, N., & Taam, R. E. 2004, ApJ, 601, 1058,
2175 doi: [10.1086/380561](https://doi.org/10.1086/380561)
- 2176 Ivanova, N., Justham, S., Chen, X., et al. 2013, A&A Rv,
2177 21, 59, doi: [10.1007/s00159-013-0059-2](https://doi.org/10.1007/s00159-013-0059-2)
- 2178 Kalogera, V., & Baym, G. 1996, ApJL, 470, L61,
2179 doi: [10.1086/310296](https://doi.org/10.1086/310296)
- 2180 Kalogera, V., Belczynski, K., Kim, C., O'Shaughnessy, R.,
2181 & Willems, B. 2007, PhR, 442, 75,
2182 doi: [10.1016/j.physrep.2007.02.008](https://doi.org/10.1016/j.physrep.2007.02.008)
- 2183 Keane, E., Bhattacharyya, B., Kramer, M., et al. 2015, in
2184 Advancing Astrophysics with the Square Kilometre Array
2185 (AASKA14), 40. <https://arxiv.org/abs/1501.00056>
- 2186 Klein, A., Barausse, E., Sesana, A., et al. 2016, PhRvD, 93,
2187 024003, doi: [10.1103/PhysRevD.93.024003](https://doi.org/10.1103/PhysRevD.93.024003)
- 2188 Klencki, J., Moe, M., Gladysz, W., et al. 2018, A&A, 619,
2189 A77
- 2190 Klencki, J., Nelemans, G., Istrate, A. G., & Chruslinska, M.
2191 2021, A&A, 645, A54, doi: [10.1051/0004-6361/202038707](https://doi.org/10.1051/0004-6361/202038707)
- 2192 Kluyver, T., Ragan-Kelley, B., Pérez, F., et al. 2016, in
2193 Positioning and Power in Academic Publishing: Players,
2194 Agents and Agendas, ed. F. Loizides & B. Schmidt, IOS
2195 Press, 87 – 90
- 2196 Korol, V., Rossi, E. M., & Barausse, E. 2019, MNRAS, 483,
2197 5518, doi: [10.1093/mnras/sty3440](https://doi.org/10.1093/mnras/sty3440)
- 2198 Korol, V., Rossi, E. M., Groot, P. J., et al. 2017, MNRAS,
2199 470, 1894, doi: [10.1093/mnras/stx1285](https://doi.org/10.1093/mnras/stx1285)
- 2200 Korol, V., & Safarzadeh, M. 2021, MNRAS, 502, 5576,
2201 doi: [10.1093/mnras/stab310](https://doi.org/10.1093/mnras/stab310)
- 2202 Korol, V., Toonen, S., Klein, A., et al. 2020, A&A, 638,
2203 A153, doi: [10.1051/0004-6361/202037764](https://doi.org/10.1051/0004-6361/202037764)
- 2204 Kreidberg, L., Bailyn, C. D., Farr, W. M., & Kalogera, V.
2205 2012, ApJ, 757, 36, doi: [10.1088/0004-637X/757/1/36](https://doi.org/10.1088/0004-637X/757/1/36)
- 2206 Kremer, K., Chatterjee, S., Breivik, K., et al. 2018, PhRvL,
2207 120, 191103, doi: [10.1103/PhysRevLett.120.191103](https://doi.org/10.1103/PhysRevLett.120.191103)
- 2208 Kroupa, P. 2001, MNRAS, 322, 231,
2209 doi: [10.1046/j.1365-8711.2001.04022.x](https://doi.org/10.1046/j.1365-8711.2001.04022.x)
- 2210 Kummer, F. 2020, UvA Scripties
- 2211 Kupfer, T., Korol, V., Shah, S., et al. 2018, MNRAS, 480,
2212 302, doi: [10.1093/mnras/sty1545](https://doi.org/10.1093/mnras/sty1545)
- 2213 Kyutoku, K., Kiuchi, K., Sekiguchi, Y., Shibata, M., &
2214 Taniguchi, K. 2018, PhRvD, 97, 023009,
2215 doi: [10.1103/PhysRevD.97.023009](https://doi.org/10.1103/PhysRevD.97.023009)
- 2216 Kyutoku, K., Nishino, Y., & Seto, N. 2019, MNRAS, 483,
2217 2615, doi: [10.1093/mnras/sty3322](https://doi.org/10.1093/mnras/sty3322)
- 2218 Lamberts, A., Blunt, S., Littenberg, T. B., et al. 2019,
2219 MNRAS, 490, 5888, doi: [10.1093/mnras/stz2834](https://doi.org/10.1093/mnras/stz2834)
- 2220 Lamberts, A., Garrison-Kimmel, S., Hopkins, P. F., et al.
2221 2018, MNRAS, 480, 2704, doi: [10.1093/mnras/sty2035](https://doi.org/10.1093/mnras/sty2035)
- 2222 Langer, N. 2012, ARA&A, 50, 107
- 2223 Laplace, E., Götberg, Y., de Mink, S. E., Justham, S., &
2224 Farmer, R. 2020, A&A, 637, A6
- 2225 Lau, M. Y. M., Hirai, R., González-Bolívar, M., et al. 2021,
2226 arXiv e-prints, arXiv:2111.00923.
2227 <https://arxiv.org/abs/2111.00923>
- 2228 Lau, M. Y. M., Mandel, I., Vigna-Gómez, A., et al. 2020,
2229 MNRAS, 492, 3061, doi: [10.1093/mnras/staa002](https://doi.org/10.1093/mnras/staa002)
- 2230 Law-Smith, J. A. P., Everson, R. W., Ramirez-Ruiz, E.,
2231 et al. 2020, arXiv e-prints, arXiv:2011.06630.
2232 <https://arxiv.org/abs/2011.06630>
- 2233 Li, L.-X., & Paczyński, B. 1998, ApJL, 507, L59,
2234 doi: [10.1086/311680](https://doi.org/10.1086/311680)
- 2235 Licquia, T. C., & Newman, J. A. 2015, ApJ, 806, 96,
2236 doi: [10.1088/0004-637X/806/1/96](https://doi.org/10.1088/0004-637X/806/1/96)
- 2237 Liu, J., Soria, R., Zheng, Z., et al. 2020, Nature, 580, E16,
2238 doi: [10.1038/s41586-020-2217-9](https://doi.org/10.1038/s41586-020-2217-9)
- 2239 Liu, J., Zhang, H., Howard, A. W., et al. 2019, Nature, 575,
2240 618, doi: [10.1038/s41586-019-1766-2](https://doi.org/10.1038/s41586-019-1766-2)
- 2241 Liu, J., & Zhang, Y. 2014, PASP, 126, 211,
2242 doi: [10.1086/675721](https://doi.org/10.1086/675721)
- 2243 Lyne, A. G., & Lorimer, D. R. 1994, Nature, 369, 127,
2244 doi: [10.1038/s41586-019-1766-2](https://doi.org/10.1038/s41586-019-1766-2)
- 2245 Majewski, S. R., Schiavon, R. P., Frinchaboy, P. M., et al.
2246 2017, AJ, 154, 94, doi: [10.3847/1538-3881/aa784d](https://doi.org/10.3847/1538-3881/aa784d)
- 2247 Manchester, R. N., Hobbs, G. B., Teoh, A., & Hobbs, M.
2248 2005, AJ, 129, 1993, doi: [10.1086/428488](https://doi.org/10.1086/428488)
- 2249 Mandel, I., & Broekgaarden, F. S. 2021, arXiv e-prints,
2250 arXiv:2107.14239. <https://arxiv.org/abs/2107.14239>
- 2251 Mandel, I., & de Mink, S. E. 2016, MNRAS, 458, 2634,
2252 doi: [10.1093/mnras/stw379](https://doi.org/10.1093/mnras/stw379)

- 2253 Mandel, I., & Müller, B. 2020, MNRAS, 499, 3214,
2254 doi: [10.1093/mnras/staa3043](https://doi.org/10.1093/mnras/staa3043)
- 2255 Mandel, I., Sesana, A., & Vecchio, A. 2018, Classical and
2256 Quantum Gravity, 35, 054004,
2257 doi: [10.1088/1361-6382/aaa7e0](https://doi.org/10.1088/1361-6382/aaa7e0)
- 2258 Mapelli, M. 2021, Formation Channels of Single and Binary
2259 Stellar-Mass Black Holes (Springer), 4,
2260 doi: [10.1007/978-981-15-4702-7_16-1](https://doi.org/10.1007/978-981-15-4702-7_16-1)
- 2261 Marchant, P., Langer, N., Podsiadlowski, P., et al. 2017,
2262 A&A, 604, A55, doi: [10.1051/0004-6361/201630188](https://doi.org/10.1051/0004-6361/201630188)
- 2263 Marchant, P., Langer, N., Podsiadlowski, P., Tauris, T. M.,
2264 & Moriya, T. J. 2016, A&A, 588, A50,
2265 doi: [10.1051/0004-6361/201628133](https://doi.org/10.1051/0004-6361/201628133)
- 2266 Marchant, P., Renzo, M., Farmer, R., et al. 2019, ApJ, 882,
2267 36, doi: [10.3847/1538-4357/ab3426](https://doi.org/10.3847/1538-4357/ab3426)
- 2268 Margalit, B., & Metzger, B. D. 2017, ApJL, 850, L19,
2269 doi: [10.3847/2041-8213/aa991c](https://doi.org/10.3847/2041-8213/aa991c)
- 2270 Marsh, T. R., Nelemans, G., & Steeghs, D. 2004, MNRAS,
2271 350, 113, doi: [10.1111/j.1365-2966.2004.07564.x](https://doi.org/10.1111/j.1365-2966.2004.07564.x)
- 2272 Massevitch, A., & Yungelson, L. 1975,
2273 Mem. Soc. Astron. Italiana, 46, 217
- 2274 McKernan, B., Ford, K. E. S., & O’Shaughnessy, R. 2020,
2275 MNRAS, 498, 4088, doi: [10.1093/mnras/staa2681](https://doi.org/10.1093/mnras/staa2681)
- 2276 McMillan, P. J. 2011, MNRAS, 414, 2446,
2277 doi: [10.1111/j.1365-2966.2011.18564.x](https://doi.org/10.1111/j.1365-2966.2011.18564.x)
- 2278 Metzger, B. D. 2017, Living Reviews in Relativity, 20, 3,
2279 doi: [10.1007/s41114-017-0006-z](https://doi.org/10.1007/s41114-017-0006-z)
- 2280 Miller, M. C., & Lauburg, V. M. 2009, ApJ, 692, 917,
2281 doi: [10.1088/0004-637X/692/1/917](https://doi.org/10.1088/0004-637X/692/1/917)
- 2282 Miller-Jones, J. C. A., Bahramian, A., Orosz, J. A., et al.
2283 2021, Science, 371, 1046, doi: [10.1126/science.abb3363](https://doi.org/10.1126/science.abb3363)
- 2284 Morris, M. 1993, ApJ, 408, 496, doi: [10.1086/172607](https://doi.org/10.1086/172607)
- 2285 Nandez, J. L. A., & Ivanova, N. 2016, MNRAS, 460, 3992,
2286 doi: [10.1093/mnras/stw1266](https://doi.org/10.1093/mnras/stw1266)
- 2287 Narayan, R., Piran, T., & Shemi, A. 1991, ApJL, 379, L17,
2288 doi: [10.1086/186143](https://doi.org/10.1086/186143)
- 2289 Neijssel, C. J., Vigna-Gómez, A., Stevenson, S., et al. 2019,
2290 MNRAS, 490, 3740, doi: [10.1093/mnras/stz2840](https://doi.org/10.1093/mnras/stz2840)
- 2291 Nelemans, G., Yungelson, L. R., & Portegies Zwart, S. F.
2292 2001, A&A, 375, 890, doi: [10.1051/0004-6361:20010683](https://doi.org/10.1051/0004-6361:20010683)
- 2293 Nishizawa, A., Berti, E., Klein, A., & Sesana, A. 2016,
2294 PhRvD, 94, 064020, doi: [10.1103/PhysRevD.94.064020](https://doi.org/10.1103/PhysRevD.94.064020)
- 2295 Nissanke, S., Vallisneri, M., Nelemans, G., & Prince, T. A.
2296 2012, ApJ, 758, 131, doi: [10.1088/0004-637X/758/2/131](https://doi.org/10.1088/0004-637X/758/2/131)
- 2297 Nomoto, K. 1984, ApJ, 277, 791, doi: [10.1086/161749](https://doi.org/10.1086/161749)
2298 —. 1987, ApJ, 322, 206, doi: [10.1086/165716](https://doi.org/10.1086/165716)
- 2299 Öpik, E. 1924, Publications of the Tartu Astrofizika
2300 Observatory, 25, 1
- 2301 Özel, F., Psaltis, D., Narayan, R., & McClintock, J. E.
2302 2010, ApJ, 725, 1918,
2303 doi: [10.1088/0004-637X/725/2/1918](https://doi.org/10.1088/0004-637X/725/2/1918)
- 2304 Paczyński, B., & Sienkiewicz, R. 1972, AcA, 22, 73
- 2305 Peters, P. C. 1964, Physical Review, 136, 1224,
2306 doi: [10.1103/PhysRev.136.B1224](https://doi.org/10.1103/PhysRev.136.B1224)
- 2307 Peters, P. C., & Mathews, J. 1963, Physical Review, 131,
2308 435, doi: [10.1103/PhysRev.131.435](https://doi.org/10.1103/PhysRev.131.435)
- 2309 Pfahl, E., Podsiadlowski, P., & Rappaport, S. 2005, ApJ,
2310 628, 343, doi: [10.1086/430515](https://doi.org/10.1086/430515)
- 2311 Pfahl, E., Rappaport, S., Podsiadlowski, P., & Spruit, H.
2312 2002, ApJ, 574, 364, doi: [10.1086/340794](https://doi.org/10.1086/340794)
- 2313 Podsiadlowski, P., Langer, N., Poelarends, A. J. T., et al.
2314 2004, ApJ, 612, 1044, doi: [10.1086/421713](https://doi.org/10.1086/421713)
- 2315 Pol, N., McLaughlin, M., & Lorimer, D. 2021, arXiv
2316 e-prints, arXiv:2109.04512.
2317 <https://arxiv.org/abs/2109.04512>
- 2318 Pols, O. R., Schröder, K.-P., Hurley, J. R., Tout, C. A., &
2319 Eggleton, P. P. 1998, MNRAS, 298, 525,
2320 doi: [10.1046/j.1365-8711.1998.01658.x](https://doi.org/10.1046/j.1365-8711.1998.01658.x)
- 2321 Portegies Zwart, S. F., & McMillan, S. L. W. 2000, ApJL,
2322 528, L17, doi: [10.1086/312422](https://doi.org/10.1086/312422)
- 2323 Rastello, S., Mapelli, M., Di Carlo, U. N., et al. 2020,
2324 MNRAS, 497, 1563, doi: [10.1093/mnras/staa2018](https://doi.org/10.1093/mnras/staa2018)
- 2325 Rastello, S., Mapelli, M., di Carlo, U. N., et al. 2021, arXiv
2326 e-prints, arXiv:2105.01669.
2327 <https://arxiv.org/abs/2105.01669>
- 2328 Renzo, M., Callister, T., Chatzioannou, K., et al. 2021,
2329 ApJ, 919, 128, doi: [10.3847/1538-4357/ac1110](https://doi.org/10.3847/1538-4357/ac1110)
- 2330 Robson, T., Cornish, N. J., & Liu, C. 2019, Classical and
2331 Quantum Gravity, 36, 105011,
2332 doi: [10.1088/1361-6382/ab1101](https://doi.org/10.1088/1361-6382/ab1101)
- 2333 Rodriguez, C. L., Amaro-Seoane, P., Chatterjee, S., &
2334 Rasio, F. A. 2018, PhRvL, 120, 151101,
2335 doi: [10.1103/PhysRevLett.120.151101](https://doi.org/10.1103/PhysRevLett.120.151101)
- 2336 Rodriguez, C. L., Morscher, M., Pattabiraman, B., et al.
2337 2015, PhRvL, 115, 051101,
2338 doi: [10.1103/PhysRevLett.115.051101](https://doi.org/10.1103/PhysRevLett.115.051101)
- 2339 Ruiter, A. J., Belczynski, K., Benacquista, M., Larson,
2340 S. L., & Williams, G. 2010, ApJ, 717, 1006,
2341 doi: [10.1088/0004-637X/717/2/1006](https://doi.org/10.1088/0004-637X/717/2/1006)
- 2342 Sana, H., de Mink, S. E., de Koter, A., et al. 2012, Science,
2343 337, 444, doi: [10.1126/science.1223344](https://doi.org/10.1126/science.1223344)
- 2344 Sander, A. A. C., & Vink, J. S. 2020, MNRAS, 499, 873,
2345 doi: [10.1093/mnras/staa2712](https://doi.org/10.1093/mnras/staa2712)
- 2346 Schneider, F. R. N., Izzard, R. G., Langer, N., & de Mink,
2347 S. E. 2015, ApJ, 805, 20
- 2348 Schreier, R., Hillel, S., Shiber, S., & Soker, N. 2021,
2349 MNRAS, 508, 2386, doi: [10.1093/mnras/stab2687](https://doi.org/10.1093/mnras/stab2687)

- 2350 Schuster, E. F. 1985, Communications in Statistics-theory
 2351 and Methods, 14, 1123
- 2352 Sellwood, J. A., & Binney, J. J. 2002, MNRAS, 336, 785,
 2353 doi: [10.1046/j.1365-8711.2002.05806.x](https://doi.org/10.1046/j.1365-8711.2002.05806.x)
- 2354 Sesana, A. 2016, PhRvL, 116, 231102,
 2355 doi: [10.1103/PhysRevLett.116.231102](https://doi.org/10.1103/PhysRevLett.116.231102)
- 2356 Sesana, A., Lamberts, A., & Petiteau, A. 2020, MNRAS,
 2357 494, L75, doi: [10.1093/mnrasl/slaa039](https://doi.org/10.1093/mnrasl/slaa039)
- 2358 Shao, Y., & Li, X.-D. 2021, arXiv e-prints,
 2359 arXiv:2107.03565. <https://arxiv.org/abs/2107.03565>
- 2360 Sharma, S., Hayden, M. R., & Bland-Hawthorn, J. 2020,
 2361 arXiv e-prints, arXiv:2005.03646.
<https://arxiv.org/abs/2005.03646>
- 2362 Shenar, T., Bodensteiner, J., Abdul-Masih, M., et al. 2020,
 2363 A&A, 639, L6, doi: [10.1051/0004-6361/202038275](https://doi.org/10.1051/0004-6361/202038275)
- 2364 Shenar, T., Sablowski, D. P., Hainich, R., et al. 2019, A&A,
 2365 627, A151, doi: [10.1051/0004-6361/201935684](https://doi.org/10.1051/0004-6361/201935684)
- 2366 Sigurdsson, S., & Hernquist, L. 1993, Nature, 364, 423,
 2367 doi: [10.1038/364423a0](https://doi.org/10.1038/364423a0)
- 2368 Silsbee, K., & Tremaine, S. 2017, ApJ, 836, 39,
 2369 doi: [10.3847/1538-4357/aa5729](https://doi.org/10.3847/1538-4357/aa5729)
- 2370 Smarr, L. L., & Blandford, R. 1976, ApJ, 207, 574,
 2371 doi: [10.1086/154524](https://doi.org/10.1086/154524)
- 2372 Smits, R., Kramer, M., Stappers, B., et al. 2009, A&A, 493,
 2373 1161, doi: [10.1051/0004-6361/200810383](https://doi.org/10.1051/0004-6361/200810383)
- 2374 Snaith, O. N., Haywood, M., Di Matteo, P., et al. 2014,
 2375 ApJL, 781, L31, doi: [10.1088/2041-8205/781/2/L31](https://doi.org/10.1088/2041-8205/781/2/L31)
- 2376 Soberman, G. E., Phinney, E. S., & van den Heuvel,
 2377 E. P. J. 1997, A&A, 327, 620.
<https://arxiv.org/abs/astro-ph/9703016>
- 2378 Srinivasan, G. 1989, A&A Rv, 1, 209,
 2379 doi: [10.1007/BF00873079](https://doi.org/10.1007/BF00873079)
- 2380 Stephan, A. P., Naoz, S., Ghez, A. M., et al. 2016,
 2381 MNRAS, 460, 3494, doi: [10.1093/mnras/stw1220](https://doi.org/10.1093/mnras/stw1220)
- 2382 Stevenson, S., Sampson, M., Powell, J., et al. 2019, ApJ,
 2383 882, 121, doi: [10.3847/1538-4357/ab3981](https://doi.org/10.3847/1538-4357/ab3981)
- 2384 Stevenson, S., Vigna-Gómez, A., Mandel, I., et al. 2017,
 2385 Nature Communications, 8, 14906,
 2386 doi: [10.1038/ncomms14906](https://doi.org/10.1038/ncomms14906)
- 2387 Taam, R. E., & Sandquist, E. L. 2000, ARA&A, 38, 113,
 2388 doi: [10.1146/annurev.astro.38.1.113](https://doi.org/10.1146/annurev.astro.38.1.113)
- 2389 Takahashi, R., & Seto, N. 2002, ApJ, 575, 1030,
 2390 doi: [10.1086/341483](https://doi.org/10.1086/341483)
- 2391 Tamanini, N., & Danielski, C. 2019, Nature Astronomy, 3,
 2392 858, doi: [10.1038/s41550-019-0807-y](https://doi.org/10.1038/s41550-019-0807-y)
- 2393 Tauris, T. M., Kramer, M., Freire, P. C. C., et al. 2017,
 2394 ApJ, 846, 170, doi: [10.3847/1538-4357/aa7e89](https://doi.org/10.3847/1538-4357/aa7e89)
- 2395 Tauris, T. M., Langer, N., Moriya, T. J., et al. 2013, ApJL,
 2396 778, L23, doi: [10.1088/2041-8205/778/2/L23](https://doi.org/10.1088/2041-8205/778/2/L23)
- 2397 Tauris, T. M., Langer, N., & Podsiadlowski, P. 2015,
 2398 MNRAS, 451, 2123, doi: [10.1093/mnras/stv990](https://doi.org/10.1093/mnras/stv990)
- 2400 Team COMPAS: J. Riley, Riley, J., Agrawal, P., et al.
 2401 2021, arXiv e-prints, arXiv:2109.10352.
<https://arxiv.org/abs/2109.10352>
- 2402 The LIGO Scientific Collaboration, the Virgo
 2403 Collaboration, Abbott, R., et al. 2021a, arXiv e-prints,
 2404 arXiv:2108.01045. <https://arxiv.org/abs/2108.01045>
- 2405 The LIGO Scientific Collaboration, the Virgo
 2406 Collaboration, the KAGRA Collaboration, et al. 2021b,
 2407 arXiv e-prints, arXiv:2106.15163.
<https://arxiv.org/abs/2106.15163>
- 2408 The LIGO Scientific Collaboration, The Virgo
 2409 Collaboration, & The KAGRA Scientific Collaboration.
 2410 2021c, arXiv e-prints, arXiv:2111.03634.
<https://arxiv.org/abs/2111.03634>
- 2411 Thrane, E., Osłowski, S., & Lasky, P. D. 2020, MNRAS,
 2412 493, 5408, doi: [10.1093/mnras/staa593](https://doi.org/10.1093/mnras/staa593)
- 2413 Timmes, F. X., Woosley, S. E., & Weaver, T. A. 1996, ApJ,
 2414 457, 834, doi: [10.1086/176778](https://doi.org/10.1086/176778)
- 2415 Toonen, S., Claeys, J. S. W., Mennekens, N., & Ruiter,
 2416 A. J. 2014, A&A, 562, A14,
 2417 doi: [10.1051/0004-6361/201321576](https://doi.org/10.1051/0004-6361/201321576)
- 2418 Toonen, S., Portegies Zwart, S., Hamers, A. S., &
 2419 Bandopadhyay, D. 2020, A&A, 640, A16,
 2420 doi: [10.1051/0004-6361/201936835](https://doi.org/10.1051/0004-6361/201936835)
- 2421 Tout, C. A., Pols, O. R., Eggleton, P. P., & Han, Z. 1996,
 2422 MNRAS, 281, 257, doi: [10.1093/mnras/281.1.257](https://doi.org/10.1093/mnras/281.1.257)
- 2423 Tutukov, A., & Yungelson, L. 1973, Nauchnye Informatsii,
 2424 27, 70
- 2425 Tutukov, A. V., & Yungelson, L. R. 1993, MNRAS, 260,
 2426 675, doi: [10.1093/mnras/260.3.675](https://doi.org/10.1093/mnras/260.3.675)
- 2427 van den Heuvel, E. P. J. 2011, Compact stars and the
 2428 evolution of binary systems (World Scientific Publishing
 2429 Co. Pte. Ltd), 55–73, doi: [10.1142/9789814374774_0006](https://doi.org/10.1142/9789814374774_0006)
- 2430 van den Heuvel, E. P. J., Portegies Zwart, S. F., & de
 2431 Mink, S. E. 2017, MNRAS, 471, 4256,
 2432 doi: [10.1093/mnras/stx1430](https://doi.org/10.1093/mnras/stx1430)
- 2433 van Son, L. A. C., de Mink, S. E., Callister, T., et al. 2021,
 2434 arXiv e-prints, arXiv:2110.01634.
<https://arxiv.org/abs/2110.01634>
- 2435 van Son, L. A. C., De Mink, S. E., Broekgaarden, F. S.,
 2436 et al. 2020, ApJ, 897, 100
- 2437 Vigna-Gómez, A., Neijssel, C. J., Stevenson, S., et al. 2018,
 2438 MNRAS, 481, 4009, doi: [10.1093/mnras/sty2463](https://doi.org/10.1093/mnras/sty2463)
- 2439 Vink, J. S. 2017, A&A, 607, L8,
 2440 doi: [10.1051/0004-6361/201731902](https://doi.org/10.1051/0004-6361/201731902)
- 2441 Vink, J. S., & de Koter, A. 2005, A&A, 442, 587,
 2442 doi: [10.1051/0004-6361:20052862](https://doi.org/10.1051/0004-6361:20052862)

- ²⁴⁴⁸ Vink, J. S., de Koter, A., & Lamers, H. J. G. L. M. 2000,
²⁴⁴⁹ A&A, 362, 295. <https://arxiv.org/abs/astro-ph/0008183>
- ²⁴⁵⁰ —. 2001, A&A, 369, 574, doi: [10.1051/0004-6361:20010127](https://doi.org/10.1051/0004-6361:20010127)
- ²⁴⁵¹ Virtanen, P., Gommers, R., Oliphant, T. E., et al. 2020,
²⁴⁵² Nature Methods, 17, 261, doi: [10.1038/s41592-019-0686-2](https://doi.org/10.1038/s41592-019-0686-2)
- ²⁴⁵³ Vynatheya, P., & Hamers, A. S. 2021, arXiv e-prints,
²⁴⁵⁴ arXiv:2110.14680
- ²⁴⁵⁵ Wagg, T., Breivik, K., & de Mink, S. E. 2021, arXiv
²⁴⁵⁶ e-prints, arXiv:2111.08717.
²⁴⁵⁷ <https://arxiv.org/abs/2111.08717>
- ²⁴⁵⁸ Wagg, T., Broekgaarden, F., de Mink, S., et al. 2021,
²⁴⁵⁹ Dataset from: Gravitational wave sources in our Galactic
²⁴⁶⁰ backyard - Predictions for BHBH, BHNS and NSNS
²⁴⁶¹ binaries in LISA, 0.0.1, Zenodo,
²⁴⁶² doi: [10.5281/zenodo.5725607](https://doi.org/10.5281/zenodo.5725607)
- ²⁴⁶³ Waskom, M. 2021, The Journal of Open Source Software, 6,
²⁴⁶⁴ 3021, doi: [10.21105/joss.03021](https://doi.org/10.21105/joss.03021)
- ²⁴⁶⁵ Webbink, R. F. 1984, ApJ, 277, 355, doi: [10.1086/161701](https://doi.org/10.1086/161701)
- ²⁴⁶⁶ Webster, B. L., & Murdin, P. 1972, Nature, 235, 37,
²⁴⁶⁷ doi: [10.1038/235037a0](https://doi.org/10.1038/235037a0)
- ²⁴⁶⁸ Wegg, C., Gerhard, O., & Portail, M. 2015, MNRAS, 450,
²⁴⁶⁹ 4050, doi: [10.1093/mnras/stv745](https://doi.org/10.1093/mnras/stv745)
- ²⁴⁷⁰ Willemse, B., Kalogera, V., Vecchio, A., et al. 2007, ApJL,
²⁴⁷¹ 665, L59, doi: [10.1086/521049](https://doi.org/10.1086/521049)
- ²⁴⁷² Woosley, S. E., Blinnikov, S., & Heger, A. 2007, Nature,
²⁴⁷³ 450, 390, doi: [10.1038/nature06333](https://doi.org/10.1038/nature06333)
- ²⁴⁷⁴ Xu, X.-J., & Li, X.-D. 2010a, ApJ, 716, 114,
²⁴⁷⁵ doi: [10.1088/0004-637X/716/1/114](https://doi.org/10.1088/0004-637X/716/1/114)
- ²⁴⁷⁶ —. 2010b, ApJ, 722, 1985,
²⁴⁷⁷ doi: [10.1088/0004-637X/722/2/1985](https://doi.org/10.1088/0004-637X/722/2/1985)
- ²⁴⁷⁸ Yu, S., & Jeffery, C. S. 2010, A&A, 521, A85,
²⁴⁷⁹ doi: [10.1051/0004-6361/201014827](https://doi.org/10.1051/0004-6361/201014827)
- ²⁴⁸⁰ Zapartas, E., de Mink, S. E., Izzard, R. G., et al. 2017,
²⁴⁸¹ A&A, 601, A29, doi: [10.1051/0004-6361/201629685](https://doi.org/10.1051/0004-6361/201629685)
- ²⁴⁸² Ziosi, B. M., Mapelli, M., Branchesi, M., & Tormen, G.
²⁴⁸³ 2014, MNRAS, 441, 3703, doi: [10.1093/mnras/stu824](https://doi.org/10.1093/mnras/stu824)

APPENDIX

2485 A. POPULATION SYNTHESIS

2486 In this section we summarise the main assumptions
 2487 and settings from the population synthesis simulation
 2488 from Broekgaarden et al. (2021a,b).

2489 A.1. Initial conditions

2490 Broekgaarden et al. (2021a,b) simulate between 1 and
 2491 100 million massive binaries for each of 50 metallicities
 2492 equally spaced in log space between $Z \in [0.0001, 0.022]$,
 2493 where Z is the mass fraction of heavy elements. They
 2494 simulate more binaries for higher metallicities so that
 2495 large enough sample of DCOs at each metallicity (since
 2496 DCOs are formed at a lower rate at higher metallicities).
 2497 These metallicities span the allowed metallicity range for
 2498 the original fitting formulae on which COMPAS is based
 2499 (Hurley et al. 2000). This is repeated for 19 physics
 2500 variations (see Section A.3) and so in total over two
 2501 billion binaries were simulated.

2502 Each binary is sampled from initial distributions for
 2503 the primary and secondary masses as well as the separa-
 2504 tion. The primary mass, that is the mass of the initially
 2505 more massive star, is restricted to $m_1 \in [5, 150] M_\odot$,
 2506 which spans the range of interest for NS and BH for-
 2507 mation in binary systems, and drawn from the Kroupa
 2508 (2001) initial mass function (IMF), $p(m_1) \propto m_1^{-2.3}$. The
 2509 secondary mass, m_2 , is drawn using the initial mass
 2510 ratio of the binary, $q \equiv m_2/m_1$, which Broekgaarden
 2511 et al. (2021a,b) assume to be uniform on $[0, 1]$, therefore
 2512 $p(q) = 1$ (e.g. consistent with Sana et al. 2012). They
 2513 additionally restrict the secondary masses $m_2 \geq 0.1 M_\odot$,
 2514 which is approximately the minimum mass for a main
 2515 sequence star. They assume that the initial separation
 2516 follows a flat in the log distribution with $p(a_i) \propto 1/a_i$
 2517 and $a_i \in [0.01, 1000] \text{ AU}$ (Öpik 1924; Abt 1983). They
 2518 assume that all binary orbits are circular at birth to re-
 2519 duce the dimensions of initial parameters. Since they
 2520 focus on post-interaction binaries which will have cir-
 2521 cularised after mass transfer they argue this is a rea-
 2522 sonable assumption (as many studies have in the past)
 2523 and is likely not critical for predicting detection rates
 2524 (Hurley et al. 2002; de Mink & Belczynski 2015).

2525 Broekgaarden et al. (2021a,b) apply the adaptive im-
 2526 portance sampling algorithm STROOPWAFEL (Broek-
 2527 gaarden et al. 2019) to improve the yield of their sample.
 2528 This algorithm increases the prevalence of target DCOs
 2529 (BHBHs, BHNSs and NSNSs in this case) in the sample
 2530 and assigns each a weight, w , which represents the prob-
 2531 ability of drawing the DCO without STROOPWAFEL
 2532 in effect.

2533 A.2. Physical assumptions in the fiducial model

2534 *Stellar Evolution:* To follow the evolution of mas-
 2535 sive stars, COMPAS relies on fitting formulae by Hurley
 2536 et al. (2000) to detailed single star models by Pols et al.
 2537 (1998). COMPAS models the evolution of stars that lose
 2538 or gain mass closely following the algorithms originally
 2539 described in Tout et al. (1996) and Hurley et al. (2002).

2540 *Wind mass loss:* Broekgaarden et al. (2021a,b) fol-
 2541 low the wind prescription from Belczynski et al. (2008),
 2542 which was based on results from Monte Carlo radiative
 2543 transfer simulation of Vink et al. (2000, 2001). They use
 2544 the wind mass loss rates from Vink et al. (2001) for stars
 2545 above 12500 K and the rates from Hurley et al. (2000) for
 2546 cooler stars. Additionally, they use a separate, higher
 2547 wind mass loss rate for luminous blue variable (LBV)
 2548 stars, following Belczynski et al. (2008), to mimic ob-
 2549 served LBV eruptions for stars with luminosities and
 2550 effective temperatures above the Humphreys-Davidson
 2551 limit. They use the Wolf-Rayet-like mass loss rate from
 2552 Hamann & Koesterke (1998) with an additional metal-
 2553 licity scaling from Vink & de Koter (2005) for helium
 2554 stars, and set $f_{\text{WR}} = 1$. See Team COMPAS: J. Riley
 2555 et al. (2021), Section 3 for the explicit equations.

2556 *Mass Transfer:* In determining the stability of mass
 2557 transfer Broekgaarden et al. (2021a,b) use the ζ -
 2558 prescription, which compares the radial response of the
 2559 star with the response of the Roche lobe radius to the
 2560 mass transfer (e.g. Hjellming & Webbink 1987). The
 2561 mass transfer efficiency, $\beta \equiv \Delta M_{\text{acc}}/\Delta M_{\text{don}}$, is the frac-
 2562 tion of the mass transferred by the donor that is actu-
 2563 ally accreted by the accretor. They limit the maximum
 2564 accretion rate for stars to $\Delta M_{\text{acc}}/\Delta t \leq 10M_{\text{acc}}/\tau_{\text{KH}}$,
 2565 where τ_{KH} is the Kelvin-Helmholtz timescale of the star
 2566 (Paczyński & Sienkiewicz 1972; Hurley et al. 2002). The
 2567 maximum accretion rate for compact objects is limited
 2568 to the Eddington accretion rate. If more mass than
 2569 these rates is accreted then they assume that the ex-
 2570 cess is lost through isotropic re-emission in the vicinity
 2571 of the accreting star (e.g. Massevitch & Yungelson 1975;
 2572 Soberman et al. 1997). They assume that all mass trans-
 2573 fer from a stripped post-helium-burning-star (case BB)
 2574 onto a neutron star or black hole is unstable (Tauris
 2575 et al. 2015).

2576 *Common-Envelope:* A common-envelope phase fol-
 2577 lows dynamically unstable mass transfer and Broekgaar-
 2578 den et al. (2021a,b) parameterise this using the α -
 2579 λ prescription from Webbink (1984) and de Kool (1990).
 2580 They assume $\alpha = 1$, such that all of the gravitational

binding energy is available for the ejection of the envelope. For λ they use the fitting formulae from Xu & Li (2010a,b). They assume that any Hertzsprung gap donor stars that initiate a common-envelope phase will not survive this phase due to a lack of a steep density gradient between the core and envelope (Taam & Sandquist 2000; Ivanova & Taam 2004; Klencki et al. 2021). This follows the ‘pessimistic’ common-envelope scenario (c.f. Belczynski et al. 2007). They remove any binaries where the secondary immediately fills its Roche lobe upon the conclusion of the common-envelope phase as they treat these as failed common-envelope ejections, likely leading to a stellar merger.

Supernovae: Broekgaarden et al. (2021a,b) draw the remnant masses and natal kick magnitudes from different distributions depending on the type of supernova that occurs. For stars undergoing a general core-collapse supernova, they use the *delayed* supernova remnant mass prescription from Fryer et al. (2012). The *delayed* prescription does not reproduce a neutron star black hole mass gap and they use this as their default as it has been shown to provide a better fit for observed populations of DCOs (e.g. Vigna-Gómez et al. 2018). They draw the natal kick magnitudes from a Maxwellian velocity distribution with a one-dimensional root-mean-square velocity dispersion of $\sigma_{\text{rms}}^{1D} = 265 \text{ km s}^{-1}$ (Lyne & Lorimer 1994; Hobbs et al. 2005). They assume that stars with helium core masses between $1.6\text{--}2.25 M_\odot$ (Hurley et al. 2002) experience electron-capture supernovae (ECSN) (Nomoto 1984, 1987; Ivanova et al. 2008). They set all remnant masses to $1.26 M_\odot$ in this case as an approximation of the solution to Equation 8 of Timmes et al. (1996). For these supernovae, they set $\sigma_{\text{rms}}^{1D} = 30 \text{ km s}^{-1}$ (e.g. Pfahl et al. 2002; Podsiadlowski et al. 2004). They assume that stars that undergo case BB mass transfer (Dewi et al. 2002) experience extreme stripping which leads to an ultra-stripped supernova (Tauris et al. 2013, 2015). For these supernovae they calculate the remnant mass using the Fryer et al. (2012) prescription and use $\sigma_{\text{rms}}^{1D} = 30 \text{ km s}^{-1}$ (as with ECSN). Stars with final helium core masses between $35\text{--}135 M_\odot$ are presumed to undergo a pair-instability, or pulsational pair-instability supernova (e.g. Woosley et al. 2007; Farmer et al. 2019). They follow the prescription from Marchant et al. (2019) as implemented in (Stevenson et al. 2019) for these supernovae. They assume that kicks are isotropic in the frame of the collapsing star. They adopt a maximum neutron star mass of $2.5 M_\odot$ (e.g. Kalogera & Baym 1996; Fryer et al. 2015; Margalit & Metzger 2017) for the fiducial model and change the Fryer et al. (2012) prescription accordingly.

A.3. Model variations

In addition to their fiducial model for the formation of DCOs, Broekgaarden et al. (2021a,b) explore 19 other models in which they change various aspects of the mass transfer, common-envelope, supernova and wind mass loss physics assumptions in order to assess the effect of their uncertainties on the overall double compact object detection rates and distributions. Each of the models varies a single physics assumption (fiducial assumptions are outlined in Section A.2) and these models are outlined in Table A1.

Their fiducial model is labelled model A. Models B-D focus on changes to the mass transfer physics assumptions. They explore the effect of fixing the mass transfer efficiency β to a constant value, rather than allowing it to vary based on the maximum accretion rate. In models B, C, D, in which they set the value of β to 0.25, 0.5 and 0.75 respectively.

Models E'-K focus on altering the common-envelope physics. In model E' we modify model E from Broekgaarden et al. (2021a,b) to investigate the consequence of assuming that case BB mass transfer is always unstable, whilst allowing Helium HG donors to survive CE events. They change the common-envelope efficiency parameter to $\alpha_{\text{CE}} = 0.1, 0.5, 2.0, 10.0$ in models G, H, I and J respectively. In model K, they relax their restriction that Hertzsprung gap donor stars cannot survive common-envelope events, thereby following the ‘optimistic’ common-envelope scenario. They combine this with model E' in model F.

In models L-R they consider changes related to their assumptions about supernova physics. Model L uses the alternate *rapid* remnant mass prescription from Fryer et al. (2012) instead of the *delayed* prescription. They change the maximum neutron star mass in models M and N to 2 and $3 M_\odot$ respectively to account for the range of predicted maximum neutron star masses. Model O removes the implementation of pair-instability and pulsational pair-instability supernovae. In models P and Q they decrease the root-mean-square velocity dispersion for core-collapse supernovae to explore the effect of lower kicks. Model R removes the natal kick for all black holes.

Finally, in models S-T Broekgaarden et al. (2021a,b) investigate the effect of changing their assumption about wind mass loss rates, specifically for Wolf-Rayet winds. They vary f_{WR} to 0.1 and 5.0 in models S and T respectively. These values approximately span the current range of possible Wolf-Rayet wind efficiencies suggested from observations (e.g. Vink 2017; Hamann et al. 2019; Shenar et al. 2019; Miller-Jones et al. 2021; van Son et al. 2021).

Model	Physics Variation
A	Fiducial (see Section A.2)
B	Fixed mass transfer efficiency of $\beta = 0.25$
C	Fixed mass transfer efficiency of $\beta = 0.5$
D	Fixed mass transfer efficiency of $\beta = 0.75$
E'	Case BB mass transfer always unstable
F	Case BB always unstable + Optimistic CE
G	CE efficiency parameter $\alpha = 0.1$
H	CE efficiency parameter $\alpha = 0.5$
I	CE efficiency parameter $\alpha = 2$
J	CE efficiency parameter $\alpha = 10$
K	HG donor stars initiating a CE survive CE
L	Fryer rapid SN remnant mass prescription
M	Maximum NS mass is fixed to $2 M_{\odot}$
N	Maximum NS mass is fixed to $3 M_{\odot}$
O	PISN and pulsational-PISN not implemented
P	$\sigma_{\text{rms}}^{\text{1D}} = 100 \text{ km s}^{-1}$ for core-collapse supernova
Q	$\sigma_{\text{rms}}^{\text{1D}} = 30 \text{ km s}^{-1}$ for core-collapse supernova
R	Black holes receive no natal kick
S	Wolf-Rayet wind factor $f_{\text{WR}} = 0.1$
T	Wolf-Rayet wind factor $f_{\text{WR}} = 5.0$

Table A1. A description of the 20 binary population synthesis models used in this study. A is the fiducial model, B-D change mass transfer physics, E'-K change common-envelope physics, L-R change supernova physics and S-T change wind mass loss (c.f. Broekgaarden et al. 2021a, Table 2).

2684

B. DETECTION RATE NORMALISATION

In this section we explain the normalisation process that we refer to in Section 2.3. From each simulated instance of the Milky Way we extract the fraction of targets that are detectable, where we define a target as one of BHBH, BHNS or NSNS that merges in a Hubble time. To convert the detectable fraction to a detection rate for the Milky Way, we write that the *number* of detectable targets in the Milky Way is

$$N_{\text{detect}} = f_{\text{detect}} \cdot N_{\text{target,MW}}, \quad (\text{B1})$$

where f_{detect} is the fraction of targets in the instance that were detectable and $N_{\text{target,MW}}$ is the total number of targets that have been formed in the Milky Way's history. We can further break this total down into

$$N_{\text{target,MW}} = \langle \mathcal{R}_{\text{target}} \rangle \cdot M_{\text{SF,MW}}, \quad (\text{B2})$$

2685 where $\langle \mathcal{R}_{\text{target}} \rangle$ is the average number of targets formed
2686 per star forming mass and $M_{\text{SF,MW}}$ is the star forming
2687 mass of the Milky Way, meaning the total mass of every
2688 star ever formed in the Milky Way.

B.1. Average target formation rate

Double compact object formation is metallicity dependent, so we find the average rate as the integral over metallicity, which is given by

$$\langle \mathcal{R}_{\text{target}} \rangle = \int_{Z_{\min}}^{Z_{\max}} p_Z \mathcal{R}_{\text{target,Z}} dZ, \quad (\text{B3})$$

where Z_{\min}, Z_{\max} are the minimum and maximum sampled metallicities, p_Z is the probability of forming a star at the metallicity Z (which can be found using the distribution in Frankel et al. 2018) and $\mathcal{R}_{\text{target,Z}}$ is the number of targets formed per star forming mass,

$$\mathcal{R}_{\text{target,Z}} = \frac{N_{\text{target,Z}}}{M_{\text{SF,Z}}}. \quad (\text{B4})$$

In practice, this integral is instead approximated as a sum over the metallicity bins that we use in our simulation. The number of targets in our sample at a metallicity Z , $N_{\text{target,Z}}$, can be written simply as the sum of the targets' weights:

$$N_{\text{target,Z}} = \sum_{i=1}^{N_{\text{binaries,Z}}} w_i \theta_{\text{target,i}}, \quad (\text{B5})$$

2690 where w_i is the binary's adaptive importance sampling
2691 weight assigned, $N_{\text{binaries,Z}}$ is the number of binaries at
2692 metallicity Z in our sample and $\theta_{\text{target,i}}$ is only 1 when
2693 the binary is a target and otherwise 0.

The total star forming mass at a metallicity Z , $M_{\text{SF,Z}}$, can be written as

$$M_{\text{SF,Z}} = \frac{\langle m \rangle_{\text{COMPAS,Z}}}{f_{\text{trunc}}} N_{\text{binaries,Z}}, \quad (\text{B6})$$

2694 where $\langle m \rangle_{\text{COMPAS}}$ is the average star forming mass of
2695 a binary in a simulation using our cutoffs (discussed
2696 in Section 2.1) and f_{trunc} is the fraction of the total
2697 stellar mass from which our COMPAS simulations sam-
2698 ple, given our truncated mass and separation ranges
2699 (see Section 2.1). These truncations mean that only
2700 $f_{\text{trunc}} \approx 0.17$ of the stellar mass in the galaxy is sam-
2701 pled from.

B.2. Total star forming mass in the Milky Way

2703 It is important to distinguish between the *total* mass
2704 of every star formed over the entire history of the Milky
2705 Way and the *current* stellar mass in the Milky Way.
2706 Many stars born in the Milky Way are no longer living
2707 and have lost much of their mass to stellar winds and
2708 supernovae, thus the current stellar mass in the Milky
2709 Way is an underestimate of the total star forming mass.

Licquia & Newman (2015) find that the total stellar mass today in the Milky Way is $6.08 \pm 1.14 \times 10^{10} M_{\odot}$.

This total includes all stars and stellar remnants (white dwarfs, neutrons stars and black holes) but *excludes* brown dwarfs. We can write that the total mass of every star every formed in the Milky Way is

$$M_{\text{SF,MW}} = (6.08 \pm 1.14) \times 10^{10} M_{\odot} \cdot \frac{\langle m \rangle_{\text{SF,total}}}{\langle m \rangle_{\text{SF,today}}}, \quad (\text{B7})$$

where $\langle m \rangle_{\text{SF,total}}$ is the average mass of a star over the history of the Milky Way and is defined as

$$\langle m \rangle_{\text{SF,total}} = \int_0^{t_{\text{MW}}} p_{\text{birth}}(\tau) \int_{0.01}^{200} \zeta(m) m dm d\tau, \quad (\text{B8})$$

where t_{MW} is the age of the Milky Way, $\zeta(m)$ is the Kroupa (2001) IMF function and $p_{\text{birth}}(\tau)$ is the probability of a star being formed at a lookback time τ (Eq. 2). $\langle m \rangle_{\text{SF,today}}$ is the average mass of all stars and stellar remnants (excluding brown dwarfs) present in the Milky Way today is defined as follows (note that we integrate from 0.08 not 0.01 since observations of today's Milky Way mass exclude brown dwarfs)

$$\langle m \rangle_{\text{SF,today}} = \int_0^{t_{\text{MW}}} p_{\text{birth}}(\tau) \int_{0.08}^{200} \zeta(m) m_{\text{today}} dm d\tau, \quad (\text{B9})$$

where $m_{\text{today}}(m, Z, \tau)$ is the current mass of a star that was formed τ years ago at a metallicity Z . We calculate $m_{\text{today}}(m, Z, \tau)$ by interpolating the final masses given by COMPAS for a grid of single stars over different masses and metallicities using the Fryer et al. (2012) delayed prescription and default wind mass loss settings. For Z , we use the average star forming metallicity in the Milky Way at a lookback time τ using our galaxy model. Evaluating Equation B7, we find that the total mass of every star that has ever formed in the Milky Way is

$$\begin{aligned} M_{\text{SF,MW}} &= (6.1 \pm 1.1) \times 10^{10} M_{\odot} \cdot \frac{0.378 M_{\odot}}{0.221 M_{\odot}}, \\ &= (10.4 \pm 1.1) \times 10^{10} M_{\odot}, \end{aligned} \quad (\text{B10})$$

an increase of approximately 70% from the value still in stars today!

B.3. Normalisation summary

Finally, we can substitute Equations B3 and B7 into B1 and write that the overall normalisation of the detection rate is calculated as

$$\begin{aligned} N_{\text{detect}} &= f_{\text{detect}} \cdot 10.4 \times 10^{10} M_{\odot} \\ &\times \sum_{Z=Z_{\min}}^{Z_{\max}} p_Z \left(\sum_{i=1}^{N_{\text{binaries},Z}} w_i \theta_{\text{target},i} \right) \\ &\times \left(\frac{\langle m \rangle_{\text{COMPAS},Z}}{f_{\text{trunc}}} \sum_{i=1}^{N_{\text{binaries},Z}} w_i \right)^{-1}. \end{aligned} \quad (\text{B11})$$

C. CALCULATION OF THE UNCERTAINTIES IN THE CHIRP MASS FOR DETECTABLE SOURCES

How accurately the chirp mass of a detected binary can be determined depends on the signal to noise ratio, duration of the mission, its orbital frequency and the time derivative of the orbital frequency.

Here we describe how we estimate the uncertainty of the chirp mass. First, consider the chirp mass, which can be expressed as

$$\mathcal{M}_c = \frac{c^3}{G} \left(\frac{5\pi}{48n} \frac{\dot{f}_n}{F(e)} \right)^{3/5} \frac{1}{(2\pi f_{\text{orb}})^{11/5}}, \quad (\text{C1})$$

where f_n is the frequency of the n-th harmonic, f_{orb} is the orbital frequency, \mathcal{M}_c is the chirp mass (defined in Eq. 12), e is the eccentricity and

$$F(e) = \frac{1 + \frac{73}{24}e^2 + \frac{37}{96}e^4}{(1 - e^2)^{7/2}}, \quad (\text{C2})$$

is the enhancement factor of gravitational wave emission for an eccentric binary over an otherwise identical circular binary (Peters & Mathews 1963, Eq. 17). In practice, we will use the dominating harmonic, with $n = n_{\text{dom}}$ and $f_n = n_{\text{dom}} f_{\text{orb}} = f_{\text{dom}}$. The dominating harmonic for circular binaries is $n_{\text{dom}} = 2$ and so the dominating frequency is twice the orbital frequency.

Therefore the chirp mass uncertainty can be estimated as

$$\frac{\Delta \mathcal{M}_c}{\mathcal{M}_c} = \frac{11}{5} \frac{\Delta f_{\text{orb}}}{f_{\text{orb}}} + \frac{3}{5} \frac{\Delta \dot{f}_{\text{dom}}}{\dot{f}_{\text{dom}}} + \frac{3}{5} \frac{\Delta F(e)}{F(e)}, \quad (\text{C3})$$

We estimate the frequency uncertainties using Takahashi & Seto (2002), such that

$$\frac{\Delta f_{\text{orb}}}{f_{\text{orb}}} = 4\sqrt{3} \cdot \frac{1}{\rho} \frac{1}{T_{\text{obs}}} \frac{1}{f_{\text{orb}}}, \quad (\text{C4})$$

$$\frac{\Delta \dot{f}_{\text{dom}}}{\dot{f}_{\text{dom}}} = 6\sqrt{5} \cdot \frac{1}{\rho} \left(\frac{1}{T_{\text{obs}}} \right)^2 \frac{1}{\dot{f}_{\text{dom}}}, \quad (\text{C5})$$

where ρ is the signal-to-noise ratio and T_{obs} is the LISA mission length. We estimate the eccentricity certainty, Δe , following the methods of Lau et al. (2020) and Korol & Safarzadeh (2021), which use the relative SNRs of different harmonics to work out the eccentricity. We propagate this uncertainty such that

$$\frac{\Delta F(e)}{F(e)} = \Delta e \cdot \frac{(1256 + 1608e^2 + 111e^4)e}{96 + 196e^2 - 255e^4 - 37e^6}. \quad (\text{C6})$$

We use Eq. C3 to calculate the chirp mass uncertainty for each DCO type in our sample and plot it in Fig. 6.

2729 D. ASSESSING THE IMPACT OF MILKY WAY
 2730 MODEL CHOICES

2731 The model that we use for the Milky Way adds several layers of complexity, accounting for the inside-out
 2732 growth of the thin disc, using empirically informed star
 2733 formation histories that are a function of time and as-
 2734 signing metallicities based on the position and age of
 2735 binaries. In this section, we repeat our main analysis
 2736 but instead apply a simpler model for the Milky Way in
 2737 order to assess the effect of these added features. For
 2738 this purpose, we use model for the Milky Way used in
 2739 Breivik et al. (2020) as this is representative of the mod-
 2740 els used in most previous works.

2742 Their model can be summarised as follows: the Milky
 2743 Way is assumed to comprise of three components, a thin
 2744 disc, a thick disc and a bulge. The spatial distributions
 2745 and relative masses for these components are given in
 2746 McMillan (2011). Breivik et al. (2020) assume constant
 2747 star formation over 10 Gyr for the thin disc, a 1 Gyr
 2748 burst of star formation 11 Gyr ago for the thick disc
 2749 and a 1 Gyr burst of star formation 10 Gyr ago for the
 2750 bulge. A major difference is that only two metallicities
 2751 are used and they are assigned to binaries independent
 2752 of age or position. Binaries formed in the thin disc and
 2753 bulge are assumed to have a metallicity of $Z = 0.02$
 2754 and those formed in the thick disc are assumed to have
 2755 $Z = 0.003$.

2756 We show the spatial metallicity distribution for this
 2757 model in Fig. D1 in the same form as Fig. 1 for ease
 2758 of comparison between our models. The two main dif-
 2759 ferences we can see between Fig. 1 and D1 are that the
 2760 Breivik et al. (2020) model is more centrally concen-
 2761 trated and only has two fixed metallicity populations.

2762 When applying this simpler Milky Way model in com-
 2763 bination with our fiducial binary physics assumptions
 2764 (model A), we find that the expected number of detec-
 2765 tions for BHBHs, BHNSs and NSNSs for a 4-year LISA
 2766 mission is 52, 25 and 17 respectively. Thus the BHBH
 2767 detection has decreased slightly compared to our main
 2768 findings, whilst for BHNSs and NSNSs the rate has ap-
 2769 proximately halved and doubled respectively.

2770 Moreover, the distribution of parameters within the
 2771 population, particularly the mass distributions, are no-
 2772 tablely disparate. By using only two fixed metallicity pop-
 2773 ulations, unphysical artifacts are introduced into distri-
 2774 bution of DCO masses (e.g. Dominik et al. 2015; Neijssel
 2775 et al. 2019; Kummer 2020). For example, in Fig. D2, we
 2776 show the black hole mass distribution produced by the
 2777 simulation using the simple Milky Way model. Despite
 2778 the fact that these KDEs use the same bandwidth as
 2779 Fig. 3, the distributions show many more sharp transi-
 2780 tions, which is a result of pileups occurring at specific

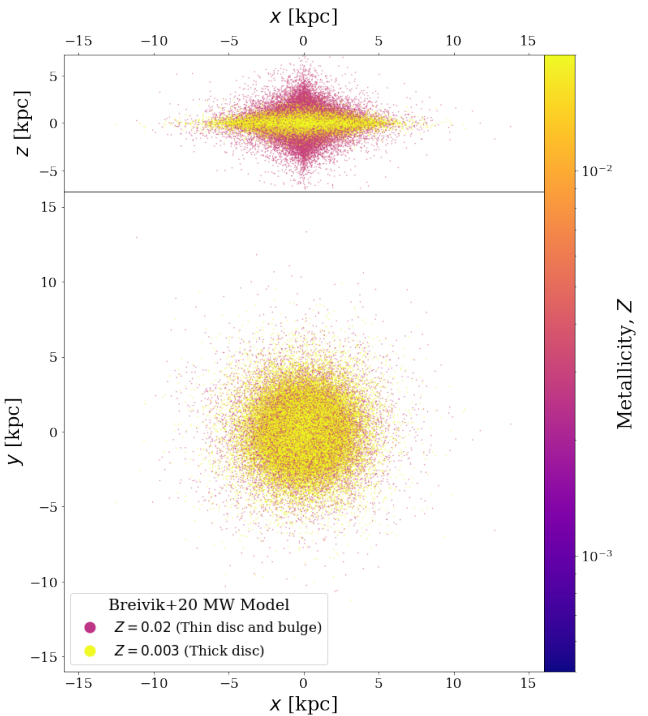


Figure D1. As Fig. 1 (right panel), but for the Milky Way model used in Breivik et al. (2020).

2781 masses for specific metallicities. Moreover, the lack of
 2782 lower metallicity systems means that higher mass sys-
 2783 tems are not formed and so we see the distributions do
 2784 not include a high mass tail such as in our fiducial re-
 2785 sults.

2786 The unphysical artifacts present in the mass distribu-
 2787 tions can have far-reaching effects since the masses of
 2788 DCOs affect most other parameters. The inspiral time
 2789 and SNR are directly dependent on the mass, whilst the
 2790 uncertainty estimates depend on the SNR. This means
 2791 that the artifacts can affect the predictions for most dis-
 2792 tributions of LISA detectable populations.

2793 Overall, we find that previous studies that use Milky
 2794 Way models analogous to this simpler model may signif-
 2795 icantly underestimate the LISA BHNS rate whilst over-
 2796 estimating the NSNS detection rate. They may also miss
 2797 higher mass systems (particular for BHNSs) and contain
 2798 unphysical artifacts in their parameter distributions.

2799 E. ESTIMATING THE NUMBER OF PULSARS
 2800 FOR A GIVEN SKY AREA IN SKA

2801 In this section, we perform some back-of-the-envelope
 2802 calculations in order to estimate the number of pulsars
 2803 that SKA will observe within a given sky area.

2804 First, we consider how many pulsars SKA is likely
 2805 to detect. Keane et al. (2015) uses PSRPOPPy (Bates
 2806 et al. 2014) to simulate the Milky Way pulsar popula-

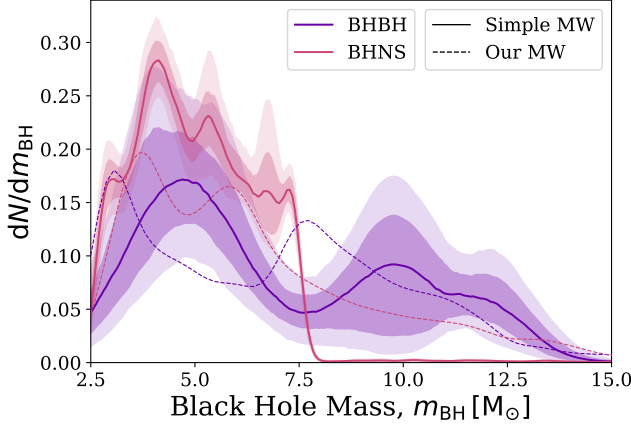


Figure D2. As Fig. 3b, but for the Milky Way model used in Breivik et al. (2020). Dotted lines show the distribution from Fig. 3b for comparison.

tion. They find that for SKA-1, approximately 10000 pulsars will be discovered. The second phase of SKA, which should be in operation by the time of the LISA mission, would yield a total of 35000-41000 pulsars (Keane et al. 2015). We use the average, 38000, in further estimates below. Moreover, we are only interested in pulsars that are part of a binary system. We estimate this pulsar binary fraction as the fraction of known pulsars that are in binaries using the ATNF Pulsar Catalogue⁸ (Manchester et al. 2005). 290 of the 2872 currently known pulsars are in binary systems and thus we estimate the binary fraction of pulsars as 10%. Therefore, we expect that SKA-1 and SKA-2 will detect approximately 1000 and 3800 binary pulsars respectively.

Next, we can find the total number of pulsars SKA will detect in a patch on the sky. The total sky area that the SKA mission covers is approximately 5700 deg^2 , which is calculated by integrating over the sky for all Galactic longitudes and Galactic latitudes limited to $|b| < 10^\circ$ and $\delta < 45^\circ$, which are the limits on SKA-mid (Keane et al. 2015). If we assume that the pulsars are found uniformly across the sky, this means that roughly 0.2 and 0.7 binary pulsars are expected per square degree for SKA-1 and SKA-2 respectively. Note that the assumption of a uniform distribution is not realistic as pulsars will tend to be far more concentrated in the Galactic centre but we use it to provide a slightly optimistic estimate.

Overall, we therefore expect a single pulsar per 5.7 deg^2 and 1.5 deg^2 for SKA-1 and SKA-2 respectively, which correspond to angular resolutions of $\sigma_\theta = 1.3^\circ$ and $\sigma_\theta = 0.7^\circ$.

⁸<https://www.atnf.csiro.au/research/pulsar/psrcat>

F. SUPPLEMENTARY MATERIAL

Table F1. The number of detectable binaries in a 4- and 10-year LISA mission for the 20 different model variations and each DCO type. Each model variation is discussed in App. A.3 and the trends in detection rates are discussed in Sec. 4.1. The ‘All’ column contains the total expected detections when summed over the three types. The final two rows show the minimum and maximum rates across all model variations. We embolden the corresponding rate for convenience of seeing which variation results in the minimum/maximum. Each value shows the mean and the $1-\sigma$ Poisson uncertainty. Ξ .

Model	Description	LISA detections (4 year)				LISA detections (10 year)			
		All	BHBH	BHNS	NSNS	All	BHBH	BHNS	NSNS
A	Fiducial	124^{+11}_{-11}	74^{+8}_{-9}	42^{+7}_{-6}	8^{+3}_{-3}	202^{+14}_{-15}	117^{+11}_{-10}	71^{+8}_{-8}	13^{+4}_{-4}
B	Fixed mass transfer efficiency of $\beta = 0.25$	94^{+10}_{-10}	69^{+8}_{-9}	22^{+5}_{-4}	3^{+2}_{-2}	149^{+12}_{-12}	108^{+10}_{-11}	37^{+6}_{-6}	5^{+2}_{-2}
C	Fixed mass transfer efficiency of $\beta = 0.5$	59^{+8}_{-8}	47^{+7}_{-7}	8^{+3}_{-3}	4^{+2}_{-2}	96^{+9}_{-10}	76^{+8}_{-9}	14^{+3}_{-4}	7^{+2}_{-3}
D	Fixed mass transfer efficiency of $\beta = 0.75$	67^{+8}_{-8}	47^{+7}_{-7}	7^{+3}_{-2}	13^{+3}_{-4}	104^{+11}_{-10}	71^{+8}_{-8}	12^{+4}_{-3}	21^{+5}_{-4}
E'	Case BB mass transfer is always unstable	90^{+9}_{-10}	66^{+8}_{-8}	21^{+5}_{-5}	3^{+2}_{-2}	133^{+12}_{-11}	101^{+10}_{-10}	29^{+5}_{-5}	4^{+2}_{-2}
F	Case BB Unstable + Optimistic CE	368^{+19}_{-19}	154^{+12}_{-13}	198^{+14}_{-14}	17^{+4}_{-4}	553^{+23}_{-24}	238^{+16}_{-15}	289^{+17}_{-17}	25^{+5}_{-5}
G	CE efficiency $\alpha = 0.1$	40^{+6}_{-6}	28^{+5}_{-5}	2^{+2}_{-1}	10^{+3}_{-3}	64^{+8}_{-8}	44^{+6}_{-7}	3^{+2}_{-1}	17^{+4}_{-4}
H	CE efficiency $\alpha = 0.5$	86^{+9}_{-10}	58^{+8}_{-7}	22^{+4}_{-5}	6^{+2}_{-3}	136^{+11}_{-12}	91^{+10}_{-9}	35^{+6}_{-6}	10^{+3}_{-3}
I	CE efficiency $\alpha = 2.0$	133^{+11}_{-12}	67^{+9}_{-8}	38^{+6}_{-6}	28^{+5}_{-6}	218^{+14}_{-15}	109^{+11}_{-10}	62^{+8}_{-7}	46^{+7}_{-7}
J	CE efficiency $\alpha = 10.0$	78^{+9}_{-9}	27^{+5}_{-6}	16^{+4}_{-4}	35^{+6}_{-6}	126^{+11}_{-11}	42^{+7}_{-6}	27^{+5}_{-6}	57^{+8}_{-7}
K	HG donor stars initiating a CE survive CE	218^{+14}_{-15}	151^{+12}_{-12}	57^{+7}_{-8}	10^{+3}_{-3}	340^{+19}_{-18}	229^{+15}_{-15}	96^{+10}_{-10}	16^{+4}_{-4}
L	Fryer rapid SN remnant mass prescription	127^{+11}_{-11}	50^{+7}_{-7}	70^{+8}_{-8}	7^{+2}_{-3}	204^{+15}_{-14}	76^{+9}_{-8}	117^{+11}_{-11}	11^{+3}_{-3}
M	Maximum NS mass = $2.0 M_{\odot}$	133^{+12}_{-11}	96^{+10}_{-10}	30^{+5}_{-5}	7^{+3}_{-2}	214^{+15}_{-14}	153^{+13}_{-12}	50^{+7}_{-7}	12^{+3}_{-4}
N	Maximum NS mass = $3.0 M_{\odot}$	118^{+11}_{-11}	58^{+8}_{-8}	52^{+7}_{-7}	8^{+3}_{-3}	189^{+14}_{-13}	91^{+10}_{-9}	85^{+9}_{-10}	14^{+3}_{-4}
O	No PISN and pulsational-PISN	126^{+12}_{-11}	75^{+9}_{-9}	43^{+7}_{-6}	8^{+3}_{-3}	205^{+14}_{-14}	120^{+11}_{-11}	72^{+9}_{-8}	13^{+3}_{-4}
P	$\sigma_{\text{RMS}}^{1D} = 100 \text{ km s}^{-1}$ for CCSN	184^{+14}_{-14}	82^{+9}_{-9}	86^{+10}_{-9}	15^{+4}_{-4}	300^{+17}_{-17}	130^{+11}_{-12}	145^{+12}_{-12}	26^{+5}_{-6}
Q	$\sigma_{\text{RMS}}^{1D} = 30 \text{ km s}^{-1}$ for CCSN	268^{+16}_{-16}	92^{+9}_{-10}	143^{+12}_{-12}	34^{+6}_{-6}	426^{+21}_{-20}	142^{+12}_{-11}	229^{+15}_{-16}	55^{+8}_{-7}
R	Black holes receive not natal kick	205^{+15}_{-14}	89^{+10}_{-9}	109^{+10}_{-11}	7^{+3}_{-2}	332^{+18}_{-18}	140^{+12}_{-12}	180^{+13}_{-13}	12^{+3}_{-4}
S	Wolf-Rayet wind factor $f_{\text{WR}} = 0.1$	118^{+11}_{-11}	75^{+9}_{-8}	34^{+6}_{-6}	9^{+3}_{-3}	182^{+13}_{-14}	112^{+11}_{-11}	56^{+7}_{-8}	14^{+4}_{-4}
T	Wolf-Rayet wind factor $f_{\text{WR}} = 5.0$	30^{+5}_{-6}	6^{+2}_{-3}	15^{+4}_{-3}	8^{+3}_{-2}	49^{+7}_{-7}	9^{+3}_{-3}	26^{+5}_{-5}	13^{+4}_{-3}
-	Minimum rate	30^{+5}_{-6}	6^{+2}_{-3}	2^{+2}_{-1}	3^{+1}_{-2}	49^{+7}_{-7}	9^{+3}_{-3}	3^{+2}_{-1}	4^{+2}_{-2}
-	Maximum rate	368^{+19}_{-19}	154^{+12}_{-13}	198^{+14}_{-14}	35^{+6}_{-6}	553^{+23}_{-24}	238^{+16}_{-15}	289^{+17}_{-17}	57^{+8}_{-7}



Figure F1. Fraction of each DCO type that is formed through different formation channels for all physics variations. Channels are described in detail in Broekgaarden et al. (2021a). The classic, single core CEE and double core CEE channels all require at least one common-envelope event whilst only “only stable” consists of only stable mass transfer and “other” contains the remaining binaries which are mainly formed from case A “classic” binaries as well as “lucky” supernova kicks that shrink the binary.  .



Figure F2. As the bottom panels of Fig. 2, but without the density distributions and scatter points are coloured by their eccentricity. We show eccentric sources are located in an offshoot below the 30 kpc around 2 mHz. .



Figure F3. As Fig. 3, but for the properties of the detectable systems at DCO formation. .